Neutrino-Nucleus Scattering from First Principles

Dissertation zur Erlangung des Doktorgrades der Naturwissenschaften (Dr. rer. nat.) der Fakultät für Physik der Universität Regensburg

vorgelegt von

Andreas Hackl

aus

Freyung

im Jahr 2025

Promotionsgesuch eingereicht am: 27.05.2025
Die Arbeit wurde angeleitet von: Prof. Dr. Christoph Lehner

Prüfungsausschuss:

Vorsitzender:	Prof. Dr. Franz J. Gießibl
1. Gutachter:	Prof. Dr. Christoph Lehner
2. Gutachter:	Prof. Dr. Gunnar S. Bali
weiterer Prüfer:	Prof. Dr. Ferdinand Evers

Datum Promotionskolloquium: 22.10.2025

Abstract

Upcoming neutrino experiments, such as LBNF/DUNE and HyperK, demand accurate theoretical models of the nucleus-neutrino cross section, particularly in the energy range from a few MeV to GeV where the interaction is described by quasi-elastic and resonant regions. These regions are described by the effective interaction of the entering neutrino with a single nucleon within the nucleus. Effective field theories provide a framework to model this interaction, which necessitates a non-perturbative input of fundamental neutrino-nucleon interactions. Lattice QCD facilitates the determination of these interactions from first principles. This thesis explores a crucial step in the ongoing effort to identify the necessary input parameters for effective field theories by conducting a spectral analysis of the nucleon spectrum in the positive and negative parity sectors. This study presents the first explicit computation of the nucleon-pion-pion state and the first calculation of the nucleon-pion state at the physical pion mass using a fermion discretization with good chiral properties.

The spectral analysis is conducted utilizing the exact distillation method, emphasizing its effectiveness for baryonic quantities, especially concerning multi-hadronic states. This sets the stage for future investigations, for example, for the calculation of form factors. The research employs seven $2+1$ domain-wall fermion ensembles, defined by pion masses ranging from $m_\pi = 139$ MeV to $m_\pi = 279$ MeV, along with two distinct lattice spacings ($a^{-1} = 1.730$ GeV and $a^{-1} = 2.359$ GeV) and multiple volumes ($m_\pi L = 3.8 - 7.5$). In the positive parity sector, this thesis additionally offers a complete physical point extrapolation of the nucleon mass to evaluate the robustness of the approach. To address the extensive number of contractions from the correlator calculations, this thesis introduces an algorithm to automate the contraction of correlation functions with a single nucleon at the source and sink and any number of pions. The automated contractor is designed in such a manner that it enables a smooth transition to the distillation method.

Contents

1. Introduction

Neutrinos occupy a distinctive role in the standard model of particle physics. These neutral particles with spin 1/2 interact within the standard model exclusively through the weak nuclear force (see Fig. 1.1). Due to this limited interaction potential, neutrinos rarely interact with other particles. For a quantitative example, approximately one light year ($\sim 9.46 \times 10^{12}$ km) of lead is required for half of the neutrinos to interact with the medium as they traverse through it[1]. Additionally, neutrinos are considered to be some of the most abundant particles in the universe. On average, approximately a trillion neutrinos traverse our bodies each second[2].

This weak interaction potential of neutrinos has both advantages and disadvantages. An advantage is that neutrinos allow us to observe parts of the universe typically difficult to study with photons, such as the Sun's core. In the core, photons, which have an average free path roughly on the order of centimeters [1], undergo frequent scattering. As a result, by the time they reach the surface, the electromagnetic radiation appears as black-body radiation, providing no insights into the nuclear fusion processes within the Sun. In contrast, neutrinos generated by fusion processes can traverse the Sun's core with minimal interference, thereby granting us insight into the fusion reactions occurring in the Sun. The disadvantage is that this behavior significantly complicates their detection.

Beyond their role as unique messengers from otherwise inaccessible regions like the Sun's core, neutrinos also offer a promising avenue for probing some of the most fundamental questions in cosmology and particle physics. The early universe created almost equal amounts of matter and antimatter. Nevertheless, a minor disparity existed, with slightly more matter present than antimatter [2, 3]. This disparity, referred to as matter-antimatter asymmetry, is crucial because without it the universe would lack complex structures such as stars and consequently life would not exist. This imbalance suggests that the CP (charge conjugation and parity) symmetry must be violated. Precise measurement of neutrino oscillation might allow us to measure this CP violation in the leptonic sector (see Sec. 4.1). A potential finding of future neutrino experiments could be the detection of indications of proton decay, a theorized process that is postulated by numerous beyond the standard model (BSM) theories, thereby allowing for these theories to be evaluated. Moreover, similar to the previously mentioned example of the Sun, neutrino detectors are capable of detecting neutrinos produced during core-collapse supernovae. This capability could improve our understanding of these phenomena, which play a crucial role in the formation of neutron stars and black holes.

Neutrino detection is generally achieved with large-scale and highly sensitive detectors. Detection occurs indirectly via secondary particles generated when a neutrino interacts with a nucleus within the detector. Ch. 4 provides a detailed introduction to neutrino detection. However, the key point here is that these detectors depend on the theoretical

[1] This numbers are provided in https://snews.bnl.gov/popsci/neutrino.html

[2] Source: https://novaexperiment.fnal.gov/what-is-a-neutrino/

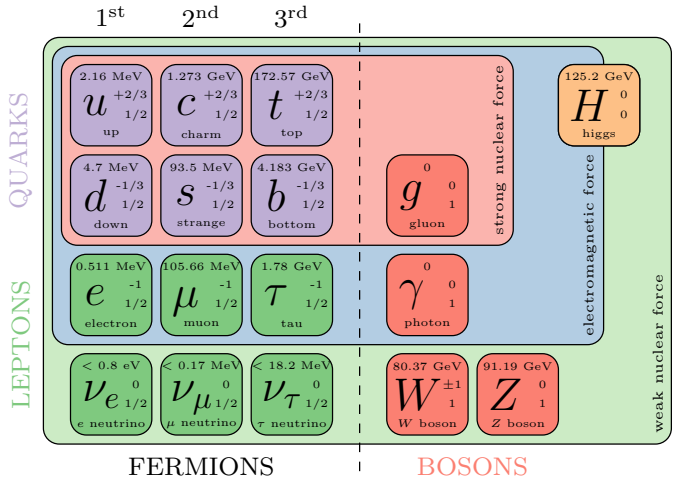

Figure 1.1.: Overview of the elementary particles in the standard model of particle physics. Modified version of https://github.com/mlubej/standard-model

input. Providing a portion of this theoretical input serves as the primary motivation for this thesis. The primary emphasis is on low-energy scattering events where neutrino energies are less than 10 GeV. At the tree level, these interactions are governed entirely by weak force through the exchange of Z or $W^{\pm}$ bosons. Nevertheless, when quantum corrections are accounted for, contributions from other standard-model forces also arise: the strong force, as described by quantum chromodynamics (QCD), and the electromagnetic force, as explained by quantum electrodynamics (QED). In the case of neutrino-nucleus interactions, the predominant contribution arises from QCD corrections. At low-energy scales that are relevant to such interactions, the strong coupling of QCD prohibits a perturbative description as used with other forces. Consequently, to address the QCD component, we employ lattice QCD, which is a non-perturbative first-principles method for calculating QCD observables.
The key measurable quantity for neutrino-nucleus scattering is the axial-vector current with given initial and final states, more closely discussed in Ch. 4, particularly with respect to the nucleon and its excited states. Calculating the axial vector current requires an accurate understanding of the nucleon state spectrum. This thesis offers such a spectral analysis using the exact distillation method, concentrating on nucleon, nucleon-pion, and, for the first time, nucleon-pion-pion states. Additionally, it presents a spectral analysis within the negative parity sector.

The chapters of this thesis are organized as follows: Ch. 2 presents a brief overview of lattice QCD, emphasizing topics relevant to this thesis, such as hadron spectroscopy and the study of nucleons on the lattice. Ch. 3 offers an introduction to group theory and its application in constructing operators relevant for multi-hadronic states, including nucleon-pion and nucleon-pion-pion states. Subsequently, Ch. 4 delves into neutrino physics with an emphasis on the DUNE/LNBF experiments as a case study. The chapter concludes by discussing the role that lattice QCD can play in providing theoretical support for neutrino experiments. Ch. 5 provides a comprehensive overview of the technical aspects concerning

the lattice computations and statistical analyses utilized throughout this thesis. Ch. 6 presents the findings of the thesis' first project, focusing on a spectral analysis of the omega baryon. The omega serves as an effective testing ground for various concepts due to its relatively low computational demands. In Ch. 7, the second project is detailed, which involves a spectral analysis of the rho mesons and two-pion states using the distillation method. This work is related to determining the long-distance window contribution of hadronic vacuum polarization to the anomalous magnetic moment of the muon, as reported in [4]. The subsequent chapter, Ch. 8, details the results of the aforementioned spectral analysis of nucleon, nucleon-pion, and nucleon-pion-pion states in the positive parity sector, along with an analysis of the negative parity sector. These analyses represent the main results of this thesis and are documented in [5]. The thesis concludes with a concise summary and outlook in Ch. 9.

2. Lattice QCD

Quantum Chromodynamics (QCD) is the fundamental theory describing the strong force, dictating the interaction between quarks and gluons (see Fig. 1.1). Lattice QCD is a non-perturbative approach that discretizes space-time on a lattice, allowing for first principles calculations of hadronic properties and interactions. The forthcoming chapter offers a brief overview of lattice QCD, specifically focusing on topics relevant to this thesis. It is not intended as a comprehensive introduction. For a broader introduction to Lattice QCD, the reader is referred to standard textbooks [6, 7].

2.1. QCD in the Continuum

We start with the definition of the QCD action for a 3+1-dimensional continuum Minkowski space-time

$$S_{\mathrm{QCD}}[\bar{\psi},\psi,A] = \int \mathrm{d}^4x \left(\sum_f \bar{\psi}^{(f)}(x) \left(i\gamma^\mu D_\mu - m^{(f)} \right) \psi^{(f)}(x) + \frac{1}{2}\mathrm{tr}\left[F_{\mu\nu}(x) F^{\mu\nu}(x) \right] \right). \tag{2.1}$$

The action involves n_f quark fields $\psi^{(f)}(x)$ representing various flavors (f): up, down, strange, charm, bottom, and top. The quark field $\psi^{(f)}_{\mu,c}(x)$ for a specific flavor itself has two independent indices, the spin index $\mu = 0,1,2,3$ and the color index $c = 0,1,2$. The spin index is a consequence of the quarks transforming in the irreducible representation $(\frac{1}{2},0)\oplus(0,\frac{1}{2})$ of the Lorentz group [8]. The local $SU(3)$ gauge symmetry of QCD introduces the so-called color charges, giving rise to the color index of the quark field. The adjoint quark field $\bar{\psi}^{(f)}(x)$ is defined by $\bar{\psi}^{(f)}(x) = \psi^\dagger(x)\gamma^0$, where γ^0 denotes the Minkowski γ-matrix in the time direction defined in Sec. A.2. In the following, we will reconstruct the QCD action in Eq. 2.1 with the help of symmetry considerations. Quarks are fermions, and hence, in the free theory, they have to obey the Dirac equation, which is the Euler-Lagrange equation of the action

$$S_D[\bar{\psi},\psi] = \int \mathrm{d}^4x \sum_f \bar{\psi}^{(f)}(x)(i\gamma^\mu\partial_\mu - m^{(f)})\psi^{(f)}(x). \tag{2.2}$$

However, this action is not invariant under local $SU(3)$ gauge transformations

$$\psi(x) \to \psi'(x) = \Omega(x)\psi(x), \tag{2.3a}$$
$$\bar{\psi}(x) \to \bar{\psi}'(x) = \bar{\psi}(x)\Omega^\dagger(x), \tag{2.3b}$$

where $\Omega(x)$ denotes a general $SU(3)$ matrix. The action in Eq. 2.2 becomes invariant if we replace the partial derivative with the covariant derivative, defined as

$$D_\mu(x) = \partial_\mu + igA_\mu(x), \tag{2.4}$$

where we introduce the gluon fields $A_\mu(x)$ and the strong coupling constant g. The gluon field consists of four components $\mu = 0, 1, 2, 3$, similar to the four-vector potential in quantum electrodynamics (QED). One main difference from QED, with the symmetry group $U(1)$, is that gluons have eight color charges, in contrast to the neutral photon of QED. Therefore, the gluon field is a combination of eight gluon fields carrying color charge a, represented by $A_\mu(x) = \sum_{a=1}^{8} \frac{\lambda_a}{2} A_\mu^a(x)$, where λ_a are the generators of $SU(3)$, also known as the Gell-Mann matrices. To ensure a gauge-invariant fermion action

$$S_F[\bar{\psi}, \psi, A] = \int \mathrm{d}^4x \sum_f \bar{\psi}^{(f)}(x)(i\gamma^\mu D_\mu - m^{(f)})\psi^{(f)}(x), \tag{2.5}$$

it is necessary for the gluon field to transform as

$$A_\mu(x) \to A'_\mu(x) = \Omega(x)A_\mu(x)\Omega^\dagger(x) + \frac{i}{g}(\partial_\mu\Omega(x))\Omega^\dagger(x). \tag{2.6}$$

Given the transformation properties of the gluon field, we find that the covariant derivative undergoes the following transformation:

$$D_\mu(x) \to D'_\mu(x) = \partial_\mu + igA'_\mu(x) = \Omega(x)D_\mu(x)\Omega^\dagger(x). \tag{2.7}$$

Using this transformation behavior, we can then construct the pure gluonic part of the action in Eq. 2.1 by first defining the field strength tensor

$$F_{\mu\nu}(x) = -\frac{i}{g}\left[D_\mu(x), D_\nu(x)\right] = \partial_\mu A_\nu(x) - \partial_\nu A_\mu(x) + ig\left[A_\mu(x), A_\nu(x)\right], \tag{2.8}$$

where the commutator $[A_\mu(x), A_\nu(x)]$ causes the self-interaction of the gluons and, as a consequence, leads to the confinement of QCD [6]. The field strength tensor inherits the transformational behavior of the gauge from the covariant derivative, i.e., $F_{\mu\nu}(x) \to F'_{\mu\nu}(x) = \Omega(x)F_{\mu\nu}(x)\Omega^\dagger(x)$. Hence, it is easy to see that the gluonic part of the action in Eq. 2.1, i.e.,

$$S_G[A] = \frac{1}{2}\int \mathrm{d}^4x \ \mathrm{tr}\left[F_{\mu\nu}(x)F^{\mu\nu}(x)\right], \tag{2.9}$$

is invariant under gauge transformations. With that, we have defined the QCD action in the continuum for a Minkowski space-time.
We can use the QCD action for the calculation of expectation values of the operator $\mathcal{O}$ using the so-called path integral

$$\langle\mathcal{O}\rangle = \frac{1}{Z_{\mathrm{QCD}}}\int \mathcal{D}[\bar{\psi}, \psi]\mathcal{D}[A]e^{iS_{\mathrm{QCD}}[\bar{\psi},\psi,A]}\mathcal{O}[\bar{\psi}, \psi, A], \tag{2.10}$$

with the gluonic measure

$$\mathcal{D}[A] \equiv \prod_x \prod_{\mu=1}^{4} \prod_{a=1}^{8} \mathrm{d}A_\mu^a(x), \tag{2.11}$$

the fermionic measure

$$\mathcal{D}[\bar{\psi}, \psi] = \prod_f \prod_x \prod_{\alpha=1}^{4} \prod_{c=1}^{3} \mathrm{d}\bar{\psi}_{\alpha,c}^{(f)}(x)\mathrm{d}\psi_{\alpha,c}^{(f)}(x) \tag{2.12}$$

and QCD partition function

$$Z_{\mathrm{QCD}} = \int \mathcal{D}[\bar{\psi}, \psi]\mathcal{D}[A] e^{iS_{\mathrm{QCD}}[\bar{\psi},\psi,A]}. \tag{2.13}$$

A widely used technique for evaluating this integral is perturbation theory. This method implies the expression of the QCD action as the sum of two components: the analytically solvable free action, S_0, and the interaction action, S_{int}, such that $S_{\mathrm{QCD}} = S_0 + gS_{\mathrm{int}}$. The path integral is then expanded as a power series in g. This expansion in powers of g is often associated with Feynman diagrams.

A fundamental characteristic of QCD, as well as other quantum field theories, is the running of the coupling constant. In QCD, this behavior signifies that the strength of the strong interaction depends on the energy scale, diminishing at high energies and increasing at low energies, as dictated by the renormalization group equations. At high energies, the weak coupling results in asymptotic freedom, allowing quarks to interact as nearly-free particles. In contrast, at low energies, the strong coupling leads to confinement, ensuring that quarks and gluons remain permanently bound within hadrons. A more detailed introduction to QCD from a perturbative perspective lies beyond the scope of this thesis, and I refer the interested reader to standard references [9, 10].

In the low-energy regime, the relevant regime of this thesis, the perturbative expansion fails to converge, necessitating the use of a non-perturbative approach. A well-established first principles non-perturbative method is lattice QCD, which forms the foundation of this work.

2.2. QCD on the Lattice

In lattice QCD, we want to numerically estimate the integral in Eq. 2.10. However, because the factor $e^{iS_{\mathrm{QCD}}}$ oscillates, it creates a severe numerical sign problem. To resolve this, we perform the calculations in Euclidean space-time by substituting real time t with imaginary time $\tau = it$ (a procedure known as Wick rotation). This change in metric also modifies the definition of the γ matrices (see Sec. A.2). The Wick rotation transforms the operator expectation value from Eq. 2.10 into the Euclidean form

$$\langle \mathcal{O} \rangle_E = \frac{1}{Z^E_{\mathrm{QCD}}} \int \mathcal{D}[\bar{\psi}, \psi]\mathcal{D}[A]\, e^{-S^E_{\mathrm{QCD}}[\bar{\psi},\psi,A]}\, \mathcal{O}[\bar{\psi}, \psi, A], \tag{2.14}$$

with the Euclidean action S^E_{QCD} and partition function

$$Z^E_{\mathrm{QCD}} = \int \mathcal{D}[\bar{\psi}, \psi]\mathcal{D}[A]\, e^{-S^E_{\mathrm{QCD}}[\bar{\psi},\psi,A]}. \tag{2.15}$$

Since S^E_{QCD} is real, the oscillatory term $e^{iS_{\mathrm{QCD}}}/Z_{\mathrm{QCD}}$ is replaced by $e^{-S^E_{\mathrm{QCD}}}/Z^E_{\mathrm{QCD}}$, which is bounded between 0 and 1 and can be interpreted as a probability distribution. This allows the Euclidean path integral in Eq. 2.14 to be computed via Monte Carlo integration. One can also relate the Euclidean path integral formulation to the Hamiltonian operator formalism. Assuming a finite Euclidean time extent T, the expectation value of an operator $\mathcal{O}$ is given by

$$\langle \mathcal{O} \rangle_{E,T} = \frac{\mathrm{Tr}\left(e^{-\hat{H}T}\hat{\mathcal{O}}\right)}{\mathrm{Tr}\left(e^{-\hat{H}T}\right)}, \tag{2.16}$$

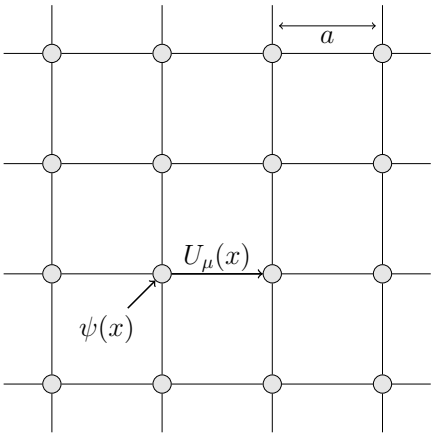

Figure 2.1.: Sketch of a 2-dimensional lattice illustrating that the fermionic fields $\psi(x)$ are defined on the lattice points and the gauge links $U_\mu(x)$ connecting x and $x+\hat{\mu}$.

where $\hat{H}$ is the QCD Hamiltonian. In Minkowski space-time, the corresponding expression is

$$\langle \mathcal{O} \rangle_{M,T} = \frac{\mathrm{Tr}\left(e^{i\hat{H}T}\hat{\mathcal{O}}\right)}{\mathrm{Tr}\left(e^{i\hat{H}T}\right)}. \tag{2.17}$$

In this context, it is convenient to define the transfer matrices:

- In Minkowski space-time: $T_M = e^{i\hat{H}t}$,
- In Euclidean space-time: $T_E = e^{-\hat{H}t}$.

Both transfer matrices are used to compute the expectation values $\langle \mathcal{O} \rangle_T$. In particular, the eigenstates of the Hamiltonian are also eigenstates of both T_M and T_E, which means that they span the same Fock space. Consequently, one can extract spectral information and matrix elements in Minkowski space-time by performing calculations in Euclidean space-time.
To make the computation of Eq. 2.14 feasible, we need to make another restriction: We have to discretize the space-time into $N_s^3 \times N_t$ points forming the set of lattice points

$$\Lambda = \{(a_s n_x, a_s n_y, a_s n_z, a_t n_t) \mid 0 \leq n_x, n_y, n_z < N_s \text{ and } 0 \leq n_t < N_t\}, \tag{2.18}$$

where a_s and a_t denote the lattice spacing in spatial and temporal directions, respectively. Throughout this thesis, we use isotropic lattices, which have the same lattice spacing in temporal and spatial directions, i.e., $a = a_t = a_s$.
The discretized versions of the fermionic field ψ and $\bar{\psi}$ are simply the field at the lattice points $\psi(x)$ for $x \in \Lambda$ (see Fig. 2.1). However, for the gauge fields A_μ, more attention is required. From the gauge invariance of the discretized version of $\bar{\psi} D_\mu \psi$, one can deduce that we need to define $SU(3)$ link variables $U_\mu(x)$. These link variables can be connected to the gauge fields A_μ via the gauge transporter along a curve $\mathcal{C}_{x,x+a\hat{\mu}}$ connecting the points x and $x + a\hat{\mu}$:

$$\tilde{U}_\mu(x) = \mathcal{P} \exp\left(i \int_{\mathcal{C}_{x,x+a\hat{\mu}}} A_\mu \cdot \mathrm{d}s \right), \tag{2.19}$$

where $\mathcal{P}$ denotes the path ordering operator [9]. A more convenient way to define the gauge link is to approximate the integral by $\int_{\mathcal{C}_{x,x+a\hat{\mu}}} A_\mu \cdot \mathrm{d}s = aA_\mu(x) + \mathcal{O}(a^2)$, which leads to

$$U_\mu(x) = \exp\Big(iagA_\mu(x) + \mathcal{O}(a^2)\Big). \tag{2.20}$$

Fig. 2.1 summarizes the role of the fermionic and gluonic fields in the discretized theory. All fermionic fields ψ with flavor, spin, and color indices are defined at the lattice points $x \in \Lambda$. The gluonic fields are defined as part of the links U_μ between neighboring lattice sites. In the path integral of Eq. 2.14, it is equivalent to integrating over the gluonic fields and the link variables. The only subtlety is that one has to be careful since A_μ are elements of the Lie algebra, whereas the link variables are elements of the Lie group. In the following, we will always use the integration over the link variables that leads to the Euclidean expectation value of $\mathcal{O}$ on the lattice described by

$$\langle \mathcal{O} \rangle_E = \frac{1}{Z^E_{\mathrm{QCD}}} \int \mathcal{D}[\bar{\psi}, \psi] \mathcal{D}[U]\, e^{-S^E_{\mathrm{QCD}}[\bar{\psi},\psi,U]}\, \mathcal{O}[\bar{\psi}, \psi, U], \tag{2.21}$$

which is then solved using Monte Carlo techniques, which is elaborated more at the end of Sec. 2.7.
The remaining part to discretize is the action, which is part of the following two sections.

2.3. Iwasaki Gauge Action

Generally, there are multiple ways to formulate a gauge action on the lattice. The simplest version is the Wilson gauge actions defined as

$$S_W[U] = \frac{\beta}{3} \sum_{x \in \Lambda} \sum_{\mu < \nu} \mathrm{Re}\,\mathrm{tr}\Big\{ \mathbb{1} - R^{(1\times1)}_{\mu\nu}(x) \Big\}, \tag{2.22}$$

with $\beta = \frac{6}{g^2}$ and the plaquette

$$R^{(1\times1)}_{\mu\nu}(x) = U_\mu(x) U_\nu(x + \hat{\mu}) U^\dagger_\mu(x + \hat{\nu}) U^\dagger_\nu(x), \tag{2.23}$$

representing the shortest loop of link variables possible (cf. Fig. 2.2). In the construction of the plaquette, we use the relation that

$$U_{-\mu}(x) = U^\dagger_\mu(x - a\hat{\mu}), \tag{2.24}$$

and $\hat{\mu}$ denotes an unit vector in the μ direction. Using the gauge transformation of the link $U_\mu(x)$ given by

$$U_\mu(x) \to U'_\mu(x) = \Omega(x) U_\mu(x) \Omega^\dagger(x + \hat{\mu}), \tag{2.25}$$

yields the result that the plaquette transforms under gauge transformations like

$$R^{(1\times1)}_{\mu\nu}(x) \to \tilde{R}^{(1\times1)}_{\mu\nu}(x) = \Omega(x) R^{(1\times1)}_{\mu\nu}(x) \Omega^\dagger(x). \tag{2.26}$$

Calculating the trace of the plaquette results in a gauge-invariant expression, leading to the action as shown in Eq. 2.22. Using Eq. 2.20 and repeating the Baker-Campell-Hausdorff formula

$$\exp(A)\exp(B) = \exp\left(A + B + \frac{1}{2}[A, B] + \dots\right) \tag{2.27}$$

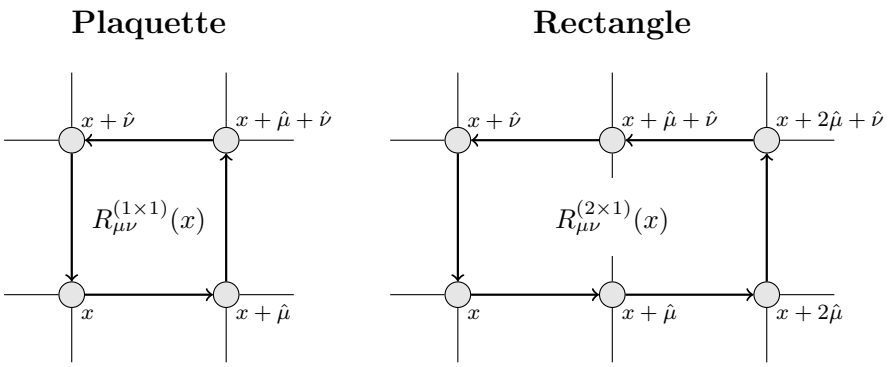

Figure 2.2.: Depiction of the plaquette and rectangle used to construct gauge actions.

yields for the plaquette that

$$R_{\mu\nu}^{(1\times1)}(x) = \exp\Big(ia^2 g F_{\mu\nu}(x) + \mathcal{O}(a^3)\Big). \tag{2.28}$$

The expanded version of this expression for $R^{(1\times1)}$ inserted into the definition of Wilson gauge action (cf. Eq. 2.22) yields

$$S_W[U] = \frac{a^4}{2} \sum_{x\in\Lambda} \sum_{\mu,\nu} \mathrm{tr}[F_{\mu\nu}(x)^2] + \mathcal{O}(a^2), \tag{2.29}$$

where $a^4 \sum_{x\in\Lambda}$ converges for $a \to 0$ and $N \to \infty$ to the space-time integral of Eq. 2.1 and hence we have recovered the QCD action in the continuum limit.
As mentioned above, there are multiple ways to define a gauge action on the lattice. One natural expansion of the Wilson gauge action of Eq. 2.22 is to include 2×1 rectangle terms, which are constructed by

$$R_{\mu\nu}^{(2\times1)}(x) = U_\mu(x) U_\mu(x+\hat{\mu}) U_\nu(x+2\hat{\mu}) U_\mu^\dagger(x+\hat{\nu}+\hat{\mu}) U_\mu^\dagger(x+\hat{\nu}) U_\nu^\dagger(x). \tag{2.30}$$

The graphic on the right of Fig. 2.2 symbolizes the 2×1 rectangle. The extended gauge action is then

$$S_{\text{Iwasaki}}[U] = \frac{\beta}{3} \sum_{x\in\Lambda} \left(c_0 \sum_{\mu<\nu} \mathrm{Re\,tr}\Big\{ R_{\mu\nu}^{(1\times1)}(x) \Big\} + c_1 \sum_{\mu\neq\nu} \mathrm{Re\,tr}\Big\{ R_{\mu\nu}^{(2\times1)}(x) \Big\} \right), \tag{2.31}$$

where we drop the constant part because of physical irrelevance. The prefactors c_0 and c_1 are determined using renormalization group arguments to be close to the renormalization group trajectory. Following [11], we obtain $c_1 = -0.331$ and $c_0 = 1 - 8c_1$ as optimized parameters yielding the **Iwasaki gauge action**, which is used for all the ensembles used throughout this thesis.

2.4. Wilson Fermions

A naive gauge-invariant way to discretize the fermionic action is

$$S_F^n[\bar{\psi}, \psi, U] = a^4 \sum_{x,y\in\Lambda} \underset{a}{\bar{\psi}_\alpha}(x) \underset{ab}{D^n_{\alpha\beta}}(x|y) \underset{b}{\psi_\beta}(x) \tag{2.32}$$

where we impose Einstein sum convention for a, b, α, β and the naive discretized Dirac operator D^n reads

$$D^n_{\substack{\alpha\beta \\ ab}}(x|y) = \sum_\mu (\gamma_\mu)_{\alpha\beta} \frac{U_\mu(x)_{ab}\delta_{x+a\hat{\mu},y} - U^\dagger_\mu(x-a\hat{\mu})\delta_{x-a\hat{\mu},y}}{2a} + m\delta_{ab}\delta_{\alpha\beta}\delta_{x,y}. \tag{2.33}$$

The main problem with this naive approach can be seen by considering the propagator of the free fermions in momentum space. For free fermions, the gluon fields vanish and we find that $U_\mu(x) = \mathbb{1}$. The Fourier transformation of Eq. 2.33 is given by

$$\tilde{D}^n(p|q) = \frac{1}{|\Lambda|} \sum_{x,y\in\Lambda} e^{-ip\cdot x} D^n(x|y) e^{iq\cdot y}, \tag{2.34}$$

where $|\Lambda|$ denotes the number of space-time points. Eq. 2.34 can be brought into the form

$$\tilde{D}^n(p|q) = \delta(p-q)\left(m\mathbb{1} + \frac{i}{a}\sum_\mu \gamma_\mu \sin(p_\mu a)\right) \equiv \delta(p-q)\tilde{D}^n(p) \tag{2.35}$$

for free quarks. We can compute the quark propagator by inverting the Dirac operator, which gives

$$\left[\tilde{D}^n(p)\right]^{-1} = \frac{m\mathbb{1} - \frac{i}{a}\sum_\mu \gamma_\mu \sin(p_\mu a)}{m^2 + \frac{1}{a^2}\sum_\mu \sin^2(p_\mu a)}. \tag{2.36}$$

Particularly interesting is the massless case, which reproduces in the $a \to 0$ limit the continuum free quark propagator

$$\left[\tilde{D}^n(p)\right]^{-1}\Big|_{m=0} = \frac{-\frac{i}{a}\sum_\mu \gamma_\mu \sin(p_\mu a)}{\frac{1}{a^2}\sum_\mu \sin^2(p_\mu a)} \xrightarrow{a\to 0} \frac{-i\sum_\mu \gamma_\mu p_\mu}{p^2}, \tag{2.37}$$

where one can see that the continuum limit has one pole at $(0,0,0,0)$ whereas for the discretized version, we find 16 poles characterized by the individual momentum elements being either $p_\mu = 0$ or $p_\mu = \pi/a$. These 15 unphysical poles with $p \neq (0,0,0,0)$ are called doublers, and, in general, one wants to decouple them from the continuum theory. In [12], Wilson suggested a solution to this doubler problem by adding the so-called Wilson term to the naive discretization. The Wilson term reads

$$-a\sum_\mu \frac{U_\mu(x)_{ab}\delta_{x+a\hat{\mu},y} - 2\delta_{ab}\delta_{x,y} + U^\dagger_\mu(x-a\hat{\mu})_{ab}\delta_{x-a\hat{\mu},y}}{2a^2}, \tag{2.38}$$

which is the discretization of $-\frac{a}{2}\partial_\mu\partial_\mu$ and vanishes for $a \to 0$. This term has the effect that doublers gain the mass $m + 2\ell/a$, where ℓ denotes the number of momentum components with the value $p_\mu = \pi/a$. For small lattice spacings, the doublers become heavy and decoupled from the theory's low modes. The final **Wilson Dirac operator** is then

$$\begin{aligned} D^W_{\substack{\alpha\beta \\ ab}}(x|y) = \left(m + \frac{4}{a}\right)\delta_{\alpha\beta}\delta_{ab}\delta_{x,y} - \frac{1}{2a}\sum_\mu \big[&(\mathbb{1} - \gamma_\mu)_{\alpha\beta} U_\mu(x)_{ab}\delta_{x+a\hat{\mu},y} \\ &+ (\mathbb{1} + \gamma_\mu)_{\alpha\beta} U^\dagger_\mu(x-a\hat{\mu})_{ab}\delta_{x-a\hat{\mu},y}\big], \end{aligned} \tag{2.39}$$

and is embedded in the Wilson fermionic action

$$S^W_F[\bar{\psi},\psi,U] = a^4 \sum_{x,y\in\Lambda} \bar{\psi}(x) D^W(x|y)\psi(y), \tag{2.40}$$

with implicit matrix-vector multiplications in the color and spin space.

2.5. Chiral Symmetry in QCD

This section follows the arguments made in [6]. The Wilson term breaks one fundamental symmetry of massless QCD, the chiral symmetry. In Sec. 2.6, we will introduce domain-wall fermions, a fermion discretization which strongly mitigates the chiral symmetry breaking. This section briefly introduces chiral symmetry in QCD and aims to motivate the necessity of domain-wall fermions.

First, suppose that we have N_f flavors of massless quarks. The QCD action is invariant under chiral rotations for these massless fermions, which come in two types: vector and axial vector transformations. The symmetry group for each of these transformations is the unitary group $U(N_f)$ and can be expressed as the direct product $U(1) \otimes SU(N_f)$, where $SU(N_f)$ contains all special unitary $N_f \times N_f$ matrices with $\det(U) = 1$. The algebra of $SU(N_f)$ has in total $N_f^2 - 1$ generators labeled T_i for $i = 1, \ldots, N_f^2 - 1$. The chiral vector transformations are

$$\Psi'(x) = e^{i\alpha \mathbb{1}} \Psi(x), \quad \bar{\Psi}'(x) = \bar{\Psi}(x) e^{-i\alpha \mathbb{1}}, \tag{2.41}$$

$$\Psi'(x) = e^{i\alpha T_i} \Psi(x), \quad \bar{\Psi}'(x) = \bar{\Psi}(x) e^{-i\alpha T_i}, \tag{2.42}$$

where the first and second line denotes the $U_V(1)$ and $SU_V(N_f)$ rotations, respectively. Note that the fermionic vectors Ψ and $\bar{\Psi}$ carry color, spin, and flavor indices. The chiral or axial vector rotations are defined as

$$\Psi'(x) = e^{i\alpha \gamma_5 \mathbb{1}} \Psi(x), \quad \bar{\Psi}'(x) = \bar{\Psi}(x) e^{i\alpha \gamma_5 \mathbb{1}}, \tag{2.43}$$

$$\Psi'(x) = e^{i\alpha \gamma_5 T_i} \Psi(x), \quad \bar{\Psi}'(x) = \bar{\Psi}(x) e^{i\alpha \gamma_5 T_i}, \tag{2.44}$$

where the first and second line represent $U_A(1)$ and $SU_A(N_f)$ rotations, respectively.

As aforementioned, the QCD action for N_f massless fermions is invariant under all of these transformations of the group $SU_V(N_f) \otimes SU_A(N_f) \otimes U_V(1) \otimes U_A(1)$. However, for the path integral, we observe that the $U_A(1)$ symmetry is explicitly broken by the path integral's measure, resulting in the so-called axial anomaly. Another observation is that even though the action is invariant under $SU_A(N_f)$ rotations, the ground state of the theory is not. This phenomenon is called spontaneous symmetry breaking, and its order parameter is the chiral condensate, which is defined as

$$\langle \bar{\psi}(x) \psi(x) \rangle. \tag{2.45}$$

A key aspect of spontaneous symmetry breaking is that it produces massless Nambu-Goldstone bosons. In the case of $SU_A(2)$ chiral symmetry, these bosons manifest as pions. However, because physical quark masses introduce a slight explicit breaking of $SU_A(2)$, the pions acquire a small mass relative to the QCD scale Λ_{QCD}. In this context, the pions are called pseudo-Nambu-Goldstone bosons. Similar consideration can be given for $SU_A(3)$ with the pseudo-Nambu-Goldstone bosons being pions, kaons, and the η meson. However, the explicit symmetry breaking due to the strange quark mass is more substantial than for the $SU_A(2)$ case.

2.6. Möbius Domain-Wall Fermions

The chiral invariance of the massless QCD action yields the anti-commutator relation

$$D\gamma_5 + \gamma_5 D = 0, \tag{2.46}$$

with the continuum Dirac operator $D = \sum_\mu \gamma_\mu(\partial_\mu + igA_\mu)$. As discussed previously, the Wilson term noted in Eq. 2.38 violates chiral symmetry, which results in the Wilson-Dirac operator not fulfill Eq. 2.46. In 1981, Nielsen and Ninomiya established the no-go theorem, which states that it is impossible to have a fermion discretization on the lattice that is free of doublers while simultaneously satisfying Eq. 2.46, locality, hermiticity, and translational symmetry [13–15].
Ginsparg and Wilson suggested one way around this no-go theorem in [16]. The idea is that instead of fulfilling Eq. 2.46, the discrete Dirac operator has to fulfill the Ginsparg-Wilson equation given by

$$D\gamma_5 + \gamma_5 D = aD\gamma_5 D, \tag{2.47}$$

which recovers Eq. 2.46 for $a \to 0$. Furthermore, modifying the chiral rotation on the lattice to

$$\begin{aligned} \psi'(x) &= \sum_y \exp\left(i\alpha\gamma_5\left(\mathbb{1} - \frac{a}{2}D(x|y)\right)\right)\psi(y), \\ \bar{\psi}'(x) &= \sum_y \bar{\psi}(y)\exp\left(i\alpha\left(\mathbb{1} - \frac{a}{2}D(y|x)\right)\gamma_5\right) \end{aligned} \tag{2.48}$$

yields the invariance under these modified chiral rotations if the Dirac operator D satisfies the Ginsparg-Wilson equation (c.f. Eq. 2.47). Note that we assumed only one flavor for the modified chiral rotation in Eq. 2.48. If we want to add different flavors, we must include N_f generators, like, $\mathbb{1}$ and T_i.
A discrete Dirac operator satisfying Eq. 2.47 is the overlap operator expressed as

$$D_{\text{ov}} = \frac{1+m}{2}\mathbb{1} + \frac{1-m}{2}\gamma_5 \text{sign}[H], \tag{2.49}$$

where H denotes a Hermitian kernel operator [17–23]. Due to the computational cost of calculating the sign function in Eq. 2.49, an approximate overlap fermion discretization known as domain-wall fermions is frequently favored. In the following, we will specifically introduce Möbius domain-wall fermions. Moreover, by the end of this brief overview, we will demonstrate that domain-wall fermions have a connection with overlap fermions.
For the following, we will follow [24]. The basic idea of domain-wall fermions is to introduce an extra fifth dimension with the index $s = 0, 1, \ldots, L_s$, in which the left- and right-handed fermions are localized. In our setup, which follows [25], we label 5-dimensional fermionic fields by Ψ and $\bar{\Psi}$, and we get for the left- and right-handed states

$$\psi_L(x) = P_-\Psi(x, 0) \quad \text{and} \quad \psi_R(x) = P_+\Psi(x, L_s - 1), \tag{2.50}$$

with $P_\pm = \frac{1}{2}(\mathbb{1} \pm \gamma_5)$ denoting the chiral projection. Before introducing the domain-wall fermionic action, we redefine the Wilson operator

$$D^W(x|y) = (4 + M_5)\delta_{x,y} - \frac{1}{2}\left[(\mathbb{1} - \gamma_\mu)U_\mu(x)\delta_{x+a\hat{\mu},y} + (\mathbb{1} + \gamma_\mu)U_\mu^\dagger(y)\delta_{x-a\hat{\mu},y}\right], \tag{2.51}$$

where M_5 is a negative real mass, which does not correspond to the fermion mass. The domain-wall fermionic action can then be constructed by

$$S_F^{DW}[\bar{\Psi}, \Psi, U] = \sum_{x,y,s,q} \bar{\Psi}(x,s) D^{\mathrm{DW}}(x,s|y,q) \Psi(y,q) \tag{2.52}$$

with the Möbius domain-wall operator

$$\begin{aligned} D^{DW}(x,s|y,r) =& D_+(x|y)\delta_{sr} + D_-(x|y)\left(\delta_{s+1,r}P_+ + \delta_{s-1,r}P_-\right) \\ & - mD_-(x|y)\left(\delta_{s,0}\delta_{r,L_s-1}P_+ - \delta_{s,L_s-1}\delta_{r,0}P_-\right) \end{aligned} \tag{2.53}$$

and the auxiliary operators $D_+ = bD^W + 1$ and $D_- = cD^W - 1$. Following [24], we can express the 4-dimensional projected fermion field as

$$\psi(x) = P_-\Psi(x,0) + P_+\Psi(x, L_s - 1). \tag{2.54}$$

The connection between domain wall and overlap can be seen by considering the effective overlap operator

$$D_{\mathrm{ov}}^{L_s} = \frac{1+m}{2}\mathbb{1} + \frac{1-m}{2}\gamma_5 \epsilon_{L_s}\left[\gamma_5 D^{\mathrm{Möbius}}\right], \tag{2.55}$$

where ϵ_{L_s} denotes an approximation of the sign function and the Möbius kernel given by

$$D^{\mathrm{Möbius}} = \frac{(b+c)D^W}{2 + (b-c)D^W}. \tag{2.56}$$

Using the polar approximation of the sign function, we obtain for ϵ_{L_s} that [24]

$$\epsilon_{L_s}[H_5] = \frac{(1+H_5)^{L_s} - (1-H_5)^{L_s}}{(1+H_5)^{L_s} + (1-H_5)^{L_s}}, \tag{2.57}$$

with $H_5 = \gamma_5 D^{\mathrm{Möbius}}$. The approximation ϵ_{L_s} has thereby the property that

$$\lim_{L_s \to \infty} \varepsilon_{L_s}[H_5] = \mathrm{sign}[H_5]. \tag{2.58}$$

The equivalence between overlap fermions and domain-wall fermions is strictly valid only in the limit of $L_s \to \infty$. For finite values of L_s, there is inevitably some level of chirality breaking. The residual mass m_{res} serves as a measure of this chirality breaking, although we will not discuss m_{res} further here and instead refer the reader to [24] for further details. However, empirical evidence suggests that for values of L_s around $\mathcal{O}(10)$, the effects of chirality breaking are sufficiently mitigated. This mitigation of chirality breaking is the primary reason for the use of domain-wall fermions throughout this thesis.

2.7. Wick's Theorem

In the previous sections, we explored various methods for discretizing QCD on the lattice. After establishing the QCD action on the lattice, the next task is the evaluation of the path integral in Eq. 2.21 for a given operator $\mathcal{O}$. This section examines the scenario where the operator is composed of a collection of fermionic operators. Initially, we decompose

the path integral from Eq. 2.21 into a gluonic component and a fermionic component, yielding

$$\langle\langle\mathcal{O}\rangle_F\rangle_G = \frac{1}{Z}\int\mathcal{D}[U]\left(\frac{1}{Z_F[U]}\int\mathcal{D}[\bar{\psi},\psi]e^{-S_F[\bar{\psi},\psi,U]}\mathcal{O}[\bar{\psi},\psi,U]\right)Z_F[U]e^{-S_G[U]}, \tag{2.59}$$

$$= \frac{1}{Z}\int\mathcal{D}[U]\,\langle\mathcal{O}\rangle_F\,Z_F[U]e^{-S_G[U]} \tag{2.60}$$

where the action is expressed as a sum of gluonic and fermionic parts, specifically $S[\bar{\psi},\psi,U] = S_F[\bar{\psi},\psi,U] + S_G[U]$. Additionally, we characterize the fermion partition function as

$$Z_F[U] = \int\mathcal{D}[\bar{\psi},\psi]e^{-S_F[\bar{\psi},\psi]}. \tag{2.61}$$

In this section, we will focus on the fermionic path integral expressed as

$$\langle\mathcal{O}\rangle_F = \frac{1}{Z_F[U]}\int\mathcal{D}[\bar{\psi},\psi]e^{-S_F[\bar{\psi},\psi,U]}\mathcal{O}[\bar{\psi},\psi,U]. \tag{2.62}$$

Rather than considering a generic operator $\mathcal{O}$, we consider the expectation values of fermion field products described by

$$\langle\mathcal{O}_F\rangle_F = \left\langle \underset{a_1}{\overset{\alpha_1}{\psi^{(f_1)}}}(x_1)\underset{a_2}{\overset{\alpha_2}{\psi^{(f_2)}}}(x_2)\ldots\underset{a_n}{\overset{\alpha_n}{\psi^{(f_n)}}}(x_n)\underset{b_1}{\overset{\beta_1}{\bar{\psi}^{(g_1)}}}(y_1)\underset{b_2}{\overset{\beta_2}{\bar{\psi}^{(g_2)}}}(y_2)\ldots\underset{b_n}{\overset{\beta_n}{\bar{\psi}^{(g_n)}}}(y_n)\right\rangle_F, \tag{2.63}$$

where α_i,β_i are spin indices, a_i,b_i are color indices, and f_i,g_i are flavor indices. The fermion fields are located at x_i and y_i. Since fermions obey Fermi-Dirac statistics, they are subject to anti-commutation, reflected in the rules

$$\begin{aligned}
\underset{a}{\overset{\alpha}{\psi^{(f)}}}(x)\underset{b}{\overset{\beta}{\psi^{(g)}}}(y) &= -\underset{b}{\overset{\beta}{\psi^{(g)}}}(y)\underset{a}{\overset{\alpha}{\psi^{(f)}}}(x)\\
\underset{a}{\overset{\alpha}{\bar{\psi}^{(f)}}}(x)\underset{b}{\overset{\beta}{\bar{\psi}^{(g)}}}(y) &= -\underset{b}{\overset{\beta}{\bar{\psi}^{(g)}}}(y)\underset{a}{\overset{\alpha}{\bar{\psi}^{(f)}}}(x)\\
\underset{a}{\overset{\alpha}{\psi^{(f)}}}(x)\underset{b}{\overset{\beta}{\bar{\psi}^{(g)}}}(y) &= -\underset{b}{\overset{\beta}{\bar{\psi}^{(g)}}}(y)\underset{a}{\overset{\alpha}{\psi^{(f)}}}(x).
\end{aligned} \tag{2.64}$$

for general indices and positions. The anticommutation properties of fermion fields allow us to organize the fields by flavor such that

$$\langle\mathcal{O}_F\rangle_F = \left\langle\prod_f\mathcal{O}_F^{(f)}\right\rangle_F, \tag{2.65}$$

where each flavor-specific operator is given by

$$\mathcal{O}_F^{(f)} = \underset{a_1}{\overset{\alpha_1}{\psi^{(f)}}}(x_1)\underset{a_2}{\overset{\alpha_2}{\psi^{(f)}}}(x_2)\ldots\underset{a_{n_f}}{\overset{\alpha_{n_f}}{\psi^{(f)}}}(x_{n_f})\underset{b_1}{\overset{\beta_1}{\bar{\psi}^{(f)}}}(y_1)\underset{b_2}{\overset{\beta_2}{\bar{\psi}^{(f)}}}(y_2)\ldots\underset{b_{n_f}}{\overset{\beta_{n_f}}{\bar{\psi}^{(f)}}}(y_{n_f}). \tag{2.66}$$

Using $S_F[\bar{\psi},\psi,U] = \sum_f\bar{\psi}^{(f)}D^{(f)}\psi^{(f)} = \sum_f S_F^{(f)}[\bar{\psi}^{(f)},\psi^{(f)},U]$, we can factor the expectation value of Eq. 2.62 for the operator $\mathcal{O}_F$ into the expectation values of single flavors in the form of

$$\langle\mathcal{O}_F\rangle_F = \prod_f\left\langle\mathcal{O}_F^{(f)}\right\rangle_f, \tag{2.67}$$

with

$$\left\langle \mathcal{O}_F^{(f)} \right\rangle_f = \frac{1}{Z_F^{(f)}} \int \mathcal{D}[\bar{\psi}^{(f)}, \psi^{(f)}] e^{-S_F^{(f)}[\bar{\psi}^{(f)}, \psi^{(f)}, U]} \mathcal{O}_F^{(f)}[\bar{\psi}^{(f)}, \psi^{(f)}, U] \tag{2.68}$$

and the partition function $Z_F^{(f)}$ consisting of the same integral with $\mathcal{O}_F^{(f)} = 1$. Due to this factorability, we will only focus on fermion operators with single flavors in the remainder of this section.

The anticommutative nature described in Eq. 2.64 enables us to apply Grassmann numbers to represent fermion fields. A set of Grassmann numbers, labeled η_i for $i = 1, \ldots, N$, follows the rule

$$\eta_i \eta_j = -\eta_j \eta_i \tag{2.69}$$

for every index pair i, j. This section outlines findings from calculations involving Grassmann numbers. For more information on how these numbers are handled and their properties, consult [6]. By swapping fermion fields for Grassmann numbers, the fermionic action can be expressed as

$$S_F[\bar{\eta}, \eta] = \sum_{ij} \bar{\eta}_i D_{ij} \eta_j, \tag{2.70}$$

where $\bar{\eta}_j$ constitutes another set of Grassmann numbers related to the $\bar{\psi}$-fields, and i, j integrates spin, color, and position into a unified index. The gauge field dependency U is omitted for simpler calculations, but it is crucial to note that all results will implicitly depend on U.

The fermion partition function utilizing Grassmann numbers is represented by the Matthews-Salam formula:

$$Z_F = \int \mathrm{d}\eta_N \mathrm{d}\bar{\eta}_N \cdots \mathrm{d}\eta_1 \mathrm{d}\bar{\eta}_1 \exp\left(\sum_{i,j=1}^{N} \bar{\eta}_i D_{ij} \eta_j \right) = \det[D], \tag{2.71}$$

known as the fermion determinant. To compute expressions for general fermion expectation values, we introduce the generating functional with two additional sets of N Grassmann numbers θ_i and $\bar{\theta}_i$. This functional is defined as:

$$W[\bar{\theta}, \theta] = \int \prod_i \mathrm{d}\eta_i \mathrm{d}\bar{\eta}_i \exp\left(\sum_{k,l=1}^{N} \bar{\eta}_k D_{kl} \eta_l + \sum_{k=1}^{N} \bar{\theta}_k \eta_k + \sum_{k=1}^{N} \bar{\eta}_k \theta_k \right). \tag{2.72}$$

Carrying out the integrals yields

$$W[\bar{\theta}, \theta] = \det[D] \exp\left(- \sum_{n,m=1}^{N} \bar{\theta}_n (D^{-1})_{nm} \theta_m \right). \tag{2.73}$$

The generating functional can be used to express expectation values of Grassmann numbers as

$$\langle \eta_{i_1} \bar{\eta}_{j_1} \ldots \eta_{i_n} \bar{\eta}_{j_n} \rangle_F = \frac{1}{Z_F} \frac{\partial}{\partial \theta_{j_1}} \frac{\partial}{\partial \bar{\theta}_{i_1}} \cdots \frac{\partial}{\partial \theta_{j_n}} \frac{\partial}{\partial \bar{\theta}_{i_n}} W[\bar{\theta}, \theta] \Big|_{\theta, \bar{\theta}=0}. \tag{2.74}$$

Generally, performing this computation results in the renowned **Wick's theorem**, which is expressed as

$$\langle \eta_{i_1} \bar{\eta}_{j_1} \ldots \eta_{i_n} \bar{\eta}_{j_n} \rangle_F = (-1)^n \sum_{P(1,2,\ldots,n)} \mathrm{sign}(P) (D^{-1})_{i_1, j_{P_1}} (D^{-1})_{i_2, j_{P_2}} \ldots (D^{-1})_{i_n, j_{P_n}}, \tag{2.75}$$

where $P(1, 2, \ldots, n)$ denotes all permutations of $1, 2, \ldots, n$. The quark propagator, which will be discussed in subsequent sections, is the inverse of the Dirac operator D.
Using Wick's theorem, we deduce that the fermionic expectation value is represented as a sum of products involving quark propagators, which depend on the gauge field U. To finalize the evaluation of Eq. 2.14, the following integral must be calculated:

$$\langle \mathcal{O} \rangle = \frac{1}{Z} \int \mathcal{D}[U] O_f[U] \det \left[D^{(f)}[U] \right] e^{-S_G[U]}, \tag{2.76}$$

where $O_f[U] = \langle \mathcal{O}_F^{(f)}[U] \rangle_f$. The evaluation of this integral is carried out numerically using Monte Carlo methods. The procedure involves generating N gauge configurations U_i for $i = 1, \ldots, N$, which are distributed following the probability $P(U) = \prod_f \det \left[D^{(f)}[U] \right] e^{-S_G[U]}$. This technique allows for the approximation of the integral as:

$$\langle \mathcal{O} \rangle \approx \frac{1}{N} \sum_{i=1}^{N} \prod_f O_f[U_i]. \tag{2.77}$$

The set of gauge configurations U_i is known as the ensemble. Due to the substantial computational expense associated with calculating the fermion determinant, setting $\det \left[D^{(f)} \right] = 1$ is a common practice for heavier quarks, effectively disabling the sea quarks of that flavor. When all fermion determinants are set to one, Eq. 2.76 is evaluated in what is known as the quenched approximation. This thesis exclusively employs ensembles where the fermion determinants for light quarks, specifically up- and down-quarks, alongside the strange quark, are calculated, commonly called $(2 + 1)$ fermion ensembles. Here, 2 refers to the equal masses of the up- and down-quarks in our ensembles. There are various effective strategies for generating ensembles with and without sea quarks. For nonquenched ensembles, the Hybrid Monte Carlo algorithm is frequently used to generate gauge configurations. However, since this thesis relies on pre-established gauge configurations from the RBC/UKQCD collaborations (see Sec. 5.1 for more information), an in-depth discussion of ensemble generation is not included, although [6, 26] is suggested for readers seeking more details.

2.8. Quark Propagator and Smearing

As shown in Eq. 2.75, the expectation values of fermionic operators can be represented as sums of products of quark propagators defined by

$$F_{\substack{\alpha\beta \\ ab}}(x|y) = \left\langle \psi^{(f)}_{\substack{\alpha \\ a}}(x) \bar{\psi}^{(f)}_{\substack{\beta \\ b}}(y) \right\rangle = \left[D^{(f)} \right]^{-1}_{\substack{\alpha\beta \\ ab}}(x|y), \tag{2.78}$$

where the capital letter F is substituted with the corresponding flavor label, for instance, a propagator for an up quark is denoted by $U(x|y)$, and so forth. The discretized Dirac operator can generally be represented by a matrix of dimensions $(V \cdot 4 \cdot 3) \times (V \cdot 4 \cdot 3)$. This matrix is notably large for practical lattice sizes. Although the Dirac operator itself is sparse, its inverse is not, making it impractical to compute the propagator across all space-time configurations.

A typical solution is to solve the quark propagator for specific sources V^i, where we use i to label different source specifications. The propagator F^i is then the solution of

$$DF^i = V^i, \tag{2.79}$$

which is

$$F^i_{\substack{\alpha \\ a}}(x) = \sum_{y,\beta,b} \left[D^{(f)}\right]^{-1}_{\substack{\alpha\beta \\ ab}} V^i_{\substack{\beta \\ b}}(y). \tag{2.80}$$

Eq. 2.79 is generally addressed through Krylov subspace techniques, including conjugate gradient [27], BiCGStab [28], GMRES [29], or through state-of-the-art multigrid approaches [30]. In this thesis, we consistently employ an optimized form of conjugate gradient[1]. The source can be vector-like as shown in Eq. 2.80 or matrix-like. An example of a matrix-like source is the point source, defined as

$$V^{(y_0)}_{\substack{\beta\beta_0 \\ bb_0}}(y) = \delta(y - y_0)\delta_{\beta\beta_0}\delta_{bb_0}. \tag{2.81}$$

In the study of hadron spectroscopy, as elaborated in Sec. 2.10, the use of non-local sources can often be more advantageous. A straightforward generalization of point sources is the use of sums of point sources, referred to as box sources. These are defined by the equation

$$V^{(\tilde{y},N)}_{\substack{\beta\beta_0 \\ bb_0}}(y) = \sum_{y' \in B(\tilde{y},N)} \delta(y' - y)\delta_{\beta\beta_0}\delta_{bb_0}, \tag{2.82}$$

where the three-dimensional box comprises lattice points with spatial coordinates $y_i = (\tilde{y}_i + k_i a) \bmod L$, with $k_i = 0, 1, \ldots, L$, and sharing the temporal coordinate with $\tilde{y}$. A drawback of box sources is their lack of gauge invariance, which requires gauge fixing, which is covered in Sec. 2.9. The scenario in which the box encompasses all spatial points in a specific time slice is called a wall source. Point, box, and wall sources are predominantly used in Ch. 6.
In addition to box sources, there is also a way to create non-local gauge-invariant sources. An example is Gaussian smeared sources introduced in [31]. The idea is to smear a point source with the Gaussian smearing operator

$$G(n, \sigma) = \left(1 + \frac{\sigma^2}{4n}\Delta\right)^n, \tag{2.83}$$

with the three-dimensional Laplace operator

$$\Delta(U, D)\psi(x) = \sum_{\mu=0}^{2} \frac{U_\mu(x)\psi(x + a\hat{\mu}) + U^\dagger_\mu(x - a\hat{\mu})\psi(x - a\hat{\mu}) - 2\psi(x)}{2a}, \tag{2.84}$$

the smearing parameter σ, and the number of smearing steps n. Another smearing procedure, which is heavily used throughout this thesis, is the distillation method, which has its own dedicated section (cf. Sec. 5.7).

[1] Example code for the calculation of quark propagators in the distillation framework can be found under https://github.com/lehner/gpt/blob/master/applications/distillation/64I-peramb.py

Due to symmetry considerations, it is advantageous to not only identify a source but also define a sink $\left[V_{\substack{\alpha \\ a}}^{j}(x)\right]^{\dagger}$, thus establishing the propagator between source and sink as

$$F^{ji} = \sum_{x,\alpha,a} \sum_{y,\beta,b} \left[V_{\substack{\alpha \\ a}}^{j}(x)\right]^{\dagger} \left[D^{(f)}\right]^{-1}_{\substack{\alpha\beta \\ ab}}(x|y) V_{\substack{\beta \\ b}}^{i}(y). \tag{2.85}$$

The introduction of sinks is particularly beneficial for techniques that require identical operators at both the source and the sink, such as the GEVP method (see Sec. 5.9). Note that the propagator introduced in Eq. 2.80 is equivalent to a point sink in Eq. 2.85.
A useful property of the aforementioned propagators is the so-called γ_5-hermicity stating

$$\gamma_5 F \gamma_5 = F^{\dagger}, \tag{2.86}$$

where the adjoint operations act on spin and color indices and the positions which lead to the component representation

$$(\gamma_5)_{\alpha\alpha'} F_{\substack{\alpha'\beta' \\ ab}}(x|y)(\gamma_5)_{\beta'\beta} = \left[F_{\substack{\beta\alpha \\ ba}}(y|x)\right]^{*}, \tag{2.87}$$

with an implicit sum over repeated indices.

2.9. Gauge Fixing

As noted, the box source specified in Eq. 2.82 lacks gauge invariance. However, as long as the gauge-invariant information is still in the correlation function, we obtain this gauge-invariant part as a signal. For a sufficiently large sample over the gauge orbit, that is, the set of configurations connected via gauge transformation, the gauge-dependent contributions do not contribute to the mean, but add noise. Using Monte Carlo integration, we naturally sample over the gauge orbit. Hence, by fixing the gauge degree of freedom, we can enhance the signal of our observable [32].
In this thesis, the Coulomb gauge fixing is employed, represented by the continuum expression

$$\sum_i \partial_i A_i = 0, \tag{2.88}$$

where i signifies the spatial dimensions. Gauge fixing fundamentally involves using the local gauge transformation $\Omega(x)$ to satisfy the specified gauge fixing conditions. Specifically, for Coulomb gauge fixing, the condition involves identifying a field $\Omega(x) \in SU(3)$ such that the functional

$$F_U[\Omega] = \frac{1}{4N_c|\Lambda|} \sum_x \sum_i \mathrm{Re}\,\mathrm{Tr}\Big\{\Omega(x) U_i(x) \Omega^{\dagger}(x + a\hat{i})\Big\} \tag{2.89}$$

reaches a stationary point with respect to Ω [33]. Since there are no links in the temporal direction, it is also possible to compute the gauge fixed gauge field for the individual time slices in parallel. The stationary point of Eq. 2.89 can be computed using standard optimization algorithms, whose performance can be measured by

$$\theta \equiv \frac{1}{3|\Lambda|} \sum_x \mathrm{Tr}\Big\{\Delta(x)\Delta^{\dagger}(x)\Big\}, \tag{2.90}$$

with the discrete derivative of the gauge fields

$$\Delta(x) = \sum_i \left(A_i(x) - A_i(x - a\hat{i}) \right), \tag{2.91}$$

with A being connected to U through $U_\mu = e^{igaA_\mu}$ [34][2].

2.10. Hadron Spectroscopy

In the following, we consider expectation values of two fermion operators $\mathcal{O}_1$ and $\mathcal{O}_2$ of the kind

$$C_{12}(x, y) = \left\langle \mathcal{O}_1(x) \mathcal{O}_2^\dagger(y) \right\rangle, \tag{2.92}$$

which we call two-point correlation function. Here, the operator $\mathcal{O}_2^\dagger(y)$ creates states at position y and $\mathcal{O}_1$ destroys states at x. It is emphasized that both operators often overlap not just with one state but with a tower of states sharing the same quantum numbers as the operator. We will discuss these tower of states more in the following sections.
Often it is more convenient to express Eq. 2.92 in the momentum representation. For this, we consider the discrete Fourier transformation and its inverse for an arbitrary function f:

$$\tilde{f}(\boldsymbol{p}, t) = \frac{1}{\sqrt{|\Lambda_3|}} \sum_{\boldsymbol{x} \in \Lambda_3} e^{-i\boldsymbol{p}\cdot\boldsymbol{x}} f(\boldsymbol{x}, t), \tag{2.93}$$

$$f(\boldsymbol{x}, t) = \frac{1}{\sqrt{|\Lambda_3|}} \sum_{\boldsymbol{p} \in \tilde{\Lambda}_3} e^{i\boldsymbol{p}\cdot\boldsymbol{x}} \tilde{f}(\boldsymbol{p}, t), \tag{2.94}$$

where Λ_3 denotes the set of all spatial lattice points and $\tilde{\Lambda}_3$ the set of all momenta on the lattice, which have the form $\boldsymbol{p} = \frac{2\pi}{aN}\boldsymbol{n}$ where $\boldsymbol{n}$ is a integer vector with entries $0 \leq n_i < N$ and N being the number of spacial lattice points in one direction. With the help of the Fourier transformation we can define the operator in momentum basis as

$$\tilde{\mathcal{O}}_1(\boldsymbol{p}, t) = \frac{1}{|\Lambda_3|} \sum_{\boldsymbol{x} \in \Lambda_3} e^{-i\boldsymbol{p}\cdot\boldsymbol{x}} \mathcal{O}_1(\boldsymbol{x}, t) \tag{2.95}$$

$$\tilde{\mathcal{O}}_2^\dagger(\boldsymbol{p}, t) = \frac{1}{|\Lambda_3|} \sum_{\boldsymbol{x} \in \Lambda_3} e^{i\boldsymbol{p}\cdot\boldsymbol{x}} \mathcal{O}_2^\dagger(\boldsymbol{x}, t). \tag{2.96}$$

In the following, we will use the operator in momentum basis as default, and therefore we drop the tilde notation for the operators. Eq. 2.92 in momentum space is then given by

$$C_{12}(t, t_0, \boldsymbol{p}) = \left\langle \mathcal{O}_1(\boldsymbol{p}, t_0 + t) \mathcal{O}_2^\dagger(\boldsymbol{p}, t_0) \right\rangle, \tag{2.97}$$

where both operators must have the same momentum due to momentum conservation and have a time separation of t.

[2] Code example for the gauge fixing can be found under https://github.com/lehner/gpt/blob/master/applications/gauge_fix/coulomb.py

We can express $C_{12}(t, t_0, \boldsymbol{p})$ in the trace representation from Eq. 2.16 to obtain

$$C_{12}(t, t_0, \boldsymbol{p}) = \frac{\sum_m \langle m|e^{-\hat{H}T}\hat{O}_1(\boldsymbol{p}, t+t_0)\hat{O}_2^\dagger(\boldsymbol{p}, t)|m\rangle}{\sum_m \langle m|e^{-\hat{H}T}|m\rangle}. \tag{2.98}$$

The use of the Heisenberg picture and that $\hat{H}\,|n\rangle = \mathcal{E}_n\,|n\rangle$ yields then

$$C_{12}(t, t_0, \boldsymbol{p}) = \frac{\sum_{mn} e^{-\mathcal{E}_m T} e^{-(\mathcal{E}_n - \mathcal{E}_m)t}\langle m|\mathcal{O}_1(\boldsymbol{p})|n\rangle\langle n|\mathcal{O}_2^\dagger(\boldsymbol{p})|m\rangle}{\sum_m e^{-\mathcal{E}_m T}}. \tag{2.99}$$

For a large temporal extent and a finite mass gap $E_1 = \mathcal{E}_1 - \mathcal{E}_0$ we can approximate Eq. 2.99 by

$$C_{12}(t, t_0, \boldsymbol{p}) \approx \sum_n \langle 0|\mathcal{O}_1(\boldsymbol{p})|n\rangle\langle n|\mathcal{O}_2^\dagger(\boldsymbol{p})|0\rangle e^{-E_n t}, \tag{2.100}$$

with $E_n = \mathcal{E}_n - \mathcal{E}_0$, where $\mathcal{E}_0$ denotes the vacuum energy.
We can use the correlation function to obtain information about the spectrum of the theory with overlap with the operators $\mathcal{O}_1$ and $\mathcal{O}_2$ by defining the so-called effective energy

$$aE_{\text{eff}}(t, n) = -\frac{1}{n}\log\left(\frac{C_{12}(t + na, t_0, \boldsymbol{p})}{C_{12}(t, t_0, \boldsymbol{p})}\right). \tag{2.101}$$

Using Eq. 2.100, we can approximate the effective energy by

$$aE_{\text{eff}}(t, n) = aE_1 + \gamma_2 \frac{1 - e^{-an\Delta E_2}}{n} e^{-\Delta E_2 t} + \mathcal{O}\left(e^{-\Delta E_3 t}\right) + \mathcal{O}\left(e^{-2\Delta E_2 t}\right), \tag{2.102}$$

with $\gamma_2 = \frac{\langle 0|\mathcal{O}_1|2\rangle\langle 2|\mathcal{O}_2^\dagger|0\rangle}{\langle 0|\mathcal{O}_1|1\rangle\langle 1|\mathcal{O}_2^\dagger|0\rangle}$ and $\Delta E_n = E_n - E_1$. From this form, we can see that the effective mass decays exponentially to a plateau at the energy of the combined ground state of $\mathcal{O}_1$ and $\mathcal{O}_2$ with the energy E_1. This behavior can be used to measure the energy of states in lattice QCD. In instances where both the source and sink operators are at rest, we consistently refer to the effective mass in our analysis of Eq. 2.101. Additionally, the ground state energy is then analogous to a mass and is denoted by $E_1 = M$. In Sec. 5.9 we will also discuss a more involved method to obtain spectral information, the so-called GEVP method. This method also allows us to make stronger statements about the excited states.

2.11. Nucleons and Pions on the Lattice

In this section, we examine operators $\mathcal{O}^\dagger$ which create pion or nucleon states, focusing on their two-point correlation function given by

$$C(t) = \langle \mathcal{O}(t)\mathcal{O}^\dagger(0)\rangle. \tag{2.103}$$

In the case of a generic pion, the interpolating operator can be expressed as

$$\mathcal{O}_\pi(x) = \bar{\psi}_j(x)\gamma_5\psi_i, \tag{2.104}$$

and upon application of Wick's theorem, it results in the expression

$$C_{\pi\pi}(t,\boldsymbol{p}) = \left\langle \mathcal{O}_\pi(\boldsymbol{p},t)\mathcal{O}_\pi^\dagger(\boldsymbol{p},0)\right\rangle \tag{2.105}$$

$$= -\sum_{\boldsymbol{x},\boldsymbol{y}} e^{-i\boldsymbol{p}\cdot(\boldsymbol{x}-\boldsymbol{y})} \left\langle \mathrm{tr}\left[G_j(x|y)\gamma_5 G_i(y|x)\gamma_5\right]\right\rangle , \tag{2.106}$$

where G_i denotes the quark propagator related to ψ_i, which is either an up- or down-quark. Normally, the γ_5-hermicity property of $G_i(y|x)$ (as outlined in Eq. 2.86) is used to formulate a computationally simpler version

$$C_{\pi\pi}(t,\boldsymbol{p}) = \sum_{\boldsymbol{x},\boldsymbol{y}} e^{-i\boldsymbol{p}\cdot(\boldsymbol{x}-\boldsymbol{y})} \left\langle \mathrm{tr}\left[G_j(x|y)G_i^\dagger(x|y)\right]\right\rangle , \tag{2.107}$$

utilizing the same source for both G_i and G_j. In lattice QCD, correlation functions are statistically estimated (see Sec. 5.2 for more details). Thus, we describe the results using the expectation value along with its standard deviation, often referred to as noise. Generally, the pion correlation function exhibits a favorable signal-to-noise ratio.
The same situation does not apply to the nucleon. We use the nucleon operator defined by

$$\mathcal{O}_N(x)_\alpha = \varepsilon_{abc}(P_+\psi_a(x))_\alpha \left[u_b(x)^T C\gamma_5 d_c(x)\right], \tag{2.108}$$

where ψ can be an up or down quark, depending on whether we are considering protons or neutrons. Using Eq. 2.108 we can derive the fully contracted correlation function expressed as

$$C_{NN}(t,\boldsymbol{p}) = \left\langle \mathcal{O}_N(\boldsymbol{p},t)\mathcal{O}_N^\dagger(\boldsymbol{p},0)\right\rangle \tag{2.109}$$

$$= \sum_{\boldsymbol{x},\boldsymbol{y}} e^{-i\boldsymbol{p}\cdot(\boldsymbol{x}-\boldsymbol{y})} \left\langle \mathrm{tr}\left[P^+\mathrm{tr}_c\left[\left(\mathrm{tr}_s\left[Q^{NN}(x|y)\right] + Q^{NN}(x|y)\right)G(x|y)\right]\right]\right\rangle , \tag{2.110}$$

where the diquark structure is given by

$$Q^{NN}_{\substack{\alpha\beta\\ a'a}}(x|y) = Q[U(x|y)C\gamma_5, C\gamma_5 D(x|y)]_{\substack{\alpha\beta\\ a'a}} \tag{2.111}$$

$$= \sum_{\gamma,b,c,b',c'} \varepsilon_{abc}\varepsilon_{a'b'c'} \left[U(x|y)C\gamma_5\right]_{\substack{\alpha\gamma\\ bb'}} \left[C\gamma_5 D(x|y)\right]_{\substack{\beta\gamma\\ cc'}} . \tag{2.112}$$

[35] and [36] demonstrated that it is possible to forecast the signal-to-noise ratio for a correlation function C, which is defined as

$$\mathrm{StN}(C) = \frac{\langle C\rangle}{\sqrt{\langle |C|^2\rangle}}. \tag{2.113}$$

In the context of the nucleon, the resulting signal-to-noise ratio is given by

$$\mathrm{StN}(C) = \frac{\langle \mathcal{O}_N(t)\mathcal{O}_N^\dagger(0)\rangle}{\sqrt{\langle \mathcal{O}_N^\dagger(t)\mathcal{O}_N(t)\mathcal{O}_N^\dagger(0)\mathcal{O}_N(0)\rangle}}. \tag{2.114}$$

The signal $\langle \mathcal{O}_N(t)\mathcal{O}_N^\dagger(0)\rangle$, can be approximated for large source-sink separations t by

$$\langle \mathcal{O}_N(t)\mathcal{O}_N^\dagger(0)\rangle \sim e^{-M_N t}, \tag{2.115}$$

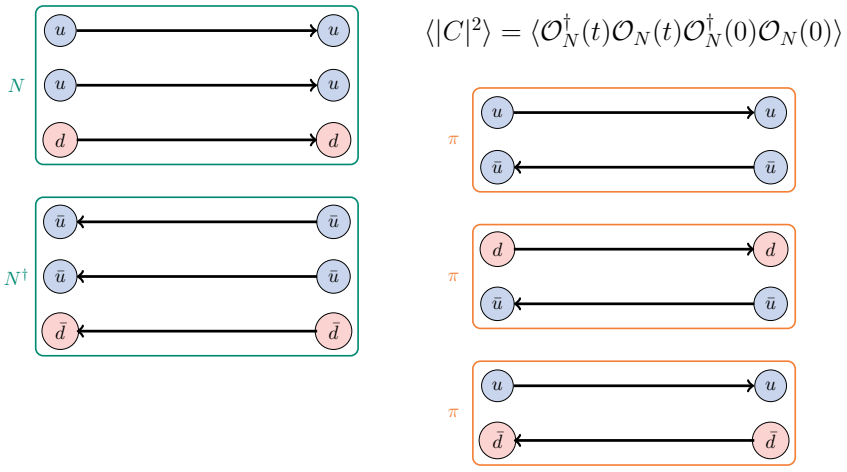

Figure 2.3.: Sketch of the origin of the signal-to-noise degradation of the nucleon correlation function. The left part of the picture shows the interpretation of the variance correlation function $\langle \mathcal{O}_N^\dagger(t)\mathcal{O}_N(t)\mathcal{O}_N^\dagger(0)\mathcal{O}_N(0)\rangle$ as the correlation of a nucleon and anti-nucleon pair. The right part of the pictures shows the interpretation of the correlation function of three pions.

since the lowest energy state is the nucleon. For the variance term $\langle \mathcal{O}_N^\dagger(t)\mathcal{O}_N(t)\mathcal{O}_N^\dagger(0)\mathcal{O}_N(0)\rangle$, we need to do a careful analysis of the two nucleon spectrum. Although a nucleon and an anti-nucleon propagating state is part of the spectrum, the same holds true for three propagating pions, as depicted in Fig. 2.3. However, for ensembles of physical relevance, it is observed that three pions are lighter compared to two nucleons, which leads to the approximate behavior of the variance correlation function given by

$$\langle \mathcal{O}_N^\dagger(t)\mathcal{O}_N(t)\mathcal{O}_N^\dagger(0)\mathcal{O}_N(0)\rangle \sim e^{-3m_\pi t}. \tag{2.116}$$

Merging the components, we find that the signal-to-noise ratio behaves according to

$$\mathrm{StN}(C) \sim e^{-(M_N - \frac{3}{2}m_\pi)t}, \tag{2.117}$$

implying that, at sufficiently large time intervals t, the noise dominates the signal. Consequently, in nucleon spectroscopy, obtaining maximal information from shorter time distances, where contributions from highly excited states are anticipated, is of critical importance. The remainder of this thesis will explore various approaches to address this issue.

3. Group Theory and Operator Construction

3.1. The Double-Cover of the Full Octahedral Group

In the following, we will discuss the basics of the group theory of finite groups, which covers the elemental principles required to understand the following chapters. For a more comprehensive introduction, we refer to standard textbooks like [8, 37], which is also the basis for this short introduction.
A group is defined as a set G together with a binary operation $*$ that satisfies the following properties:

1. **Closure:** For all $a, b \in G$, $a * b \in G$
2. **Associativity:** For all $a, b, c \in G$, $(a * b) * c = a * (b * c)$
3. **Identity:** There exists an element $e \in G$ such that for all $a \in G$, $a * e = e * a = a$
4. **Inverses:** For all $a \in G$, there exists an element $a^{-1} \in G$ such that $a * a^{-1} = a^{-1} * a = e$

First, we will focus on finite groups, i.e., groups with finite number of elements $|G|$. Such finite groups can be characterized by the multiplication table in which individual entries M_{ab} of the square matrix $|G| \times |G|$ are defined as $M_{ab} = a * b$.
Generally, we work with representations of a group G in a vector space V on the field K. A representation of a group G in a vector space V is defined as $\rho : G \to GL(V)$, where $GL(V)$ is the general linear group of V, which preserves the homomorphism property

$$\text{for all } a, b \in G : \rho(a * b) = \rho(a) \cdot \rho(b), \tag{3.1}$$

where $\cdot$ denotes the matrix multiplication. A representation is called reducible if we can find a unitary matrix U such that

$$U\rho(a)U^\dagger = \begin{pmatrix} \rho_1(a) & 0 \\ 0 & \rho_2(a) \end{pmatrix} = \rho_1(a) \oplus \rho_2(a) \quad \text{for all } a \in G. \tag{3.2}$$

The representation is called irreducible if it is not reducible. A useful measure of the representation of individual group elements $\rho(a)$ is the character $\chi_\rho(a)$ of the representation, which is defined as the trace of the representation matrix:

$$\chi_\rho(a) = \mathrm{Tr}[\rho(a)]. \tag{3.3}$$

We can order the group elements in conjugate classes defined by

$$\mathcal{C}_a = \left\{ gag^{-1} | g \in G \right\}, \tag{3.4}$$

where the character of the elements in the conjugate class is the same since

$$\chi_\rho(gag^{-1}) = \mathrm{Tr}[\rho(gag^{-1})] = \mathrm{Tr}[g\rho(a)g^{-1}] = \mathrm{Tr}[\rho(a)] = \chi_\rho(a). \tag{3.5}$$

Thus, it suffices to determine the character of representations for just one element within each conjugate class and to denote the character of the class λ by $\chi_\rho(\lambda)$. By employing Schur's lemma, we derive an orthogonality relation for the irreducible representations of the group G:

$$\langle\rho|\rho'\rangle \equiv \frac{1}{|G|}\sum_{a\in G}\chi^\star_\rho(a)\chi_{\rho'}(a) = \frac{1}{|G|}\sum_\lambda n_\lambda\chi^\star_\rho(\lambda)\chi_{\rho'}(\lambda) = \delta_{\rho\rho'}, \tag{3.6}$$

where n_λ represents the number of elements in the conjugacy class λ. Each representation σ can be expressed as a direct sum of irreducible representations ρ_i, i.e., $\sigma = \bigoplus_i \rho_i$, thus, the character of the representation σ is the sum of the characters of the irreducible representations ρ_i:

$$\chi_\sigma(a) = \sum_i \chi_{\rho_i}(a). \tag{3.7}$$

With the orthogonality relation in Eq. 3.6 the multiplicity of the irreducible representation ρ in the representation σ can be computed by

$$\langle\sigma|\rho\rangle \equiv \frac{1}{|G|}\sum_{a\in G}\chi^\star_\sigma(a)\chi_\rho(a) = \frac{1}{|G|}\sum_i\sum_{a\in G}\chi^\star_{\rho_i}(a)\chi_\rho(a) = \sum_i \delta_{\rho_i\rho}. \tag{3.8}$$

Furthermore, we can use the orthogonality relation to construct the projection operator $P_{\sigma\to\rho}$ onto the subspace of the irreducible representation ρ in the representation σ:

$$P_{\sigma\to\rho} = \frac{\dim[\rho]}{|G|}\sum_{a\in G}\chi^\star_\rho(a)\sigma(a), \tag{3.9}$$

where $\dim[\rho]$ is the dimension of the irreducible representation ρ. The eigenvalues of the projection operator are 1 or 0, and the eigenvectors corresponding to the eigenvalues 1 transform in the irreducible representation ρ. To reduce the degeneracy of the eigenvalues, it is often beneficial to calculate the eigenvectors of $\sigma(g)P_{\sigma\to\rho}$, which still transform in the irreducible representation ρ and are also the eigenvectors of $\sigma(g)$.

The aforementioned tools can now be applied to analyze the group theory associated with the lattice. For spectroscopy, we are interested in the eigenstates of the QCD-Hamiltonian. Hence, it is helpful to consider the Hamiltonian's symmetry. In the continuum, the Lorenz symmetry reduces to the group of three-dimensional rotations O_3. O_3 consists of the symmetry group of rotations $SO(3)$ and discrete parity transformations $\mathbb{Z}_2$, therefore O_3 is isomorphic to $SO(3)\otimes\mathbb{Z}_2$. In three dimensions, parity transformations reflect all coordinates, which can be easily discretized on the lattice. For the discretization of rotations, we must impose rotations by a multiple of 90°. This set of discretized rotations forms the finite group O isomorph to the symmetric group S_4, i.e., the group of all permutations of four elements. Combined with the $\mathbb{Z}_2$ parity symmetry, we end up with the full octahedral group $O_h \simeq O\otimes\mathbb{Z}_2$.
However, the continuum theory tells us that to describe half-integer spin states, we have

to consider the double cover of the rotational group $SO(3)$, which is $SU(2)$. The meaning of $SU(2)$ being the double cover of $SO(3)$ is that the mapping $f : SU(2) \to SO(3)$ has the property that $f(U) = f(-U)$ for every $U \in SU(2)$. Similarly, spin states on the lattice are described by the double cover of the full octahedral group O_h^d. Because O_h^d is finite, one can show that every group action can be generated by a repeated application of 90° rotations around two predefined directions, for example, the x and z directions and the parity transformation.
One way to find all group actions is to consider the action of a 90° rotation around the x and z axis on a spinor, given by

$$\psi(x) \xrightarrow{R_x} \psi'(x') = S_x \psi(R_x^T \boldsymbol{x}, t) = \frac{1}{\sqrt{2}} \left(\mathbb{1} + \gamma_z \gamma_y\right) \psi(R_x^T \boldsymbol{x}, t), \tag{3.10a}$$

$$\psi(x) \xrightarrow{R_z} \psi'(x') = S_z \psi(R_z^T \boldsymbol{x}, t) = \frac{1}{\sqrt{2}} \left(\mathbb{1} + \gamma_y \gamma_x\right) \psi(R_z^T \boldsymbol{x}, t), \tag{3.10b}$$

and its transformational behavior under parity:

$$\psi(x) \xrightarrow{P} \psi'(x') = \gamma_t \psi(-\boldsymbol{x}, t). \tag{3.10c}$$

The representation matrices can be computed similarly as described in [9] by translating everything into the Euclidean metric. With repeated use of the transformations introduced in Eq. 3.10, we can find the representation for all 96 group elements, which then can be used to calculate all irreducible representations, as shown above. The character table of O_h^d, which consists of the character of each irreducible representation and each class, is shown in Tab. 3.1. There, we can see that O_h^d has in total 16 irreducible representations structured in the following way: Each irreducible representation has either even (g) or odd (u) parity and has a counter irrreducible representation, which behaves the same under rotations but different under parity transformations. Excluding parity, we get five bosonic irreducible representations, A_1, A_2, E, T_1, and T_2 and three fermionic irreducible representations, G_1, G_2, and H. Bosonic irreducible representations are also irreducible representations of O and are discretized representatives of the integer spin states in the continuum. Likewise, the fermionic irreducible representations represent half-integer states. The dimensions of the individual irreducible representations can be read off by the character of the identity shown in the second column of the table. The values of the character table are checked against the values in Tab. 6.5 of [38].

By discretizing the space, we reduce the countable infinite irreducible representations $\{\ell\}$ of $SU(2)$, where ℓ denotes the spin, to the eight irreducible representations of O^d. Given that we can recover the continuum as $a \to 0$ and $L \to \infty$, it is necessary for the information of the $SU(2)$ irreducible representations to be integrated within the O_h^c irreducible representations. In essence, the $SU(2)$ irreducible representations are subduced into the lattice irreducible representations [39]. We do not consider parity since it is preserved during subduction. The character of the trivial representation is always 1. Hence, we can infer that $\{0\}$ subduces to A_1. Furthermore, comparing the representation of $\{\frac{1}{2}\}$ with G_1, we find that $\{\frac{1}{2}\}$ subduces to G_1. The subduction of the remaining irreducible representations can be computed iteratively by using the relation

$$\chi_{\ell+\frac{1}{2}}(g) = \chi_\ell(g)\chi_{\frac{1}{2}}(g) - \chi_{\ell-\frac{1}{2}}(g), \tag{3.11}$$

Irrep \ Class	I	R	P	R^2	RR'	RP	R^3	R^2R'	R^2P	R^4	R^3R'	R^3P	R^4P	PRR'	$R^2R'P$	$R'R^3P$
A_{1g}	1	1	1	1	1	1	1	1	1	1	1	1	1	1	1	1
A_{1u}	1	1	−1	1	1	−1	1	1	−1	1	1	−1	−1	−1	−1	−1
A_{2g}	1	−1	1	1	1	−1	−1	−1	1	1	1	−1	1	1	−1	1
A_{2u}	1	−1	−1	1	1	1	−1	−1	−1	1	1	1	−1	−1	1	−1
E_g	2	0	2	2	−1	0	0	0	2	2	−1	0	2	−1	0	−1
E_u	2	0	−2	2	−1	0	0	0	−2	2	−1	0	−2	1	0	1
T_{1g}	3	1	3	−1	0	1	1	−1	−1	3	0	1	3	0	−1	0
T_{1u}	3	1	−3	−1	0	−1	1	−1	1	3	0	−1	−3	0	1	0
T_{2g}	3	−1	3	−1	0	−1	−1	1	−1	3	0	−1	3	0	1	0
T_{2u}	3	−1	−3	−1	0	1	−1	1	1	3	0	1	−3	0	−1	0
G_{1g}	2	$\sqrt{2}$	2	0	1	$\sqrt{2}$	$-\sqrt{2}$	0	0	−2	−1	$-\sqrt{2}$	−2	1	0	−1
G_{1u}	2	$\sqrt{2}$	−2	0	1	$-\sqrt{2}$	$-\sqrt{2}$	0	0	−2	−1	$\sqrt{2}$	2	−1	0	1
G_{2g}	2	$-\sqrt{2}$	2	0	1	$-\sqrt{2}$	$\sqrt{2}$	0	0	−2	−1	$\sqrt{2}$	−2	1	0	−1
G_{2u}	2	$-\sqrt{2}$	−2	0	1	$\sqrt{2}$	$\sqrt{2}$	0	0	−2	−1	$-\sqrt{2}$	2	−1	0	1
H_g	4	0	4	0	−1	0	0	0	0	−4	1	0	−4	−1	0	1
H_u	4	0	−4	0	−1	0	0	0	0	−4	1	0	4	1	0	−1

Table 3.1.: Character table of the double cover of the full octahedral group O_h^d. The classes are represented by the following labels: I is the identity, R represents 90ř rotations, P is the parity transformation, and R' labels rotations perpendicular to R. See also [38].

Bosonic		Fermionic	
$SU(2)$	O^d	$SU(2)$	O^d
0	A_1	1/2	G_1
1	T_1	3/2	H
2	$E \oplus T_2$	5/2	$G_2 \oplus H$
3	$A_2 \oplus T_1 \oplus T_2$	7/2	$G_1 \oplus G_2 \oplus H$
4	$A_1 \oplus E \oplus T_1 \oplus T_2$	9/2	$G_1 \oplus 2H$
5	$E \oplus 2T_1 \oplus T_2$	11/2	$G_1 \oplus G_2 \oplus 2H$
6	$A_1 \oplus A_2 \oplus E \oplus T_1 \oplus 2T_2$		

Table 3.2.: $SU(2)$ irreducible representations subduced into O_h irreducible representations

which is a direct consequence of the tensor product [37]

$$\{\ell\} \otimes \left\{\frac{1}{2}\right\} = \left\{\ell + \frac{1}{2}\right\} \oplus \left\{\ell - \frac{1}{2}\right\}. \tag{3.12}$$

The subduction of $SU(2)$ irreducible representations up to $\ell = 6$ is shown in Tab. 3.2. The group theory explained in this section is relevant for efficient operator construction for hadron spectroscopy, especially for multi-hadronic operators, which are discussed in Sec. 3.4.

3.2. Isospin

In lattice QCD, it is a standard procedure to set the masses of the light quarks, i.e., the up and down quarks, to the same value $m_\ell = m_u = m_d$. This choice generates an additional symmetry, the isospin symmetry described by the $SU(2)$-group. Thus, the description of the isospin is analogous to the description of the spin in non-relativistic quantum mechanics discussed in multiple standard textbooks [40, 41]. Similar to the discussion of the spin in non-relativistic quantum mechanics, we define the isospin operators $\hat{I}_x$, $\hat{I}_y$, and $\hat{I}_z$ fulfilling the commutation relation

$$[\hat{I}_a, \hat{I}_b] = i\varepsilon_{abc}\hat{I}_c. \tag{3.13}$$

Additionally, we define the Casimir operator

$$\hat{I}^2 = \hat{I}_x^2 + \hat{I}_y^2 + \hat{I}_z^2. \tag{3.14}$$

Since $[\hat{I}^2, \hat{I}_z] = 0$, we know that eigenstates of $\hat{I}^2$ are also eigenstates of $\hat{I}_z$, and thus we can define isospin states $|j, m\rangle$ satisfying the following eigenvalue equations

$$\hat{I}^2 |jm\rangle = j(j+1) |jm\rangle, \tag{3.15a}$$

$$\hat{I}_z |jm\rangle = m |jm\rangle, \tag{3.15b}$$

where j denotes the total isospin of the state and $m = -j, -j+1, \ldots, j-1, j$. The states of the up and down quarks are isospin states and have the form $|u\rangle = \left|\frac{1}{2}, \frac{1}{2}\right\rangle$ and $|d\rangle = \left|\frac{1}{2}, -\frac{1}{2}\right\rangle$, respectively. For the anti-particle states, we obtain $|\bar{u}\rangle = \left|\frac{1}{2}, -\frac{1}{2}\right\rangle$ and

$\left|\bar{d}\right\rangle = -\left|\frac{1}{2}, \frac{1}{2}\right\rangle$.
The product of two isospin states $|j_1, m_1\rangle$ and $|j_2, m_2\rangle$ can be computed by

$$|J, M; j_1, j_2\rangle = \sum_{m_1=-j_1}^{j_1} \sum_{m_2=-j_2}^{j_2} |j_1 m_1; j_2 m_2\rangle \langle j_1 m_1, j_2 m_2 | J, M; j_1, j_2\rangle , \tag{3.16}$$

where $\langle j_1 m_1, j_2 m_2 | J, M; j_1, j_2\rangle$ denotes the Clebsch-Gordan coefficients.
For mesons consisting of an antiquark and a quark, we obtain an isosinglet of $I = 0$ state and an isotriplet of states with $I = 1$. For pseudo-scalar mesons, we obtain the isosinglet state

$$|\tilde{\eta}\rangle = |0, 0\rangle = -\frac{1}{\sqrt{2}}(|\bar{u}u\rangle + \left|\bar{d}d\right\rangle), \tag{3.17}$$

which is similar to the η-meson but without the strange quark contribution and, therefore, no physical state. The isotriplet pseudo-scalar states are the three types of pion defined by

$$\left|\pi^+\right\rangle = |1, 1\rangle = -\left|\bar{d}u\right\rangle , \tag{3.18a}$$

$$\left|\pi^0\right\rangle = |1, 0\rangle = \frac{1}{\sqrt{2}}(|\bar{u}u\rangle - \left|\bar{d}d\right\rangle), \tag{3.18b}$$

$$\left|\pi^-\right\rangle = |1, -1\rangle = |\bar{u}d\rangle . \tag{3.18c}$$

A color singlet of three quarks forms a baryon with a half-integer isospin. For isospin $j = \frac{1}{2}$ we obtain nucleons in the form of protons $|p\rangle$ and neutrons $|n\rangle$ with the quark contents

$$|p\rangle = \left|\frac{1}{2}, \frac{1}{2}\right\rangle = |uud\rangle \tag{3.19a}$$

$$|n\rangle = \left|\frac{1}{2}, -\frac{1}{2}\right\rangle = |udd\rangle . \tag{3.19b}$$

Additionally to the nucleon states, one can also find $j = \frac{3}{2}$ states labeled as Δ baryons ordered by their quark content and, thus, also by their electric charge in the following way:

$$\begin{aligned} \left|\Delta^{++}\right\rangle &= \left|\frac{3}{2}, \frac{3}{2}\right\rangle = |uuu\rangle , \qquad \left|\Delta^{+}\right\rangle = \left|\frac{3}{2}, \frac{1}{2}\right\rangle = |uud\rangle \\ \left|\Delta^{0}\right\rangle &= \left|\frac{3}{2}, -\frac{1}{2}\right\rangle = |udd\rangle , \qquad |\Delta^{-}\rangle = \left|\frac{3}{2}, -\frac{3}{2}\right\rangle = |ddd\rangle . \end{aligned} \tag{3.20}$$

Throughout the rest of this thesis, we will primarily consider pions and nucleons. One focus lies on the usage of multi-hadronic operators. Hence, in the following, we will compute different isospin projections that we will use throughout this thesis.
First, we consider two distinguishable pions guaranteed by giving both pions different momentum. Performing the calculation using Eq. 3.16 yields the following isospin $j = 1$ states,

$$|1, 1; \pi\pi\rangle = \frac{1}{\sqrt{2}} \left(\left|\pi^+\right\rangle \left|\pi^0\right\rangle - \left|\pi^0\right\rangle \left|\pi^+\right\rangle\right) , \tag{3.21a}$$

$$|1, 0, \pi\pi\rangle = \frac{1}{\sqrt{2}} \left(\left|\pi^+\right\rangle |\pi^-\rangle - |\pi^-\rangle \left|\pi^+\right\rangle\right) , \tag{3.21b}$$

$$|1, -1; \pi\pi\rangle = \frac{1}{\sqrt{2}} \left(\left|\pi^0\right\rangle |\pi^-\rangle - |\pi^-\rangle \left|\pi^0\right\rangle\right) , \tag{3.21c}$$

and the isospin $j = 0$ state

$$|0,0;\pi\pi\rangle = \frac{1}{\sqrt{3}}\left(\left|\pi^+\right\rangle|\pi^-\rangle + |\pi^-\rangle\left|\pi^+\right\rangle - \left|\pi^0\right\rangle\left|\pi^0\right\rangle\right). \tag{3.22}$$

There are also five $j = 2$ states that are irrelevant for the following. The $j = 1$ isospin projection is relevant for Ch. 7, considering multiple pion-pion states with different momenta and relevant. If the momenta of both pions vanish, then the pions can become indistinguishable, and we have $|\pi^i\rangle|\pi^j\rangle = |\pi^j\rangle|\pi^i\rangle$ for arbitrary $i, j = +, 0, -$. For this case, all $j = 1$ states disappear and the $j = 0$ state simplifies to

$$|0,0;\pi^r\pi^r\rangle = \frac{1}{\sqrt{3}}\left(2\left|\pi^+\right\rangle|\pi^-\rangle - \left|\pi^0\right\rangle\left|\pi^0\right\rangle\right), \tag{3.23}$$

where $\pi^r\pi^r$ indicates that both pions are at rest.
In Ch. 8, we investigate nucleon pion states in the isospin channel $j = \frac{1}{2}$. The projection can be computed similarly as the pion-pion states and yields

$$\left|\frac{1}{2},\frac{1}{2};N\pi\right\rangle = \sqrt{\frac{2}{3}}|n\rangle\left|\pi^+\right\rangle - \frac{1}{\sqrt{3}}|p\rangle\left|\pi^0\right\rangle, \tag{3.24a}$$

$$\left|\frac{1}{2},-\frac{1}{2};N\pi\right\rangle = -\sqrt{\frac{2}{3}}|p\rangle|\pi^-\rangle + \frac{1}{\sqrt{3}}|n\rangle\left|\pi^0\right\rangle. \tag{3.24b}$$

The product of pion and nucleon states also yields projections for $j = \frac{3}{2}$, which read

$$\left|\frac{3}{2},\frac{3}{2};N\pi\right\rangle = |p\rangle\left|\pi^+\right\rangle, \tag{3.25a}$$

$$\left|\frac{3}{2},\frac{1}{2};N\pi\right\rangle = \frac{1}{\sqrt{3}}|n\rangle\left|\pi^+\right\rangle + \sqrt{\frac{2}{3}}|p\rangle\left|\pi^0\right\rangle, \tag{3.25b}$$

$$\left|\frac{3}{2},-\frac{1}{2};N\pi\right\rangle = \frac{1}{\sqrt{3}}|p\rangle|\pi^-\rangle + \sqrt{\frac{2}{3}}|n\rangle\left|\pi^0\right\rangle, \tag{3.25c}$$

$$\left|\frac{3}{2},-\frac{3}{2};N\pi\right\rangle = |n\rangle|\pi^-\rangle. \tag{3.25d}$$

The $j = \frac{3}{2}$ projections are not relevant for the remainder of the thesis. However, since, for example, $\left|\frac{3}{2},\frac{1}{2};N\pi\right\rangle$ is orthogonal to $\left|\frac{1}{2},\frac{1}{2};N\pi\right\rangle$, and the ground state of $j = \frac{3}{2}$ is different from $j = \frac{1}{2}$, we can use $\left|\frac{3}{2},\frac{1}{2};N\pi\right\rangle$ to cross-check $\left|\frac{1}{2},\frac{1}{2};N\pi\right\rangle$.
In addition to the $N\pi$ states, we also consider the $N\pi\pi$ states in Ch. 8. Unlike in Ch. 7, both pions remain stationary in this context. The isospin $j = \frac{1}{2}$ projection is then given by

$$\left|\frac{1}{2},\frac{1}{2};N\pi\pi\right\rangle = \frac{2}{\sqrt{5}}|p\rangle\left|\pi^+\right\rangle|\pi^-\rangle - \frac{1}{\sqrt{5}}|p\rangle\left|\pi^0\right\rangle\left|\pi^0\right\rangle, \tag{3.26a}$$

$$\left|\frac{1}{2},-\frac{1}{2};N\pi\pi\right\rangle = \frac{2}{\sqrt{5}}|n\rangle\left|\pi^+\right\rangle|\pi^-\rangle - \frac{1}{\sqrt{5}}|n\rangle\left|\pi^0\right\rangle\left|\pi^0\right\rangle. \tag{3.26b}$$

Since we are in the isosymmetric limit, we can expect that the states with the same isospin j behave similarly. For this reason, we are only considering the states $\left|\frac{1}{2},\frac{1}{2}\right\rangle$, namely, $|p\rangle$, $\left|\frac{1}{2},\frac{1}{2};N\pi\right\rangle$, and $\left|\frac{1}{2},\frac{1}{2},N\pi\pi\right\rangle$, for all nucleon quantities throughout this thesis.

3.3. Wigner-Eckart Theorem

As established in previous sections, it is possible to construct a state that transforms according to G_{1g} with an isospin of $I = \frac{1}{2}$ and $I_z = \frac{1}{2}$, using various states that include a proton or several hadrons. In this section, our focus will once more be on the isospin characteristics while assuming the projection associated with the appropriate irreducible representation of the full octahedral group.
Using the bra-ket notation covered in the previous section, a correlation function can be defined as

$$C_{B\to A}(t) = \langle A|B\rangle. \tag{3.27}$$

For the specific case of the correlation function $C_{N\pi\to N\pi}$, it is represented by

$$C_{N\pi\to N\pi}(t) = \langle N\pi|N\pi\rangle = \frac{2}{3}\langle n\pi^+|n\pi^+\rangle - \frac{\sqrt{2}}{3}\langle p\pi^0|n\pi^+\rangle - \frac{\sqrt{2}}{3}\langle n\pi^+|p\pi^0\rangle + \frac{1}{3}\langle p\pi^0|p\pi^0\rangle, \tag{3.28}$$

assuming that $|N\pi\rangle$ has isospin $I = \frac{1}{2}$ and $I_z = \frac{1}{2}$. Here, the notation $|n\pi^+\rangle = |n\rangle\,|\pi^+\rangle$ is used. To evaluate this correlation function, it is necessary to calculate each term. Nevertheless, using the Wigner-Eckart theorem, we can derive relations among some of these correlation functions, which will be elaborated upon further.
The Wigner-Eckart theorem states that for any spherical tensor $T^{(k)}$ with rank k, it holds that

$$\langle jm|T^{(k)}_q|j'm'\rangle = \langle j'm'kq|jm\rangle\langle j||T^{(k)}||j'\rangle, \tag{3.29}$$

with the isospin eigenstates $|jm\rangle$, the $SU(2)$ Clebsch-Gordan coefficients $\langle j'm'kq|jm\rangle$, and the reduced matrix element $\langle j||T^{(k)}||j'\rangle$ [42]. We use two different spherical tensors for finding the relations, the first one is the scattering operator S of rank 0 with the matrix elements

$$\langle jm|S|j'm'\rangle = \delta_{mm'}\delta_{jj'}S^j. \tag{3.30}$$

Also useful is the rank 1 pseudo-scalar operator $\mathcal{P}$ with the entries

$$\mathcal{P}^+(x) = -\bar{d}(x)\gamma^5 u(x), \tag{3.31}$$

$$\mathcal{P}^0(x) = \frac{1}{\sqrt{2}}\left(\bar{u}(x)\gamma^5 u(x) - \bar{d}(x)\gamma^5 d(x)\right), \tag{3.32}$$

$$\mathcal{P}^-(x) = \bar{u}(x)\gamma^5 d(x). \tag{3.33}$$

We can use both tensors to deduce the following relations:

$$\langle p\pi^0|p\rangle = -\frac{1}{\sqrt{2}}\langle n\pi^+|p\rangle \tag{3.34a}$$

$$\langle p\pi^0|p\pi^0\rangle = \frac{1}{\sqrt{2}}\langle p\pi^0|n\pi^+\rangle + \langle n\pi^+|n\pi^+\rangle \tag{3.34b}$$

$$\langle p\pi^0\pi^0|p\rangle = -\langle p\pi^+\pi^-|p\rangle \tag{3.34c}$$

$$\langle p\pi^0\pi^0|p\pi^0\pi^0\rangle = \langle p\pi^+\pi^-|p\pi^0\pi^0\rangle + 2\langle p\pi^+\pi^-|p\pi^+\pi^-\rangle \tag{3.34d}$$

$$\langle p\pi^+\pi^-|p\pi^0\rangle = \sqrt{2}\langle p\pi^0\pi^0|n\pi^+\rangle \tag{3.34e}$$

$$\langle p\pi^0\pi^0|p\pi^0\rangle = \frac{1}{\sqrt{2}}\langle p\pi^0\pi^0|n\pi^+\rangle + \sqrt{2}\langle p\pi^+\pi^-|n\pi^+\rangle \tag{3.34f}$$

Moreover, it also true that $\langle A|B\rangle = \langle B|A\rangle^*$. The correlation function from Eq. 3.28 then can be rewrite as

$$\langle N\pi|N\pi\rangle = \langle n\pi^+|\ n\pi^+\rangle - \frac{1}{\sqrt{2}}\langle p\pi^0|n\pi^+\rangle. \tag{3.35}$$

A similar simplification is possible for other correlation functions, which significantly reduces the computational cost. Nonetheless, this relation is applicable not only to cost reduction but also serves a valuable role in verifying the automatically generated Wick contractions, as presented in [43].

3.4. Operator Construction

In Sec. 2.10, we have already discussed the importance of the choice of interpolating operators. In this section, we will define the operators used throughout this thesis.
First, we define the relevant single-hadron operators, starting with the pion. The pion is a pseudo-scalar meson, meaning it is invariant under rotations and has negative parity. A general meson interpolating operator is

$$\mathcal{O}_M(x) = \bar{\psi}_i(x)\Gamma_M\psi_j(x), \tag{3.36}$$

where ψ_i denotes the fermions with flavor i and Γ a general γ-structure. We also imply an implicit summation over color and spin indices. To reconstruct the pseudo-scalar character of the pion, we have to find a γ-structure fulfilling

$$S[R]^\dagger\Gamma_\pi S[R] = \Gamma_\pi, \text{ for an arbitrary } R, \tag{3.37a}$$

$$\gamma_t\Gamma_\pi\gamma_t = -\Gamma_\pi, \tag{3.37b}$$

where $S[R]$ denotes the transformation behavior of a spinor under rotation R, i.e., $\psi(\boldsymbol{x},t) \xrightarrow{R} S[R]\psi(R^T\boldsymbol{x},t)$. In Sec. 3.1, we have already shown that it is sufficient to only consider 90° rotations around the x- and z-axis, since repeated products of both can generate every other rotation. Eq. 3.37b is a consequence of the negative parity of the pion, for which we use the spinor transformation introduced in Eq. 3.10b. One can show that both

$$\Gamma_\pi = \gamma_5 \quad \text{and} \quad \Gamma_\pi = \gamma_t\gamma_5 \tag{3.38}$$

fulfill the conditions of Eq. 3.37. However, for the rest of this thesis, we will always use

$$\mathcal{O}_\pi(x) = \bar{\psi}_i(x)\gamma_5\psi_j(x). \tag{3.39}$$

Taking the isospin into account, we get the isotriplet of interpolating operators:

$$\mathcal{O}_{\pi^+}(x) = -\bar{d}(x)\gamma_5 u(x), \tag{3.40a}$$

$$\mathcal{O}_{\pi^0}(x) = \frac{1}{\sqrt{2}}\left(\bar{u}(x)\gamma_5 u(x) - \bar{d}(x)\gamma_5 d(x)\right), \tag{3.40b}$$

$$\mathcal{O}_{\pi^-}(x) = \bar{u}(x)\gamma_5 d(x). \tag{3.40c}$$

In Ch. 7, we will additionally consider the ρ-meson, a vector meson. The irreducible representation of a vector is three-dimensional. Therefore we define a set of three γ-structures, $\{\Gamma_{\rho_x}, \Gamma_{\rho_y}, \Gamma_{\rho_z}\}$, transforming as

$$S[R]^\dagger\Gamma_{\rho_i}S[R] = \Gamma_{\rho_{R\cdot i}}, \tag{3.41}$$

where $R \cdot i$ denotes the rotation of the unit vector in i-th direction. For example, in the case of $R = R_z$ and Γ_{ρ_x} we obtain

$$S[R_z]^\dagger \Gamma_{\rho_x} S[R_z] = \Gamma_{\rho_y}. \tag{3.42}$$

Furthermore, we require that Γ_{ρ_i} completes the parity transformation defined in Eq. 3.37b. We can show that $\Gamma_{\rho_i} = \gamma_i$ and $\Gamma_{\rho_i} = \gamma_t\gamma_i$ satisfy the vector transformation. However, in the following, we only consider

$$\mathcal{O}_{\rho_k}(x) = \bar{\psi}_i(x)\gamma_k\psi_j(x), \quad \text{with } k = x, y, z, \tag{3.43}$$

with additional isospin projection similar to the pion case in Eq. 3.40.
The quark and anti-quark pairs in mesons are automatically guaranteed to be a color-singlet state if both quarks have the same color index, which we have already implied for the interpolator operator definitions. In contrast, a set of three quarks forming a baryon is not automatically color-singlet. A state is a color singlet if it is colorless. There are two options to form a colorless state. First, a combination of anticolor and color (see mesons) or the sum of red, blue, and green. The second one can be constructed by the usage of the anti-symmetrical Levi-Civita symbol, yielding

$$\mathcal{O}_{b,\alpha\beta\gamma}(x) = \varepsilon_{abc}\psi^{f_1}_{a,\alpha}(x)\psi^{f_2}_{b,\beta}(x)\psi^{f_3}_{c,\gamma}(x), \tag{3.44}$$

where the spin (α, β, γ) and flavor (f_1, f_2, f_3) are chosen to reflect the wanted spin and isospin structure, respectively. Furthermore, for the color indices, we imply the Einstein sum convention. To incorporate additionally the spin structure, we define the baryon operator, following [6], to be

$$\mathcal{O}_{b,\alpha}(x) = \varepsilon_{abc}(P^\pm\Gamma^A\psi^{f_1}_a(x))_\alpha \left[\psi^{f_2}_b(x)^T\Gamma^B\psi^{f_3}_c(x)\right], \tag{3.45}$$

with implicit matrix/vector multiplication for the spin components. Γ^A and Γ^B are chosen so that the operator transforms in the wanted irreducible representation, e.g., G_{1g} for nucleons. One can show that operators with

$$(\Gamma^A, \Gamma^B) = (\mathbb{1}, C\gamma_5), (\gamma_5, C), \text{and } (\mathbb{1}, i\gamma_t C\gamma_5) \tag{3.46}$$

transform in the G_1 irrep, where $C = i\gamma_y\gamma_t$ denotes the charge conjugation matrix. The parity of the operator in Eq. 3.45 is determined by the projection matrix $P^\pm = \frac{1}{2}(\mathbb{1} \pm \gamma_t)$. Throughout this thesis we will use the standard γ-structure $(\mathbb{1}, C\gamma_5)$ yielding the nucleon operators

$$\mathcal{O}_{p^\pm}(x)_\alpha = \varepsilon_{abc}(P^\pm u_a(x))_\alpha \left[u_b(x)^T C\gamma_5 d_c(x)\right], \tag{3.47a}$$

$$\mathcal{O}_{n^\pm}(x)_\alpha = \varepsilon_{abc}(P^\pm d_a(x))_\alpha \left[d_b(x)^T C\gamma_5 u_c(x)\right], \tag{3.47b}$$

where $\pm$ denotes the parity of the state. The operator $O_{p^\pm,\alpha}$ is associated with the isospin state $(I = \frac{1}{2}, I_z = \frac{1}{2})$, representing the proton under positive parity conditions. Similarly, with analogous reasoning, $O_{n^\pm,\alpha}$ corresponds to the isospin state $(I = \frac{1}{2}, I_z = -\frac{1}{2})$, which identifies the neutron within the positive parity domain. Note that the diquark structure

within the square brackets of Eq. 3.47, transforms trivially under parity and rotation structure, and therefore, the whole operator transforms like a spinor under rotations, i.e.,

$$\mathcal{O}_{N^\pm}(x)_\alpha \xrightarrow{R} \mathcal{O}'_{N^\pm}(x')_\alpha = \sum_\beta S[R]_{\alpha\beta}\mathcal{O}_{N^\pm}(R^T\boldsymbol{x},t)_\beta, \tag{3.48}$$

where $O_{N^\pm}$ denotes a general nucleon operator and can be either $O_{p^\pm}$ or $O_{n^\pm}$. Due to the explicit parity transformation, the operators already have a definite parity and transform like

$$\mathcal{O}_{N^\pm}(x)_\alpha \xrightarrow{P} \mathcal{O}'_{N^\pm}(x')_\alpha = \pm\mathcal{O}_{N^\pm}(-\boldsymbol{x},t)_\alpha. \tag{3.49}$$

Until now, we have considered local operators $O(x)$, yet in most cases, we are interested in operators with a definite spatial momentum $\boldsymbol{p}$. Such an operator is constructed using the discrete Fourier transformation (cf. Eq. 2.95), yielding

$$\mathcal{O}(\boldsymbol{p},t) = \frac{1}{\sqrt{\Lambda_3}}\sum_{\boldsymbol{x}} e^{-i\boldsymbol{x}\cdot\boldsymbol{p}}\mathcal{O}(\boldsymbol{x},t), \tag{3.50}$$

where Λ_3 denotes the number of spatial lattice points. The momenta $\boldsymbol{p}$ are discretized and have components of the form $p_i = \frac{2\pi}{L_i}k_i$, with $-L_i/2 < k_i \leq L_i/2$ and L_i the number of lattice points in the i-th direction.
Next, we move on to multi-hadronic operators. First, consider the two-pion operators relevant for Ch. 7. There, the goal is to find two-pion states with the same transformational behavior as the ρ -meson, i.e., in the lattice irreducible representation T_{1u} and with isospin $I = 1$. Since pions are pseudo-scalar particles, a finite momentum is needed to create a vector-like structure. One can show that the pion operator with definite momentum $\boldsymbol{p}$ transforms under rotations R and parity transformations P like

$$\mathcal{O}_\pi(\boldsymbol{p},t) \xrightarrow{R} \mathcal{O}'(\boldsymbol{p}',t) = \mathcal{O}(R\boldsymbol{p},t), \tag{3.51a}$$

$$\mathcal{O}_\pi(\boldsymbol{p},t) \xrightarrow{R} \mathcal{O}'(\boldsymbol{p}',t) = -\mathcal{O}(-\boldsymbol{p},t). \tag{3.51b}$$

Combining two finite momentum pion operators with back-to-back momentum yields an operator with zero total momentum and a non-trivial transformational behavior under rotation, which reads

$$\mathcal{O}_{\pi_1\pi_2}(t|\boldsymbol{p}) = \mathcal{O}_{\pi_1}(\boldsymbol{p},t)\mathcal{O}_{\pi_2}(-\boldsymbol{p},t), \tag{3.52}$$

where π_1 and π_2 are operators of the isotriplet of pions, i.e., $\pi^\pm$ or π^0. The two-pion operator $O_{\pi_1\pi_2}$ has not yet been projected on specific irreducible representations of O_h. For the projection, we consider the set of operators with all momenta from the orbit of an initial signature momentum. The orbit of an vector $\boldsymbol{q} \in \mathbb{R}^3$ in the group G is defined as

$$G \cdot \boldsymbol{q} = \{g \cdot \boldsymbol{q} | g \in G\}. \tag{3.53}$$

Each orbit can be labeled with a signature momentum defined as a positive ordered vector $\boldsymbol{q} = \frac{2\pi}{L}(n,m,\ell)$, with $\ell \geq m \geq n \geq 0$. Given that the size of the lattice only determines the prefactor $2\pi/L$, we will omit it when referring to the signature momenta henceforth. Note that the squared Euclidean norm of these integer signature momenta is also an integer.

The projection of the operator defined in Eq. 3.52 onto the irreducible representation Λ is then given by

$$\mathcal{O}_{\pi_1\pi_2,(\Lambda,j)}(t;\boldsymbol{q}) = \sum_{\boldsymbol{q}_i \in O_h^d \cdot \boldsymbol{q}} C_i^{(\Lambda,j)} \mathcal{O}_{\pi_1\pi_2}(t;\boldsymbol{q}_i), \tag{3.54}$$

where the $C_i^{(\Lambda,j)}$ can be computed using the group theory techniques described in Sec. 3.1 and j denotes the indexing within irreducible representations Λ, where $0 \leq j < \dim(\Lambda)$. Furthermore, for momenta $\boldsymbol{q}$ with $||\boldsymbol{q}||_2^2 < 9$, which are the only relevant momenta throughout this thesis, we find only at most one signature momentum $\boldsymbol{q}_N$ fulfilling $||\boldsymbol{q}_N||_2^2 = N$ for every $N < 9$. In the following, we will label the corresponding signature momenta by $\boldsymbol{N}$, for example, we label the signature momentum $(0,0,1)$ by $\mathbf{1}$. For the signature momentum $\mathbf{1}$ the relevant T_{1u} operator has the form

$$\mathcal{O}_{\pi_1\pi_2,T_{1u}}(t;\mathbf{1})_j = \mathcal{O}_{\pi_1}(p\hat{e}_j,t)\mathcal{O}_{\pi_2}(-p\hat{e}_j,t) - \mathcal{O}_{\pi_1}(-p\hat{e}_j,t)\mathcal{O}_{\pi_2}(p\hat{e}_j,t), \tag{3.55}$$

with $p = \frac{2\pi}{L}$ and $\hat{e}_j$ the unit vector in j-th direction. In Ch. 7, we consider the signatures $\mathbf{1}, \mathbf{2}, \mathbf{3}, \mathbf{4}, \mathbf{5}, \mathbf{6}$ and $\mathbf{8}$.

We can use the procedure to construct nucleon-pion and nucleon-pion-pion operators relevant for Ch. 8.

To construct a nucleon-pion operator with positive parity, a back-to-back momentum configuration must be applied to the nucleon and pion. This requirement arises from the inherent negative parity of the pion. We can define the nucleon-pion operator without any G_1 projection, reading

$$\mathcal{O}_{(N\pi)^\pm}(t;\boldsymbol{q})_\alpha = \mathcal{O}_{N^+}(\boldsymbol{q},t)_\alpha \mathcal{O}_\pi(-\boldsymbol{q},t) \mp \mathcal{O}_{N^+}(-\boldsymbol{q},t)_\alpha \mathcal{O}_\pi(\boldsymbol{q},t), \tag{3.56}$$

where the sign in the superscript of $(N\pi)^\pm$ indicate the parity of the state. The projection onto the positive parity O_h^d irreducible representation G_{1g} for momentum signature $\mathbf{1}$ is calculated using group theory yielding

$$\mathcal{O}_{N\pi,G_{1g}}(t,\mathbf{1})_\alpha = \Sigma^x_{\alpha\beta}\mathcal{O}_{(N\pi)^+}(t;p\hat{e}_x)_\beta + \Sigma^y_{\alpha\beta}\mathcal{O}_{(N\pi)^+}(t;p\hat{e}_y)_\beta + \Sigma^z_{\alpha\beta}\mathcal{O}_{(N\pi)^+}(t;p\hat{e}_z)_\beta, \tag{3.57}$$

with an implicit sum over β and $\Sigma^j = \mathbb{1} \otimes \sigma^j$ with σ^j denoting the Pauli matrices. The operator is identical to the one used in [44–46]. The parity of two pions at rest is positive, and therefore, we can construct a nucleon-pion-pion operator with all particles at rest, which naturally transforms in the G_{1g} irreducible representation and can be defined as

$$O_{N\pi\pi,G_{1g}}(t;\mathbf{0})_\alpha = \mathcal{O}_{N^+}(\mathbf{0},t)_\alpha \mathcal{O}_\pi(\mathbf{0},t)\mathcal{O}_\pi(\mathbf{0},t). \tag{3.58}$$

Within the negative parity sector, it is feasible to formulate a nucleon-pion operator without back-to-back momentum configuration, i.e., with $\mathbf{0}$ momentum signature. Following [47], we define

$$O_{N\pi,G_{1u}}(t;\mathbf{0})_\alpha = \gamma_5 \mathcal{O}_{N^+}(\mathbf{0},t)_\alpha \mathcal{O}_\pi(\mathbf{0},t). \tag{3.59}$$

An analogous negative parity operator to the one described in Eq. 3.57 can be specified by modifying the projection from G_{1g} to G_{1u}. This provides

$$\mathcal{O}_{N\pi,G_{1u}}(t,\mathbf{1})_\alpha = \mathcal{O}_{(N\pi)^-}(t;p\hat{e}_x) + \mathcal{O}_{(N\pi)^-}(t;p\hat{e}_y) + \mathcal{O}_{(N\pi)^-}(t;p\hat{e}_z), \tag{3.60}$$

which is similar to the operator described in [44]. In the negative parity sector, nucleon-pion-pion states are excluded from our considerations. Consequently, we have established the relevant single- and multi-hadronic operators containing pions and nucleons utilized in this thesis.

4. Neutrino Physics

In 1930, Wolfgang Pauli proposed the existence of neutrinos to account for the apparent violation of energy conservation observed in radioactive β-decays. During that period, β-decay was hypothesized to involve the transformation of a neutron into a marginally lighter proton accompanied by the emission of an electron. Nevertheless, the principles of energy and momentum conservation dictate that electrons should possess a fixed energy, whereas experiments revealed that electrons appear with a spectrum of energies. Pauli suggested the existence of an (nearly) undetectable neutral particle, the neutrino, to resolve this discrepancy. With the inclusion of the neutrino, β-decay is represented by

$$n \to p + e^- + \bar{\nu}_e, \tag{4.1}$$

where an electron-flavored antineutrino is created. In 1956, Clyde Cowan and Frederick Reines provided experimental confirmation of Pauli's hypothesis by achieving the first detection of neutrinos. They utilized neutrinos generated from the β-decays of fission products within a nuclear reactor. The detection apparatus comprised two water tanks, which served as a sufficient target for the rare interactions of antineutrinos with protons in water molecules, as described by

$$\bar{\nu}_e + p \to n + e^+. \tag{4.2}$$

The positrons formed during these interactions annihilated with electrons, resulting in the emission of two gamma photons, which were subsequently detected.
Unlike other fermions in the standard model, neutrinos are consistently detected as left-handed, i.e., $\gamma_5 \psi_L = -\psi_L$[1]. This characteristic poses challenges when attempting to assign mass to neutrinos through interactions with the Higgs field, using the Yukawa coupling. Consequently, since experimental data only offer an upper limit for neutrino mass, neutrinos were traditionally considered massless.
This paradigm of massless neutrinos got challenged by the detection of solar neutrinos, which indicated a discrepancy between the predicted and observed neutrino flux originating from the Sun. The Sun emits electron-type neutrinos. However, measurements taken on Earth showed fewer electron-neutrinos than anticipated. In 1957, Bruno Pontecorvo proposed a resolution to this solar neutrino issue. His idea postulated that the electron-neutrinos transform their flavor during their journey from the Sun to Earth. This suggests two characteristics of neutrinos:

1. The eigentime of neutrinos evolves, suggesting that they must travel slower than the speed of light and, therefore, must have mass.

2. The neutrinos' mass eigenstates must differ from their flavor eigenstates.

[1] Anti-neutrinos are consistently detected as right-handed

Evidence supporting neutrino oscillation was experimentally demonstrated by the Super-Kamiokande and Sudbury Neutrino Observatories, and this discovery was honored with the Nobel Prize in Physics in 2015 [48, 49]. For a comprehensive introduction to the historical context of neutrino physics, see [50, 51].

4.1. Neutrino Oscillation

As previously stated, neutrinos possess distinct mass and flavor eigenstates. The flavor eigenstates can be represented as a linear combination of the mass eigenstates via

$$|\nu_\alpha\rangle = \sum_i U^*_{\alpha i} |\nu_i\rangle \,, \tag{4.3}$$

where $\alpha = e, \mu, \tau$ denotes the flavor index and $i = 1, 2, 3$ the mass index. Here, $U_{\alpha i}$ denotes the elements of the Pontecorvo-Maki-Nakagawa-Sakata (PMNS) matrix. The PMNS matrix is generally parameterized as follows [52]:

$$U = \begin{pmatrix} 1 & 0 & 0 \\ 0 & c_{23} & s_{23} \\ 0 & -s_{23} & c_{23} \end{pmatrix} \begin{pmatrix} c_{13} & 0 & s_{13}e^{-i\delta_{CP}} \\ 0 & 1 & 0 \\ -s_{13}e^{i\delta_{CP}} & 0 & c_{13} \end{pmatrix} \begin{pmatrix} c_{12} & s_{12} & 0 \\ -s_{12} & c_{12} & 0 \\ 0 & 0 & 1 \end{pmatrix} \begin{pmatrix} e^{i\eta_1} & 0 & 0 \\ 0 & e^{i\eta_2} & 0 \\ 0 & 0 & 1 \end{pmatrix} \tag{4.4}$$

Here, $c_{ij} = \cos(\theta_{ij})$ and $s_{ij} = \sin(\theta_{ij})$, and δ_{CP} represents the charge-parity (CP) violation phase. The phases η_1, η_2 provide additional degrees of freedom when neutrinos are considered Majorana fermions. However, in this study, we assume that neutrinos are Dirac fermions, thus setting $\eta_1 = \eta_2 = 0$. Significant experimental efforts are underway to accurately measure the mixing angles θ_{ij} and the CP phase δ_{CP} by investigating neutrino oscillations, which will be discussed below. The determination of Majorana phases remains speculative and could potentially be achieved by observation of neutrino-less double beta decay [53], a phenomenon not yet observed.
The evolution of the mass eigenstates $|\nu_i\rangle$ can be represented using plane waves, yielding

$$|\nu_i(t)\rangle = e^{-iE_i t} |\nu_i(0)\rangle \,, \tag{4.5}$$

where $E_i = \sqrt{p_i^2 + m_i^2}$ represents the energy, m_i denotes the mass and p_i is the momentum of the energy eigenstate ν_i. Given their small mass, neutrinos are effectively ultra-relativistic. Thus, $p_i \approx p_j \equiv p \approx E$, allowing us to approximate:

$$E_i = \sqrt{p_i^2 + m_i^2} \approx p + \frac{m_i^2}{2E}. \tag{4.6}$$

Moreover, given the ultra-relativistic characteristics of neutrinos, they move near the light cone, resulting in $t \approx L$, where L represents the distance covered.
The flavor state $|\nu_\alpha\rangle$ described in Eq. 4.3 evolves according to the equation:

$$|\nu_\alpha(t)\rangle = \sum_i U^*_{\alpha i} e^{iE_i t} |\nu_\alpha(0)\rangle \,, \tag{4.7}$$

which demonstrates that the flavor state composition changes over time. After traveling a distance L, the probability that we observe the neutrino with flavor β is expressed as

$$P_{\alpha\beta} = |\langle \nu_\beta | \nu_\alpha(t) \rangle|^2 = \Big| \sum_{i,j} U^*_{\alpha i} U_{\beta j} e^{iE_i t} \Big|^2, \tag{4.8}$$

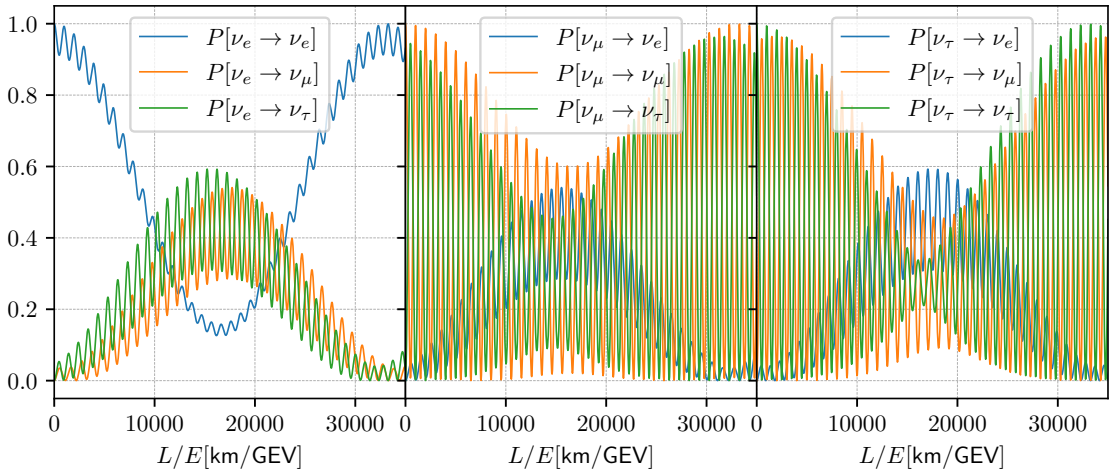

Figure 4.1.: The probability of detecting the ν_β flavor state as a function of L/E in [km/GeV], starting from an initial ν_α flavor state, is examined. The initial flavor states, arranged from left to right, are electron, muon, and tau neutrinos.

utilizing the orthogonality condition of the neutrino mass states, $\langle \nu_j | \nu_i \rangle = \delta_{ij}$. A more convenient written form of this equation is [52]

$$\begin{aligned} P_{\alpha\beta} = \delta_{\alpha\beta} &- 4 \sum_{i<j} \mathrm{Re}[U_{\alpha i} U^*_{\beta i} U^*_{\alpha j} U_{\beta j}] \sin^2 X_{ij} \\ &+ 2 \sum_{i<j} \mathrm{Im}[U_{\alpha i} U^*_{\beta i} U^*_{\alpha j} U_{\beta j}] \sin 2X_{ij}, \end{aligned} \tag{4.9}$$

where

$$X_{ij} = \frac{(m_i^2 - m_j^2)L}{4E} = 1.267 \frac{\Delta m^2_{ij}}{\mathrm{eV}^2} \frac{L/E}{\mathrm{km/GeV}}, \tag{4.10}$$

and $\Delta m^2_{ij} \equiv m_i^2 - m_j^2$ is introduced.
Using the most recent estimates for U as given in [54], it is found that $\mathrm{Re}[U_{\alpha i} U^*_{\beta i} U^*_{\alpha j} U_{\beta j}] \gg \mathrm{Im}[U_{\alpha i} U^*_{\beta i} U^*_{\alpha j} U_{\beta j}]$, which means that the probability, at leading order, is an even function. As a consequence, measuring $P_{\alpha\beta}$ is only sensitive to the absolute values of the mass-squared differences $|\Delta m^2_{ij}|$.
The assumptions that give rise to Eq. 4.9 hold only in vacuum. It was discovered that when neutrinos travel through matter, their oscillatory dynamics is different from the vacuum, an effect known as the Mikheyev-Smirnov-Wolfenstein effect [55–57]. This effect enabled for the accurate determination of the sign of Δm^2_{21} due to matter effects inside the Sun. However, the sign of Δm^2_{31} and Δm^2_{32} remains to be determined, but it is established that $|\Delta m^2_{3\ell}| > |\Delta m^2_{21}|$, which results in two potential mass hierarchies:

- the Normal Hierarchy, $m_3 > m_2 > m_1$
- the Inverted Hierarchy, $m_2 > m_1 > m_3$

Fig. 4.1 shows the evolution of the probability of Eq. 4.9 for a initial pure neutrino of flavor $\alpha = e, \mu, \tau$. As parameters, the central values of the IC24 with Super-Kamiokande atmospheric data fit of NuFit 6.0 [54] are used.

4.2. DUNE/LBNF Experiment

This section presents the DUNE/LBNF experiment as an example of neutrino detection efforts. The DUNE/LBNF is a neutrino experiment that is presently being built. Upon completion, neutrinos will be generated at Fermilab within the Long Baseline Neutrino Facility (LBNF) and directed toward a neutrino detector located 1300 km away at the Sanford Underground Research Facility. The primary objectives of this experiment include obtaining accurate measurements of the parameters that control the oscillation processes $\nu_\mu \to \nu_e$ and $\bar{\nu}_\mu \to \bar{\nu}_e$, as cited in [58]. Specifically, consisting of:

- measuring δ_{CP} — should $\delta_{CP} \neq 0, \pi$, this would offer the first indications of CP violation within the leptonic sector and could thus provide an explanation for the matter-antimatter asymmetry observed in the universe,
- determining the neutrino mass hierarchy by identifying the sign of Δm^2_{31},
- conducting precision tests of the three-flavor neutrino oscillation model.

Furthermore, the DUNE experiment aims to explore signs of proton decay, which may provide valuable information regarding the Grand Unification of Fundamental Forces. In addition, if neutrinos of a core-collapse supernova event occurring within the boundaries of our galaxy reach the Earth during the operational period of DUNE, it might enable observation and quantitative analysis of its electron neutrino (ν_e) flux.
A short description of the experiment is that within the Long-Baseline Neutrino Facility (LBNF), a beam composed of muon-flavored neutrinos and antineutrinos is generated. Still located at Fermilab, this beam undergoes analysis using a magnetized neutrino detector. This detector yields detailed information regarding the energy spectrum and composition of the neutrino beam at its point of origin. Subsequently, the neutrino beam travels approximately 1300 kilometers beneath the Earth's surface, ultimately reaching the Sanford Underground Research Facility. At this location, the primary neutrino detector, which features state-of-the-art liquid-argon time projection chamber (LArTPC) technology, is installed. Readers interested in more detailed technical information are referred to [58, 59]. Fig. 4.2 provides an illustration of this composition.
Fig. 4.3 demonstrates the process by which a concentrated neutrino beam is produced at LBNF. Initially, the main injector, which functions as a particle accelerator, delivers the primary proton beam for LBNF. This proton beam subsequently collides with a target, producing scattered particles such as neutrons, pions, kaons, and others. The charged pions and kaons are then directed using a device known as a magnetic horn to a focused beam. Due to the inherent instability of pions and kaons, they eventually decay into charged leptons and neutrinos. Because of the conservation of momentum, the beam remains focused as it strikes a concrete block, which absorbs the charged leptons, while allowing the neutrinos to pass through with minimal disturbance.
Providing a detailed description of neutrino detectors' operations exceeds the scope of this thesis. Nonetheless, the core operation of the far detector can be summarized as follows.

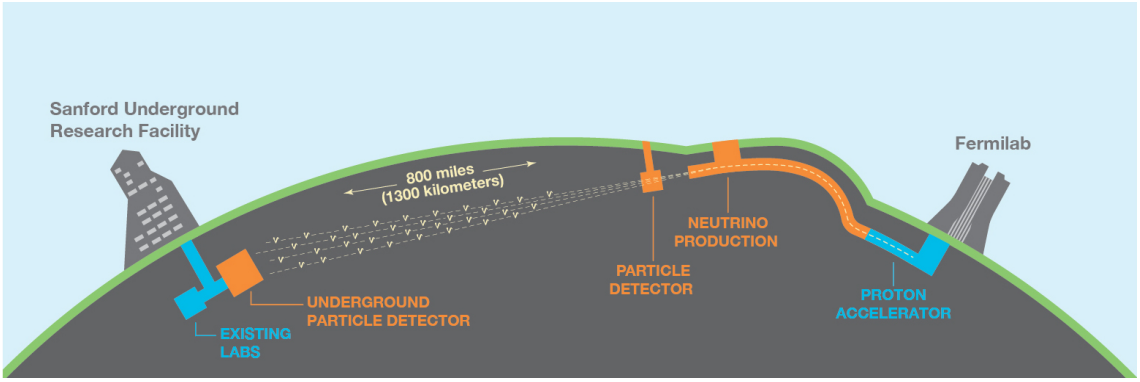

Figure 4.2.: Sketch of the Deep Underground Neutrino Experiment. The source of the picture is https://www.dunescience.org/

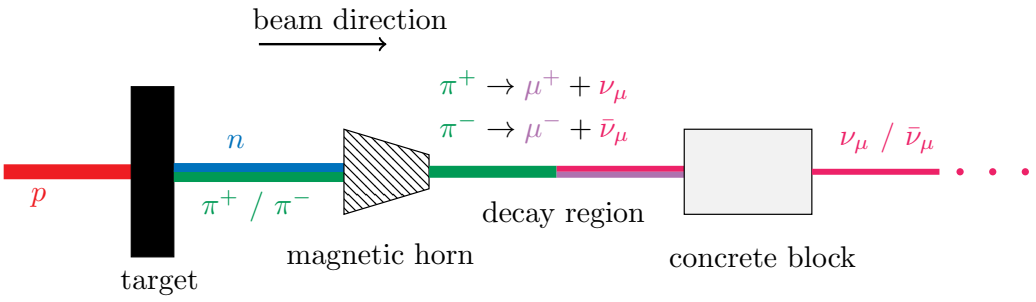

Figure 4.3.: Sketch of the creation of muon-flavored (anti)neutrinos at LBNF. The sketch shows the creations through the decay of pions, which is only one of many decays leading to neutrinos.

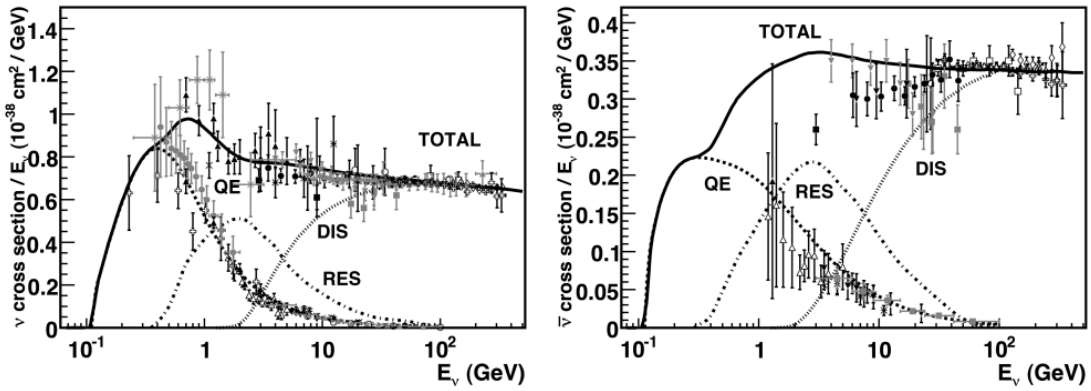

Figure 4.4.: The plots on the left and right depict the cross sections of neutrinos and antineutrinos as they relate to energy. These illustrations highlight contributions from fundamental processes that include quasielastic scattering, resonance production, and deep-inelastic scattering. The illustration is sourced from [63].

The detector comprises four LArTPC modules with a combined volume of 70 kilotons of liquid argon. Within these LArTPC modules, an electric field is applied. If a neutrino interacts with an argon nucleus, charged particles are produced. These particles ionize the surrounding argon and generate scintillation light. The electric field causes ionization electrons to drift toward the wire planes, where they are collected and recorded. The collected electron data, along with scintillation light information, facilitates the precise three-dimensional reconstruction of the event.

4.3. Neutrino-Nucleus Scattering

For optimal scientific outcomes, experiments rely on a priori knowledge of potential scattering events. Theoretical understanding can provide such insights across a broad spectrum of energy regimes, each presenting its unique challenges and, therefore, often addressed as separate issues. The subsequent section will explore how lattice QCD can offer valuable insights for the modeling of Neutrino-Nucleus Scattering. This summary is fundamentally based on the insights offered by [60].

Typically, the nuclei employed in neutrino detection are of medium to large size, such as carbon, oxygen, or, specifically for DUNE, argon. Presently, direct lattice QCD calculations for neutrino-nucleus scattering are not feasible. Nevertheless, these scattering processes can be approached using effective field theories, for which lattice QCD offers non-perturbative, first-principle calculations of nucleon inputs [60–62]. Consequently, the following discussion will emphasize neutrino-nucleon scattering, which is currently feasible to calculate on the lattice.

Fig. 4.4 depicts the cross sections for neutrinos and antineutrinos, demonstrating the contributions from distinct fundamental processes at specific neutrino energy levels. Generally, we can recognize three main processes: quasi-elastic scattering, resonance production, and deep-inelastic scattering.

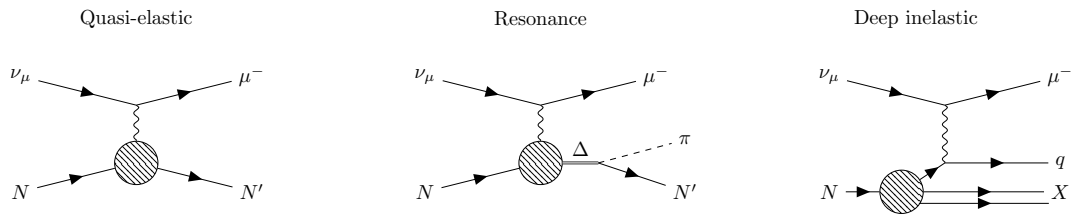

Figure 4.5.: Nucleon level Feynman diagrams of the relevant regimes, from left to right: quasi-elastic, resonance and deep-inelastic scattering. The blob represents non-perturbative QCD contributions.

At the nucleon scale, quasi-elastic scattering involves, for example, the incident neutrino converting the targeted nucleon into its isospin partner while emitting a charged lepton,

$$\bar{\nu}_\ell\, p \to \ell^+ n, \quad \text{and} \quad \nu_\ell\, n \to \ell^- p. \tag{4.11}$$

In the leading order of electroweak interactions, the process involves the exchange of a W boson, as shown in the diagram on the left diagram of Fig. 4.5. Since these scattering events are relevant to low nucleon energies, the strong interaction is non-perturbative, thus the QCD interaction indicated by the blob in the diagram cannot be computed using standard perturbation theory. Lattice QCD is thus employed in such cases. The interaction of a nucleon with the W boson can be characterized by the matrix element of the axial vector current A^a_μ, represented as

$$\langle N'(\boldsymbol{p}+\boldsymbol{q})|A^a_\mu(\boldsymbol{q})|N(\boldsymbol{p})\rangle = \bar{u}(\boldsymbol{p}+\boldsymbol{q})\left[G_A(Q^2)\gamma_\mu + \tilde{G}_P(Q^2)\frac{q_\mu}{2M}\right]\gamma_5\tau^a u(\boldsymbol{p}), \tag{4.12}$$

where the axial-vector current is defined as $A^a_\mu = \bar{\psi}\gamma_\mu\gamma_5\tau^a\psi$. Here, τ^a serves as the isospin operator, and γ_μ and γ_5 are gamma matrices. Furthermore, the matrix element contains two Lorentz covariant components, consisting of the axial form factor G_A and the pseudo-scalar form factor $\tilde{G}_P$ along with their respective Lorentz structures. The nucleon spinor with momentum $\boldsymbol{p}$ is indicated as $u(\boldsymbol{p})$, and the momentum transfer is defined by $Q^2 = \boldsymbol{q}^2 - (E_{\boldsymbol{p}+\boldsymbol{q}} - E_{\boldsymbol{p}})^2$. The energy of the initial nucleon state is represented as $E_{\boldsymbol{p}}$. Lattice QCD research includes numerous investigations that compute various components of these matrix elements, such as those in [64–73] among others.
Chiral perturbation theory at leading-loop order has demonstrated that these axial form factors display significant excited-state systematics [74, 75] originating from nucleon-pion ($N\pi$) contamination. More current investigations have analyzed the chiral perturbation theory of the pion-nucleon sigma term, which shares physical characteristics similar to the axial vector current, up to the next-to-next-to-leading order (NNLO) [76] and further confirmed the existence of exited-state systematics. Such is also the case when considering the influence of the Δ-resonance [64].
Various research efforts have attempted to address $N\pi$ contamination using different methodologies [66, 67, 71, 77–79], focusing on three-quark interpolating operators. However, recent studies have investigated the integration of five-quark operators [43, 46, 80] and seven-quark operators [81], intended to improve the coupling with multi-hadronic

states such as $N\pi$ and $N\pi\pi$. The inclusion of multi-hadronic operators alongside conventional nucleon operators has proven effective in forming nucleon states with reduced $N\pi$ contamination [46, 80]. This thesis builds upon these efforts and intends to incorporate $N\pi\pi$ operators within a comprehensive GEVP analysis.
At the nucleon scale, the resonance region encompasses neutrino interactions with nucleons, described by the reactions

$$N\ \nu_\mu \to X\ \ell^- \quad \text{and} \quad N\ \bar{\nu}_\ell \to X\ \ell^+, \tag{4.13}$$

where X represents resonances such as $\Delta(1232)$ or Roper resonance $N(1440)$, which subsequently decay into $N\pi$ or $N\pi\pi$ states. These processes are illustrated in the middle diagram of Fig. 4.5. Calculating the elements of the axial vector matrix using lattice QCD poses a significant challenge. For the $\Delta(1232)$ resonance, exploratory lattice studies are conducted with quark masses heavier than their physical values, where $\Delta(1232)$ remains stable [82–84]. With respect to the Roper resonance, the situation is different. The method of generating a state similar to the Roper resonance on the lattice remains an unresolved scientific question [45, 85, 86]. Recent investigations propose that the resonance is probably due to strong meson-baryon interactions, thereby highlighting the significance of multi-hadronic operators [87]. Particular attention is paid to the $N\pi\pi$ operators. Being the first investigation that includes $N\pi\pi$ states through a comprehensive analysis of the generalized eigenvalue problem, this thesis seeks to offer results that are beneficial for addressing this unresolved issue.
The final regime, namely deep inelastic scattering (depicted in the right diagram of Fig. 4.5), is beyond the scope of this thesis. For further details on this regime, the reader is directed to [60].
This section has outlined the relevance of the nucleon spectrum for understanding neutrino-nucleus scattering processes. Ch. 8 presents a detailed nucleon spectral analysis, which constitutes a central result of this thesis.

5. Technical Details and Framework

5.1. Ensembles

Tab. 5.1 presents all the ensembles used in this thesis, each generated by the RBC-UKQCD collaborations. These ensembles implement the Iwasaki gauge action (see Sec. 2.3) and feature $N_f = 2 + 1$ Möbius domain-wall fermion (refer to Sec. 2.6) sea quarks. The upper part of the table refers to the ensembles utilized in the nucleon spectroscopy chapter (Ch. 8) related to the study [5]. The lower part enumerates the ensembles employed in Ch. 7, which performs a sub-analysis of [4].

5.2. Statistics

Due to the probabilistic nature of Monte Carlo calculations, expectation values, represented as $\langle \mathcal{O} \rangle$, are calculated using specific probability distributions. As a result, in the following section we will provide a brief review of probability theory based on [6, 88, 89]. Consider a vector $\boldsymbol{X} = (X_1, \ldots, X_n)^T$ of multivariate random variables from $\mathbb{R}^n$, characterized by the probability density function (PDF) $p_{\boldsymbol{X}}(x)$. The expectation of a function $f : \mathbb{R}^n \to \mathbb{R}$ that is based on the random variables $\boldsymbol{X}$ is given by

$$\langle f(\boldsymbol{X}) \rangle = \int \mathrm{d}x^n f(x) p_{\boldsymbol{X}}(x). \tag{5.1}$$

The mean, or expectation, of $\boldsymbol{X}$ is represented by the vector

$$\langle \boldsymbol{X} \rangle = \left(\langle X_1 \rangle, \ldots, \langle X_n \rangle \right)^T, \tag{5.2}$$

with each component calculated as

$$\langle X_i \rangle = \int \mathrm{d}x^n x_i p_{\boldsymbol{X}}(x). \tag{5.3}$$

In addition to the first moment of the probability distribution $p_{\boldsymbol{X}}$, the covariance matrix, considered as the second central moment, is of significance and is defined as

$$\mathrm{Cov}[\boldsymbol{X}] = \left\langle \left(\boldsymbol{X} - \langle \boldsymbol{X} \rangle \right) \left(\boldsymbol{X} - \langle \boldsymbol{X} \rangle \right)^T \right\rangle = \left\langle \boldsymbol{X} \boldsymbol{X}^T \right\rangle - \langle \boldsymbol{X} \rangle \langle \boldsymbol{X} \rangle^T, \tag{5.4}$$

resulting in an $n \times n$ matrix. We call X_i independent if the relationship $p_{\boldsymbol{X}}(x) = p_{X_1}(x) \ldots p_{X_n}(x)$ holds.
Consider n independent random variables $X_1, \ldots, X_N$, each characterized by the probability density function $p(x)$, with an expectation value $\langle X_i \rangle = \mu$ and a finite covariance $\mathrm{Cov}[X_i]$. The mean of these random variables can be expressed as

$$\hat{X} = \frac{1}{n} \sum_{i=1}^{n} X_i, \tag{5.5}$$

Ens-Id	$L^3 \times T \times L_s$	m_π/MeV	m_K/MeV	a^{-1}/GeV	N_{conf}	N_c	$m_\pi L$
4	$24^3 \times 48 \times 24$	274.8(2.5)	530.1(3.1)	1.7312(28)	94	60	3.8
D	$32^3 \times 64 \times 24$	274.8(2.5)	530.1(3.1)	1.7312(28)	60	60	5.1
9	$32^3 \times 64 \times 12$	278.9(4.9)	531.2(4.9)	2.3549(49)	60	60	3.8
L	$64^3 \times 128 \times 24$	278.9(4.9)	531.2(4.9)	2.3549(49)	20	60	7.6
1	$32^3 \times 64 \times 24$	208.1(1.1)	514.0(1.8)	1.7312(28)	34	60	3.8
3	$32^3 \times 64 \times 24$	211.3(2.3)	603.8(6.1)	1.7312(28)	34	60	3.8
C	$64^3 \times 128 \times 24$	139.32(30)	499.44(88)	1.7312(28)	25	120	5.2
48I	$48^3 \times 96 \times 24$	139.32(30)	499.44(88)	1.7312(28)	27	60	3.9
64I	$64^3 \times 128 \times 12$	138.98(43)	507.5(1.5)	2.3549(49)	31	60	3.8
96I	$96^3 \times 192 \times 12$	131.29(66)	484.5(2.3)	2.6920(67)	18	200	4.7
C	$64^3 \times 128 \times 24$	139.32(30)	499.44(88)	1.7312(28)	18	200	5.2

Table 5.1.: Summary of all the ensembles utilized in this thesis, where N_c denotes the number of eigenmodes of the Laplace operator that are used. The upper half of the tables presents the ensembles applied for Ch. 8, and the lower half displays those for Ch. 7. Ensemble C is employed in both chapters, although a different number of Laplace eigenmodes are applied. Each ensemble consists of N_{conf} independent configurations. The lattice spacings a are determined by the physical pion mass ensembles 48I, 64I, and 96I. Ensembles 4, D, 1, 3, and C align with 48I, while ensembles L and 9 correspond to 64I. Furthermore, for ensembles differing solely in volume, the same pion and kaon masses are used. The ensembles are originally generated for the g-2 effort of the RBC/UKQCD collaborations [4].

The central limit theorem states that as n increases, the distribution of $\hat{X}$ tends toward a normal distribution with the mean $\langle \hat{X} \rangle = \mu$ and the covariance $\mathrm{Cov}[\hat{X}] = \frac{1}{n}\mathrm{Cov}[X_i]$.
For a single random variable $\boldsymbol{X}$ with samples $x_1, \ldots, x_N \in \mathbb{R}^n$ drawn from the probability density function $p_{\boldsymbol{X}}(x)$, the sample mean is unbiased and can be calculated as

$$\tilde{x}_N = \frac{1}{N} \sum_{i=1}^{N} x_i, \tag{5.6}$$

where unbiasedness implies $\lim_{N\to\infty} \tilde{x}_N = \langle \boldsymbol{X} \rangle$. The unbiased estimation of variance is defined as

$$\widetilde{\mathrm{Var}}[\boldsymbol{X}] = \frac{1}{N-1} \sum_{i=1}^{N} (x_i - \tilde{x}_N)^2. \tag{5.7}$$

In this thesis, our primary focus is on functions of the mean, represented as $f(\langle x \rangle)$, which we typically approximate by

$$f(\langle x \rangle) \approx f(\tilde{x}_N). \tag{5.8}$$

There are various techniques to estimate variance, including bootstrap [90] and jackknife resampling [91]. In this work, we use the jackknife method, which constructs mean estimates by excluding one element at a time. The configuration with one element omitted is defined as

$$\tilde{x}_j \equiv \frac{1}{N-1} \sum_{i=1, i\neq j}^{N} x_i = \tilde{x}_N + \frac{1}{N-1}(\tilde{x} - x_j). \tag{5.9}$$

The jackknife estimate of the variance for f is given by

$$\widetilde{\mathrm{Var}}^J[f, \boldsymbol{X}] = \frac{N-1}{N} \sum_{j=1}^{N} \left(f(\tilde{x}_j) - f(\tilde{x})\right)^2. \tag{5.10}$$

5.3. Statistics Analysis

The following statistical analyses are performed using QStatPy [92]. The Python library takes its inspiration from JKS [93]. The idea is to create a lightweight database system structured as nested dictionaries, consisting of three hierarchical layers:

1. The overall tag, which describes the ensemble along with a description of the original quantity, such as the nucleon two-point function for ensemble 4.

2. The sample tag refers to the jackknife samples of relevant secondary quantities, like the effective mass, or the jackknife samples themselves. At this level, one sample tag often also identifies the raw data, usually denoted as `CONFIG`.

3. The configuration tag, which specifies the sample configuration. For jackknife samples, there is an extra tag called `mean`, representing the ensemble average. Moreover, the configuration tag points to the jackknife sample excluding the data from this specific configuration.

The typical utilization scenario is demonstrated through an example. Assume that our aim is to investigate the nucleon two-point function within ensemble 1. The configuration identifiers used for ensemble 1 include `1-400`, `1-410`, up to `1-730`, representing the configuration labels. We begin by uploading the raw correlation data, formatted as `np.array`, into the database, adopting the general label `ens1/N2N`, which stands for nucleon to nucleon for ensemble 1. For the raw data sample tag, `CONFIG` is commonly used. Subsequently, we generate jackknife samples, which are organized under the tags `ens1/N2N` and `jk-mean`, along with the specific configuration tags. In this context, `1-400` denotes the jackknife mean that excludes this particular configuration. Additionally, for the jackknife samples, we create an entry labeled `mean` for storing the complete mean. These jackknife samples are then used for every derived quantity, such as the effective mass curve, where the mean and variance are calculated using Eq. 5.8 and Eq. 5.10, respectively.
In scenarios where various correlation functions are significant, such as in the case of the GEVP, we are able to merge the distinct jackknife samples into a single unified jackknife sample. When both global tags share the same configuration, this process is quite straightforward. However, if they possess different configurations, the jackknife samples for the missing configuration are assigned the mean value.

5.4. Markov Chain and Autocorrelation

The gauge configurations used to evaluate the correlation functions are part of a Markov chain. Typically, a Markov chain is defined by a random variable X that undergoes stochastic evolution in discrete increments. The variable value at step τ, known as Markov time, is determined solely by the preceding step $\tau - 1$. In lattice QCD, we focus exclusively on irreducible and aperiodic Markov chains, which have the characteristic of converging to a stationary distribution after a sufficiently long Markov time τ. However, since the chain element at Markov time τ depends on the prior step, some autocorrelation between the two elements is expected. Only for greater Markov time separations does the autocorrelation become negligible. The algorithm significantly influences the level of anticipated autocorrelation in use. Moreover, for the initial element of the Markov chain, known as the seed, we often select elements that are rare events in the stationary distribution. Therefore, we must first allow the Markov chain to equilibrate to the stationary distribution and then utilize the samples from the equilibrated chain for our computations. In addition to equilibration, we also want our samples to be independent of each other. Here, we typically use only every n-th element of the chain for our calculation to avoid significant autocorrelation. To quantify the autocorrelation, we define the autocorrelation function between Markov time τ_0 and τ_1

$$C_X(\tau_1, \tau_0) = \langle (X_{\tau_1} - \langle X \rangle)(X_{\tau_0} - \langle X \rangle) \rangle \,. \tag{5.11}$$

For the chain in equilibrium, the autocorrelation function is invariant under Markov time shifts and, therefore, only depends on the Markov time separation $\tau = \tau_1 - \tau_0$, yielding

$$C_X(\tau) = C_X(\tau_1, \tau_0). \tag{5.12}$$

Without time separation, the autocorrelation function is the variance $C_X(0) = \sigma_X^2$ of X. Typically, one normalizes the autocorrelation function according to this variance to obtain

$$\rho_X(\tau) = \frac{C_X(\tau)}{C_X(0)}. \tag{5.13}$$

In equilibrated, irreducible, and aperiodic Markov chains, the autocorrelation function diminishes exponentially, which can be represented as

$$\rho_X(\tau) \sim \exp\left(-\frac{\tau}{\tau_{X,\text{exp}}}\right), \tag{5.14}$$

where $\tau_{X,\text{exp}}$ denotes the exponential autocorrelation time. Due to noise influencing the autocorrelation function, it is often better to estimate the exponential Markov time using the integrated Markov time $\tau_{X,\text{int}}$, defined by

$$\tau_{X,\text{int}} \equiv \frac{1}{2} + \sum_{\tau=1}^{C} \rho_X(\tau) \approx \int \mathrm{d}\tau e^{-\frac{\tau}{\tau_{X,\text{exp}}}} = \tau_{X,\text{exp}}, \tag{5.15}$$

where a cutoff C is introduced to ensure that $\rho(\tau)$ values beyond C are not used due to unreliability.
Throughout this thesis, we always use gauge configurations of an equilibrated Markov chain, which are separated large enough that we can treat the configurations as uncorrelated. For a more detailed discussion of Markov chains, we refer to [6, 88], which is also the basis for this short introduction.

5.5. Fitting

In the analysis done throughout this thesis, we use different fitting procedures. Hence, the following section introduces the general fitting procedure in the context of Bayesian inference. In general, the idea of fitting is to describe some given data D by a model M. The model M depends on a set of parameters θ that are optimized to give the best fit. In Bayesian inference terminology, this involves maximizing the posterior probability, which is calculated using Bayes' theorem:

$$P(M|D) = \frac{P(D|M)P(M)}{P(D)}, \tag{5.16}$$

and represents the probability of the model M given the data D. The calculation of the posterior requires the prior probability $P(M)$, the likelihood $P(D|M)$, and the data probability $P(D)$, the latter being model independent and not affecting the optimization of $P(M|D)$. In the absence of prior knowledge regarding the probabilities of various models, the prior probability is generally assumed to be constant. This simplifies the optimization of the posterior probability $P(M|D)$ to that of the likelihood $P(D|M)$.
Assume that the data set consists of the input variables $x_i \in \mathbb{R}^n$ and the corresponding output variables $y_i \in \mathbb{R}$. Our model M utilizes the input variables x_i along with the model parameters $\boldsymbol{\theta}$ to predict the output variables. According to the central limit theorem, the deviation ε_i between the model predictions and actual data,

$$\varepsilon_i = y_i - M(x_i; \boldsymbol{\theta}), \tag{5.17}$$

can be approximated as a multivariate normal distribution with a mean of zero and a finite covariance matrix Σ. The probability distribution of the data given the model M is expressed as

$$P(D|M) \sim \frac{1}{\sqrt{\det[\Sigma](2\pi)^n}} \exp\left(-\frac{1}{2}\boldsymbol{\varepsilon}^T\Sigma^{-1}\boldsymbol{\varepsilon}\right). \tag{5.18}$$

Optimizing $P(D|M)$ is equivalent to minimizing the expression

$$\chi^2(\boldsymbol{\theta}) = \sum_{ij}\left(y_i - M(x_i;\boldsymbol{\theta})\right)\left[\Sigma^{-1}\right]_{ij}\left(y_j - M(x_j;\boldsymbol{\theta})\right). \tag{5.19}$$

Minimization is achieved through standard optimization algorithms, among these, the Levenberg-Marquardt algorithm has been identified as particularly advantageous [94, 95]. Therefore, throughout this thesis, Levenberg-Marquardt has been employed for all fitting procedures. The optimized χ^2 values are characterized by a distinct distribution known as the chi-square distribution, which is represented by the probability density function (PDF)

$$p(x,k) = \frac{1}{\sqrt{2^k}\Gamma(k/2)}x^{k/2-1}e^{-x/2}, \tag{5.20}$$

where k signifies the degrees of freedom. In the context of our analysis, k is determined by subtracting the number of parameters to optimize, indicated as K, from the total number of data points N. Consequently, k can be expressed as $k = N - K$. The mean value of the chi-square distribution is k, and therefore we expect that the χ^2 values have a high chance of being close to k. This property serves to introduce a single measure that characterizes the quality of fit: the reduced chi-square

$$\chi^2_{\text{red}} = \frac{\chi^2}{k}. \tag{5.21}$$

A value of χ^2_{red} close to 1 suggests a good fit, as this is the most probable scenario. Nevertheless, the limitation of the reduced chi-square is that it omits the shape of the distribution, which significantly depends on the number of degrees of freedom. Thus, a better metric for fit quality is the p-value

$$P = \int_{\chi^2}^{\infty} \mathrm{d}x p(x,k), \tag{5.22}$$

which quantifies the probability of observing a larger χ^2 value. To achieve a satisfactory fit, the p-values must exceed a predetermined threshold P_0. In our study, we opt for a threshold value of $P_0 = 0.05$.

A typical use case of fitting throughout this thesis is the fitting of effective mass curves $m(t)$ in a fit range window $\tau_0 \leq t \leq \tau_1$. To properly minimize Eq. 5.19, we need a reliable estimate of the covariance matrix $\Sigma = \langle(m(t) - \langle m(t)\rangle)(m(t') - \langle m(t')\rangle)\rangle$ for t, t' within the time window. Unfortunately, due to limited statistical data, the covariance matrix is often poorly determined, which can destabilize the fit. Consequently, it is common to treat individual time slices as uncorrelated, thus considering the covariance matrix as diagonal, that is, $\Sigma_{ij} = \sigma_i(t)^2\delta_{ij}$. This fitting approach, termed an uncorrelated fit, is applied in various situations throughout this thesis. Removing the correlation between various time

slices undermines the statistical interpretation of the optimized χ^2, thus rendering the p-value an unreliable indicator of the quality of the fit. In these cases, we instead rely on the reduced chi-square value as an alternative measure of fit quality, aiming for this value to be minimized as much as possible. In this context, assuming that the individual data points are uncorrelated, χ^2 denotes the average squared difference between the model predictions and the data points, weighted by the uncertainty associated with the data points.
To test the predictive power of our fits, we introduce another measure called the **extrapolation check** defined as the tension of the data point $(\tau_0 - a,\, m(\tau_0 - a))$ and the prediction of the fit $M(\tau_0 - a)$, that is,

$$\sigma_{\tau_0 - a} = \frac{\sigma[m(\tau_0 - a) - M(\tau_0 - a; \boldsymbol{\theta})]}{E[m(\tau_0 - a) - M(\tau_0 - a; \boldsymbol{\theta})]}, \tag{5.23}$$

where $\sigma[X]$ and $E[X]$ denote the standard deviation and expectation value of X. In this thesis, we select one of the fitting ranges that meets the extrapolation check with tensions of $|\sigma_{\tau_0 - a}| < 2$. There exist certain exceptions in Sec. 8.2, where no fitting range that satisfies this tension is obtained. Thus, the range with the least tension is selected.

5.6. All Mode Averaging

In lattice QCD, acquiring accurate results necessitates sufficient statistical data, which can be achieved by increasing the number of elements in the Markov chain. However, when calculating correlation functions, we do not always take advantage of all available information from gauge configurations. As discussed in Sec. 2.8, we usually solve the quark propagator only for a subset of space-time combinations, often focusing on particular points or chosen sources. The invariance of space-time ensures that this selected subset still yields accurate results, albeit with a reduction in the stochastic data utilized, thereby increasing the statistical error. Determining the inverse of the Dirac matrix is a resource-intensive task, especially concerning domain-wall fermions. However, by calculating a matrix that closely approximates the true quark propagator, we can significantly reduce computational expenses. These approximations are called "sloppy" solves. It is important to note that technically we do not compute the exact inverse, as algorithms allow only an approximate solution with a certain residual. Nevertheless, for sloppy solves, our approach involves relaxing the stopping criterion of the inversion process even further. In addition, we reduce machine precision to single floating point calculations in our framework to further minimize computational costs.
The concept of all-mode averaging (AMA), as initially proposed in various formats in [96–98], revolves around the extension of statistical samples using inexpensive and imprecise solutions. In this thesis, the approach involves determining the sloppy solution for a collection of sources Λ. The exact solutions are calculated only for a smaller subset $\Lambda_0 \subset \Lambda$. If one relied solely on the sloppy solutions, a bias could be introduced. This bias can be quantified by assessing the difference between the exact and approximate solutions within the subset Λ_0, expressed as

$$\langle B \rangle_{\Lambda_0} = \langle X - S \rangle_{\Lambda_0}, \tag{5.24}$$

where S denotes the sloppy, and X the exact solution for the corresponding quantity. When Λ_0 is chosen as a representative subset of Λ, it can be determined that the expectation value $\langle B \rangle$ remains consistent between different sets. In other words, $\langle B \rangle_{\Lambda_0} = \langle B \rangle_{\Lambda}$.

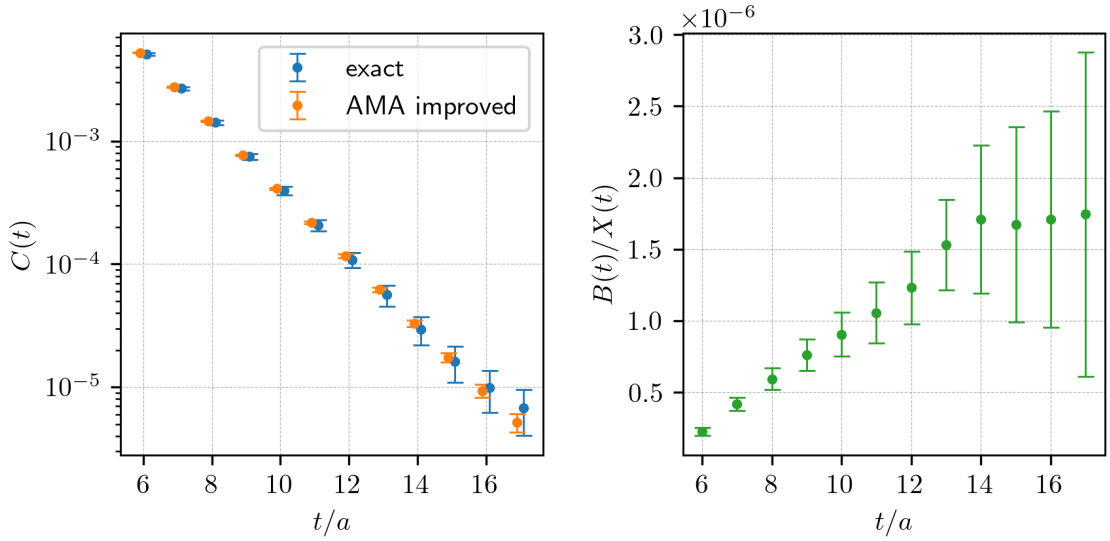

Figure 5.1.: Left: Comparison of statistical uncertainties in the nucleon two-point correlation function for ensemble 4 when using all-mode averaging (AMA) versus relying solely on exact solutions, demonstrating the improvement in precision achieved with AMA. Right: Ratio of the bias to the exact solution, quantifying the systematic effect introduced by the approximation. Both results are obtained using the distillation method.

This outcome is employed to calculate the unbiased overall expectation value, expressed as

$$\langle F \rangle_\Lambda = \langle B \rangle_{\Lambda_0} + \langle S \rangle_\Lambda. \tag{5.25}$$

When the variance of B is significantly smaller than that of S, and the covariance between B and S is minimal, which are conditions commonly observed in practice, the variance of the total F is primarily determined by the variance of S for the entire set Λ, given by

$$\mathrm{Var}[F]_\Lambda \approx \mathrm{Var}[S]_\Lambda < \mathrm{Var}[X]_\Lambda. \tag{5.26}$$

Fig. 5.1 illustrates the impact of the AMA enhancement on the two-point nucleon correlation function. The plot on the left shows a noticeable reduction in statistical noise when implementing the AMA improvement compared to relying solely on the exact solution. Meanwhile, the right-hand graph displays the relative bias compared to the exact solution. It is evident that this bias is insignificant, being six orders of magnitude smaller than the exact signal. Consequently, both the variance of the bias and its covariance with the imprecise correlation function are effectively negligible.

5.7. Distillation

In Sec. 2.8, we touched on various smearing techniques, including the distillation method, although we did not elaborate on it there. This section aims to provide a concise introduction to the distillation method. Originally presented in [99], the method uses the

eigenvectors of the gauge-covariant Laplace operator. These eigenvectors serve as smeared sources, facilitating an effective overlap with the low-mode states characteristic of the theory.
In this thesis, we employ the Laplace operator defined by the equation

$$L(\mathbf{x},\mathbf{y}) = -\delta_{\mathbf{x},\mathbf{y}} + \frac{1}{6a^2}\sum_i \left(U_i(\mathbf{x})\delta_{\mathbf{x},\mathbf{y}-a\hat{i}} + U_i^\dagger(\mathbf{x}-a\hat{i})\delta_{\mathbf{x},\mathbf{y}+a\hat{i}}\right). \tag{5.27}$$

We find the eigenvectors by solving the eigenvalue problem expressed as

$$\sum_{\mathbf{y}} L(\mathbf{x},\mathbf{y})V^n(\mathbf{y}) = V^n(\mathbf{x})\lambda^n, \tag{5.28}$$

ensuring that the eigenvalues are in ascending order, where $\lambda^m \geq \lambda^n$ for $m > n$. The corresponding eigenvectors are V^n. To enhance the long-range properties, Gaussian smearing is applied to the Laplace operator's link variables U_i. The parameters of the smearing process are $\rho = 0.1$ and $N = 30$. We utilize a four-dimensional smearing approach. However, to preserve temporal locality, we neutralize all time slices except within a small range around $t-a, t, t+a$. Only the central slice t is preserved after smearing, and this procedure is repeated for each time slice of the setup (see [100] for additional details).
The eigenvectors from Eq. 5.28 serve as the sources to solve the Dirac equation relating to the quark propagator G. This equation is formulated as follows:

$$\sum_y \sum_\mu \gamma_\mu D_\mu(x,y) G_c^n(t_y, t_x, \boldsymbol{y}) = V_c^n(x), \tag{5.29}$$

where the spin and color indices are not explicitly shown. Quark propagators that use V^n as their source components are commonly referred to as **half-perambulators**.
Employing the eigenvectors as sinks results in the formation of **perambulators**, which are defined as

$$\mathcal{G}^{mn}(t_y, t_x) = \sum_{\boldsymbol{y}} \sum_c V_c^m(t_y, \boldsymbol{y})^\dagger G_c^n(t_y, t_x, \boldsymbol{y}), \tag{5.30}$$

For simplicity, we omit the explicit spin indices. It is essential to note that the perambulator does not include a color index, as such indices are integrated by contracting with the Laplace eigenmodes. Perambulators can be understood as propagators within the eigenmode basis of the Laplace operator. For the usual number of modes employed, we truncate contributions from high-mode states. The impact of this truncation is observable in the negative parity sector described in Sec. 8.2. However, the primary benefit of using perambulators is that, while their computation is costly, they offer significant storage efficiency. This becomes evident when comparing a perambulator that utilizes 60 eigenmodes for the ensemble 4 to an all-to-all propagator on a $24^3 \times 48$ lattice, where the latter demands roughly 0.5×10^6 times more storage.
The distillation method can also be interpreted as a procedure for smearing quark fields. This is done by defining the distillation operator as follows:

$$\square(\boldsymbol{x},\boldsymbol{y},t)_{cc'} = \sum_{k=1}^{N_d} V_c^k(\boldsymbol{x},t)\left[V_{c'}^k(\boldsymbol{y},t)\right]^\dagger, \tag{5.31}$$

which results in the smearing of a point-like quark field through the expression:

$$\psi^S_{\alpha,c}(x) = \sum_{\boldsymbol{y}} \square(\boldsymbol{x},\boldsymbol{y},t)_{cc'}\psi_{\alpha,c'}(y). \tag{5.32}$$

The quark propagator of the smeared quarks is related to the perambulator by the basis transformation

$$G^S_{\substack{\alpha\alpha'\\cc'}}(y|x) = \left\langle \psi^S_{\alpha,c}(\boldsymbol{y},t_y)\bar{\psi}^S_{\alpha',c'}(\boldsymbol{x},t_x)\right\rangle = \sum_{n,m} V^n_c(\boldsymbol{y},t_y)\mathcal{G}^{nm}_{\alpha\alpha'}(t_y,t_x)\left[V^m_{c'}(\boldsymbol{x},t_x)\right]^\dagger. \tag{5.33}$$

Substituting this smeared quark propagator into the pion correlation function from Eq. 2.106 results in

$$C^S_{\pi\pi}(t,\boldsymbol{p}) = -\left\langle \mathrm{tr}\left[\mathcal{G}^{mm'}(t,0)\mathcal{P}^{m'n'}(0,-\boldsymbol{p})\gamma_5\mathcal{G}^{n'n}(0,t)\gamma_5\mathcal{P}^{nm}(t,\boldsymbol{p})\right]\right\rangle, \tag{5.34}$$

with the **momentum insertion** $\mathcal{P}(t,\boldsymbol{p})$ specified as

$$\mathcal{P}^{nm}(t,\boldsymbol{p}) = \sum_{\boldsymbol{x}}\sum_{c}\left[V^n_c(\boldsymbol{x},t)\right]^\dagger e^{i\boldsymbol{x}\cdot\boldsymbol{p}}V^m_c(\boldsymbol{x},t). \tag{5.35}$$

One can show that correlation functions that involve only mesons can be developed exclusively through the use of perambulators and momentum insertions. This approach highlights the significant benefit associated with the distillation method. After we have calculated the perambulators for the necessary quarks, all that remains is to combine the various distillation components, specifically the perambulator and momentum insertion relevant to mesons.
Baryons add an extra layer of complexity to the situation. Let us first review the nucleon correlation function mentioned in Eq. 2.110. This correlation function has been identified as the sum of two distinct terms:

$$\mathbb{T}_{UC\gamma_5,C\gamma_5D,G}(\boldsymbol{p},t)_{\alpha\alpha'} = \sum_{\boldsymbol{x},\boldsymbol{y}} e^{-i\boldsymbol{p}\cdot(\boldsymbol{y}-\boldsymbol{x})}\mathrm{tr}_c\left[\mathrm{tr}_s[Q^{NN}(x|y)]G(x|y)\right], \tag{5.36}$$

$$\mathbb{L}_{UC\gamma_5,C\gamma_5D,G}(\boldsymbol{p},t)_{\alpha\alpha'} = \sum_{\boldsymbol{x},\boldsymbol{y}} e^{-i\boldsymbol{p}\cdot(\boldsymbol{y}-\boldsymbol{x})}\mathrm{tr}_c\left[Q^{NN}(x|y)G(x|y)\right], \tag{5.37}$$

which collectively form the nucleon correlation function as:

$$C_{NN}(t,\boldsymbol{p}) = \langle \mathrm{tr}\left[P_+\left(\mathbb{T}_{UC\gamma_5,C\gamma_5D,G}(\boldsymbol{p},t) + \mathbb{L}_{UC\gamma_5,C\gamma_5D,G}(\boldsymbol{p},t)\right)\right]\rangle. \tag{5.38}$$

The terms represent different types of contractions that occur in general baryon correlation functions. We define contractions similar to those in Eq. 5.36 as **trace-full** contractions, whereas those similar to Eq. 5.37 are termed as **trace-less** contractions. By employing perambulators, both terms can be reformulated to

$$\mathbb{T}(\boldsymbol{p},t)_{\alpha\alpha'} = \mathcal{E}^{\ell nm}(t,\boldsymbol{p})\mathcal{U}^{nn'}_{\beta\gamma}(t,0)(C\gamma_5)_{\gamma\beta'}(C\gamma_5)_{\beta\gamma'}\mathcal{D}^{mm'}_{\gamma'\beta'}(t,0)\mathcal{G}^{\ell\ell'}_{\alpha\alpha'}(t,0)\left[\mathcal{E}^{\ell'n'm'}(0,\boldsymbol{p})\right]^\dagger, \tag{5.39}$$

$$\mathbb{L}(\boldsymbol{p},t)_{\alpha\alpha'} = \mathcal{E}^{\ell nm}(t,\boldsymbol{p})\mathcal{U}^{nn'}_{\alpha\gamma}(t,0)(C\gamma_5)_{\gamma\beta'}(C\gamma_5)_{\beta\gamma'}\mathcal{D}^{mm'}_{\gamma'\beta'}(t,0)\mathcal{G}^{\ell\ell'}_{\beta\alpha'}(t,0)\left[\mathcal{E}^{\ell'n'm'}(0,\boldsymbol{p})\right]^\dagger, \tag{5.40}$$

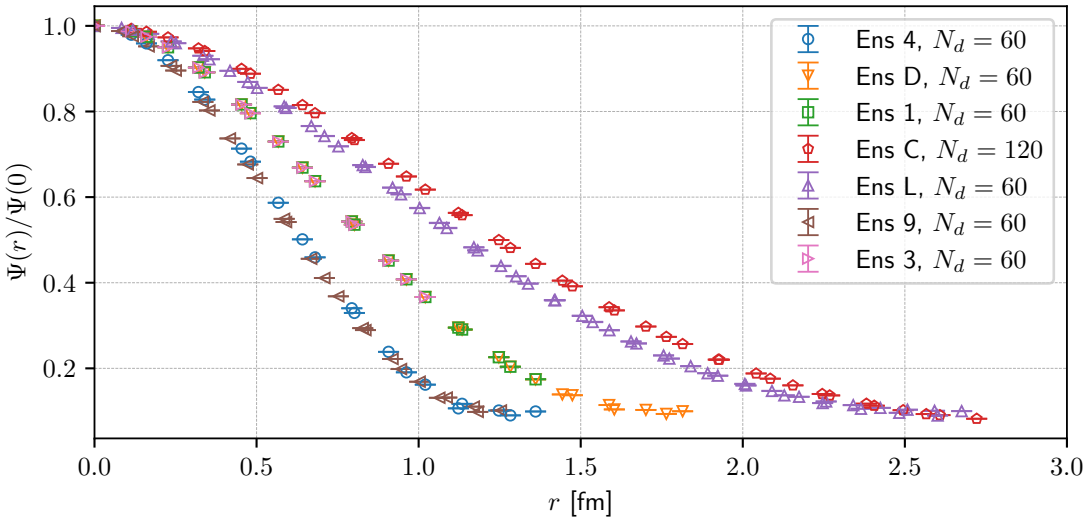

Figure 5.2.: The profile $\Psi(\boldsymbol{r})$ is expressed as $\sum_{\boldsymbol{x},t} \sqrt{\mathrm{tr}_c\left[\square(\boldsymbol{x}, \boldsymbol{x}+\boldsymbol{r}, t)\square(\boldsymbol{x}+\boldsymbol{r}, \boldsymbol{x}, t)\right]}$ for all the ensembles utilized in [5]. In particular, the data points for ens D, ens 1, and ens 3 coincide, demonstrating that the pion mass does not influence the smearing effect observed in the distillation method.

where there is an implicit summation over repeated indices and the indices of $\mathbb{T}$ and $\mathbb{L}$ are dropped for visual reasons. We further introduce the **modified elementals** by

$$\mathcal{E}^{\ell nm}(t, \boldsymbol{p}) = \sum_{\boldsymbol{x}} \varepsilon_{abc} V_a^{\ell}(\boldsymbol{x}, t) V_b^{n}(\boldsymbol{x}, t) V_c^{m}(\boldsymbol{x}, t) e^{-i\boldsymbol{p}\cdot\boldsymbol{x}}, \tag{5.41}$$

which resembles the structure utilized in previous works like [47] and [101]. However, in our approach, we exclude any inclusion of the spin structures. To reduce the computational cost associated with the calculation and storage of these elements, we can exploit the permutation properties of the Levi-Civita tensor. It is sufficient to compute all ordered tuples (ℓ, n, m) where $\ell < n < m$. The remaining permutations $\sigma(\ell, n, m)$ can then be derived using

$$\mathcal{E}^{\sigma(\ell,n,m)} = \mathrm{sign}[\sigma(\ell, n, m)]\mathcal{E}^{\ell nm}. \tag{5.42}$$

This reduces the computational cost by a factor of

$$R(N_c) = \frac{N_c(N_c-1)(N_c-2)}{6N_c^3} = \frac{1}{6} - \frac{1}{2N_c} + \frac{1}{3N_c^2}. \tag{5.43}$$

In addition, the distillation operator mentioned in Eq. 5.31 allows us to introduce a measure of the effective smearing width in this distillation process called the profile. This profile is defined by the following equation:

$$\Psi(\boldsymbol{r}) = \sum_{\boldsymbol{x},t} \sqrt{\mathrm{tr}_c\left[\square(\boldsymbol{x}, \boldsymbol{x}+\boldsymbol{r}, t)\square(\boldsymbol{x}+\boldsymbol{r}, \boldsymbol{x}, t)\right]}. \tag{5.44}$$

Fig. 5.2 shows the complete set of profiles for the ensembles utilized in Ch. 8. It is evident from the figure that ensembles 4 and 9 exhibit the sharpest profiles, suggesting that these

$\mathcal{O}_A/\mathcal{O}_B$	p	$n\pi^+$	$p\pi^0$	$p\pi^+\pi^-$	$p\pi^0\pi^0$
p	2	4	6	12	26
$n\pi^+$	4	12	16	36	84
$p\pi^0$	6	16	26	60	138
$p\pi^+\pi^-$	12	36	60	144	372
$p\pi^0\pi^0$	26	84	138	372	882

Table 5.2.: Number of non-vanishing diagrams for each correlation function $C_{AB}(t, \boldsymbol{p}, \boldsymbol{q}) = \left\langle \mathcal{O}_A(t, \boldsymbol{p}) \mathcal{O}_B^\dagger(0, \boldsymbol{q}) \right\rangle$.

ensembles' distillation smearing has the greatest overlap with the theory's high-mode states.

5.8. Automatic Wick Contraction

This section will explore general correlation functions involving a single nucleon and any number of pions at both the source and the sink. The objective is to automate the contraction of these correlation functions utilizing Wick's theorem (refer to Sec. 2.7), and subsequently translate these contracted correlation functions into a combination of precomputed distillation elements, such as perambulators, momentum insertions, and modified elementals. A Python code for implementing this automatic contraction is available in [102].
This automated Wick contraction is especially relevant for Ch. 8, where we consider spectroscopy of the nucleon, nucleon-pion, and nucleon-pion-pion states. Here, due to the sheer amount of contraction, summarized in Tab. 5.2, the need for automatic contractions of the correlation functions arises.
To make the explanation of the algorithm behind the automatic contraction more comprehensible, we first make the following assumptions without loss of generality:

1. The nucleon operators at the sink consistently take the form

$$\mathcal{O}_p(x)_\xi = \varepsilon_{abc} P^+_{\xi\alpha} u_{\alpha,a}(x) u_{\beta,b}(x) d_{\gamma,c}(x) \Gamma^T_{\beta\gamma}, \tag{5.45a}$$
$$\mathcal{O}_n(x)_\xi = \varepsilon_{abc} P^+_{\xi\alpha} d_{\alpha,a}(x) d_{\beta,b}(x) u_{\gamma,c}(x) \Gamma^T_{\beta\gamma}, \tag{5.45b}$$

   whether dealing with a proton p or a neutron n at the sink. It is crucial that the coordinates x, the spin indices (α, β, γ), and the color indices (a, b, c) are specifically associated with the nucleon in the sink. We further abbreviate these sets of position, spin and color indices as

$$A = (x, \alpha, a), \quad B = (x, \beta, b), \quad C = (x, \gamma, c). \tag{5.46}$$

2. Like the nucleon at the sink, we consistently use nucleon operators for the source:

$$\mathcal{O}^\dagger_p(y)_\rho = \varepsilon_{a'b'c'} \bar{d}_{\gamma',c'}(y) \bar{u}_{\beta',b'}(y) \bar{u}_{\alpha',a'}(y) \Gamma^S_{\beta'\gamma'} (\gamma_t P^+)_{\alpha'\rho} \tag{5.47a}$$
$$\mathcal{O}^\dagger_n(y)_\rho = \varepsilon_{a'b'c'} \bar{u}_{\gamma',c'}(y) \bar{d}_{\beta',b'}(y) \bar{d}_{\alpha',a'}(y) \Gamma^S_{\beta'\gamma'} (\gamma_t P^+)_{\alpha'\rho}, \tag{5.47b}$$

and we also use the shorthand notation:

$$A' = (y, \alpha', a'), \quad B' = (y, \beta', b'), \quad C' = (y, \gamma', c'). \tag{5.48}$$

3. For the representation of pions, we utilize the operators

$$\mathcal{O}_{\pi^+}(z) = \bar{d}_{\delta',d'}(z)\Gamma^{\pi}_{\delta'\delta}u_{\delta,d}(z)\delta_{d'd}, \tag{5.49a}$$
$$\mathcal{O}_{\pi^-}(w) = \bar{u}_{\epsilon',e'}(w)\Gamma^{\pi}_{\epsilon'\epsilon}d_{\epsilon,e}(w)\delta_{e'e}, \tag{5.49b}$$
$$\mathcal{O}_{\pi^0_u}(q) = \bar{u}_{\zeta',f'}(q)\Gamma^{\pi}_{\zeta'\zeta}u_{\zeta,f}(q)\delta_{f'f}, \tag{5.49c}$$
$$\mathcal{O}_{\pi^0_d}(s) = \bar{u}_{\eta',g'}(q)\Gamma^{\pi}_{\eta'\eta}u_{\eta,g}(s)\delta_{g'g}, \tag{5.49d}$$

where we use the letter abbreviations

$$D = (z, \delta, d), \quad E = (w, \epsilon, e), \quad F = (q, \zeta, f), \quad G = (s, \eta, g) \tag{5.50}$$

together with their respective primed versions. Note that these letters are not specifically assigned to individual pions. Instead, we first determine the alphabet for the pions at the sink and proceed to those at the source. The operator of the neutral pion is given by

$$\mathcal{O}_{\pi^0}(z) = \frac{1}{\sqrt{2}}\left(\mathcal{O}_{\pi_u}(z) - \mathcal{O}_{\pi_d}(z)\right). \tag{5.51}$$

We further will use the fact that

$$\mathcal{O}^{\dagger}_{\pi^{\pm}} = -\mathcal{O}_{\pi^{\mp}} \text{ and } \mathcal{O}^{\dagger}_{\pi^0_{u/d}} = -\mathcal{O}_{\pi^0_{u/d}}. \tag{5.52}$$

Under the given assumptions regarding the structure of the various operators, we will examine the algorithm for automatic Wick contraction systematically, using the following correlation function as an example:

$$C_{n\pi^+,n\pi^+}(t, \boldsymbol{p}, \boldsymbol{q})_{\xi\rho} = -\sum_{\boldsymbol{x},\boldsymbol{y},\boldsymbol{z},\boldsymbol{w}} e^{-i\boldsymbol{p}\cdot(\boldsymbol{x}-\boldsymbol{z})}e^{i\boldsymbol{q}\cdot(\boldsymbol{y}-\boldsymbol{w})}\langle\mathcal{O}_n(x)_{\xi}\mathcal{O}_{\pi^+}(z)\mathcal{O}_{\pi^-}(w)\mathcal{O}^{\dagger}_n(y)_{\rho}\rangle, \tag{5.53}$$

where the nucleon-pion configuration exhibits back-to-back momenta at both the source and the sink.

1. Insert the definitions of the operator
Inserting the interpolating operators yields for the correlation function

$$-\sum_{\boldsymbol{x},\boldsymbol{y},\boldsymbol{z},\boldsymbol{w}} e^{-i\boldsymbol{p}\cdot(\boldsymbol{x}-\boldsymbol{z})}e^{i\boldsymbol{q}\cdot(\boldsymbol{y}-\boldsymbol{w})}\varepsilon_{abc}\varepsilon_{a'b'c'}\Gamma^{T}_{\beta\gamma}\Gamma^{S}_{\beta'\gamma'}P^{+}_{\xi\alpha}(\gamma_3 P^{+})_{\alpha'\rho}\Gamma^{\pi^+}_{\delta'\delta}\Gamma^{\pi^-}_{\epsilon'\epsilon}\delta_{d'd}\delta_{ee'}$$
$$\times\left\langle d_A d_B u_C \bar{d}_{D'} u_D \bar{u}_{E'} d_E \bar{u}_{C'} \bar{d}_{B'} \bar{d}_{A'}\right\rangle, \tag{5.54}$$

with the above introduced short-hand notation $u_A = u_{\alpha,a}(x)$, where x belongs to A, B and C.
2. Ordering of the fermion fields
The next step is to bring all fermion fields in the expectation value to a predefined order by applying the anticommutation relations defined in Eq. 2.64, for which we get

$$-\left\langle d_A d_B u_C \bar{d}_{D'} u_D \bar{u}_{E'} d_E \bar{u}_{C'} \bar{d}_{B'} \bar{d}_{A'}\right\rangle = \left\langle d_A \bar{d}_{D'} d_B \bar{d}_{B'} d_E \bar{d}_{A'}\right\rangle_d \langle u_C \bar{u}_{E'} u_D \bar{u}_{C'}\rangle_u, \tag{5.55}$$

where we split the fermion expectation value into the different flavors.

3. Applying Wick's theorem

Applying Wick's theorem (see Eq. 2.75) onto the fermion expectation values yields

$$\begin{aligned}
-\left\langle d_A d_B u_C \bar{d}_{D'} u_D \bar{u}_{E'} d_E \bar{u}_{C'} \bar{d}_{B'} \bar{d}_{A'} \right\rangle = \\
&- D_{AD'} D_{BB'} D_{EA'} U_{CE'} U_{DC'} + D_{AD'} D_{BB'} D_{EA'} U_{CC'} U_{DE'} \\
&+ D_{AD'} D_{BA'} D_{EB'} U_{CE'} U_{DC'} - D_{AD'} D_{BA'} D_{EB'} U_{CC'} U_{DE'} \\
&+ D_{AB'} D_{BD'} D_{EA'} U_{CE'} U_{DC'} - D_{AB'} D_{BD'} D_{EA'} U_{CC'} U_{DE'} \\
&- D_{AB'} D_{BA'} D_{ED'} U_{CE'} U_{DC'} + D_{AB'} D_{BA'} D_{ED'} U_{CC'} U_{DE'} \\
&- D_{AA'} D_{BD'} D_{EB'} U_{CE'} U_{DC'} + D_{AA'} D_{BD'} D_{EB'} U_{CC'} U_{DE'} \\
&+ D_{AA'} D_{BB'} D_{ED'} U_{CE'} U_{DC'} - D_{AA'} D_{BB'} D_{ED'} U_{CC'} U_{DE'},
\end{aligned} \tag{5.56}$$

where we extend the short-hand notation to propagators such that

$$G_{AB'} = \underset{ab'}{G_{\alpha\beta'}}(x|y), \tag{5.57}$$

where G can be U for up and D for down quarks, respectively.

4. Finding all sequential propagators

The following stage involves organizing all propagators that are not connecting x and y, into sequences that form connections between the source and sink nucleons. This particular sequence is termed a sequential propagator, and it can be expressed as

$$\underset{aa'}{S_{\alpha\alpha'}}(x|y) = \sum_{\boldsymbol{x}_1,\ldots,\boldsymbol{x}_n} \underset{ab_1}{G^{(f_1)}_{\alpha\beta_1}}(x|x_1) e^{-i\boldsymbol{x}_1\cdot\boldsymbol{p}_1}\Gamma^1 \underset{b_1 b_2}{G^{(f_2)}_{\beta_1\beta_2}}(x_1|x_2)\ldots e^{-i\boldsymbol{x}_n\cdot\boldsymbol{p}_n}\Gamma^n \underset{b_n a'}{G^{(f_n)}_{\beta_n\alpha'}}(x_n|y), \tag{5.58}$$

where the specific positions $x_1,\ldots,x_n$ correspond to the locations of the pions with respective momenta $\boldsymbol{p}_1,\ldots,\boldsymbol{p}_n$ and Gamma structure Γ^n. In this framework, the pions are fixed at a particular time t_n, but for the purpose of momentum projection, we perform a summation over the entire 3-dimensional lattice.

At times, propagators connecting the distinct pions create a loop that does not attach to the source or sink nucleons. Assuming S is the sequential propagator symbolizing the loop, the complete contraction of this loop can be achieved by employing a trace, resulting in

$$L = \sum_{\boldsymbol{x}_{n+1}} e^{i\boldsymbol{p}_{n+1}\cdot\boldsymbol{x}_{n+1}} \mathrm{tr}\left[S(x_{n+1}|x_{n+1})\Gamma^{n+1}\right], \tag{5.59}$$

which resembles a purely mesonic correlation function.

In our example, we obtain in total four different sequential propagators, which are

$$\underset{ac'}{S^1_{\alpha\gamma'}}(x|y;\boldsymbol{p}) = \sum_{\boldsymbol{z}} e^{i\boldsymbol{p}\cdot\boldsymbol{z}} \underset{ad'}{D_{\alpha\delta'}}(x|z)\delta_{d'd}\Gamma^{\pi^+}_{\delta'\delta} \underset{dc'}{U_{\delta\gamma'}}(z|y), \tag{5.60a}$$

$$\underset{ca'}{S^2_{\gamma\alpha'}}(x|y;\boldsymbol{q}) = \sum_{\boldsymbol{w}} e^{-i\boldsymbol{q}\cdot\boldsymbol{w}} \underset{ce'}{U_{\gamma\epsilon'}}(x|w)\delta_{e'e}\Gamma^{\pi^-}_{\epsilon'\epsilon} \underset{ea'}{D_{\epsilon\alpha'}}(w|y), \tag{5.60b}$$

$$\underset{aa'}{S^3_{\alpha\alpha'}}(x|y;\boldsymbol{p},\boldsymbol{q}) = \sum_{\boldsymbol{z},\boldsymbol{w}} e^{i\boldsymbol{p}\cdot\boldsymbol{z}} e^{-i\boldsymbol{q}\cdot\boldsymbol{w}} \underset{ad'}{D_{\alpha\delta'}}(x|z)\delta_{d'd}\Gamma^{\pi^+}_{\delta'\delta} \underset{de'}{U_{\delta\epsilon'}}(z|w)\delta_{e'e}\Gamma^{\pi^-}_{\epsilon'\epsilon} \underset{ea'}{D_{\epsilon\alpha'}}(w|y), \tag{5.60c}$$

$$\underset{cc'}{S^4_{\gamma\gamma'}}(x|y;\boldsymbol{p},\boldsymbol{q}) = \sum_{\boldsymbol{w},\boldsymbol{z}} e^{-i\boldsymbol{q}\cdot\boldsymbol{w}} e^{i\boldsymbol{p}\cdot\boldsymbol{z}} \underset{ce'}{U_{\gamma\epsilon'}}(x|w)\delta_{e'e}\Gamma^{\pi^-}_{\epsilon'\epsilon} \underset{ed'}{D_{\epsilon\delta'}}(w|z)\delta_{d'd}\Gamma^{\pi^+}_{\delta'\delta} \underset{dc'}{U_{\delta\gamma'}}(z|y), \tag{5.60d}$$

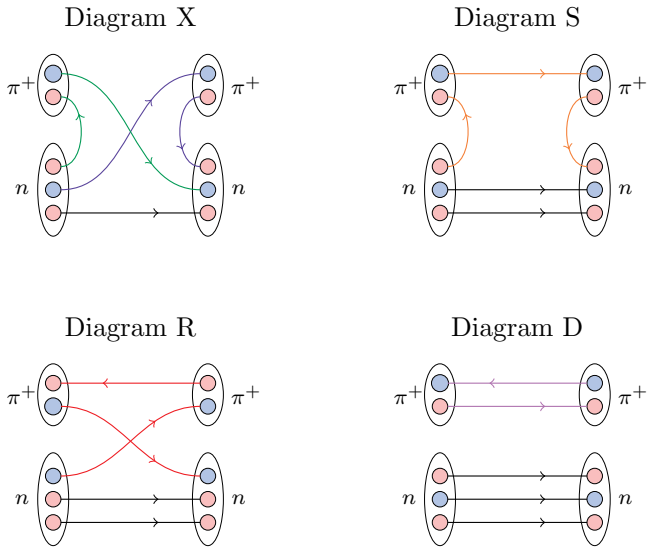

Figure 5.3.: Diagram topologies for the example correlation function $n\pi^+ \to n\pi^+$. The sequential propagator and mesonic loops are highlighted by colors.

and one mesonic loop of the form of a pion two-point function reading

$$L(\boldsymbol{p},\boldsymbol{q}) = \sum_{\boldsymbol{z},\boldsymbol{w}} e^{-i\boldsymbol{q}\cdot\boldsymbol{w}} e^{i\boldsymbol{p}\cdot\boldsymbol{z}} \mathrm{tr}\left[U(z|w)\Gamma^{\pi^-} D(w|z)\Gamma^{\pi^+}\right]. \tag{5.61}$$

By incorporating these sequential propagators and loops into the expression for the correlation function, we derive

$$\begin{aligned}
&\sum_{\boldsymbol{x},\boldsymbol{y}} e^{-i\boldsymbol{p}\cdot\boldsymbol{x}} e^{i\boldsymbol{q}\cdot\boldsymbol{y}} \varepsilon_{abc}\varepsilon_{a'b'c'} \Gamma^T_{\beta\gamma}\Gamma^S_{\beta'\gamma'} P^+_{\xi\alpha} (\gamma_3 P^+)_{\alpha'\rho} \\
&\times \Big(-S^1_{AC'} D_{BB'} S^2_{CA'} + S^3_{AA'} D_{BB'} U_{CC'} + S^1_{AC'} D_{BA'} S^2_{CB'} \\
&\quad - S^3_{AB'} D_{BA'} U_{CC'} + D_{AB'} S^1_{BC'} S^2_{CA'} - D_{AB'} S^3_{BA'} U_{CC'} \\
&\quad - D_{AB'} D_{BA'} S^4_{CC'} + D_{AB'} D_{BA'} U_{CC'} L - D_{AA'} S^1_{BC'} S^2_{CB'} \\
&\quad + D_{AA'} S^3_{BB'} U_{CC'} + D_{AA'} D_{BB'} S^4_{CC'} - D_{AA'} D_{BB'} U_{CC'} L \Big).
\end{aligned} \tag{5.62}$$

Fig. 5.3 illustrates all the topologies of the diagrams to which these contractions are associated, with the sequential propagator and mesonic loops marked by color.

5. Classify the contractions

Currently, all correlation functions integrate three sequential propagators linking x to y, along with an arbitrary number of meson loops. Consider a single diagram of this form:

$$C_i(t,\boldsymbol{p},\boldsymbol{q})_{\xi\rho} = \sigma \sum_{\boldsymbol{x},\boldsymbol{y}} e^{-i\boldsymbol{p}\cdot\boldsymbol{x}} e^{i\boldsymbol{q}\cdot\boldsymbol{y}} \varepsilon_{abc}\varepsilon_{a'b'c'} \Gamma^T_{\beta\gamma}\Gamma^S_{\beta'\gamma'} P^+_{\xi\alpha} (\gamma_t P^+)_{\alpha'\rho} \tag{5.63}$$

$$\times \langle \mathbf{A}_{A,i_A} \mathbf{B}_{B,i_B} \mathbf{C}_{C,i_C} \prod_i L_i \rangle_U, \tag{5.64}$$

Index pairs	**Diagram contribution** $\mathbb{X}$	
$(AA'),(BB'),(CC')$	$+\mathrm{tr}_c\{\mathrm{tr}_s[Q[\mathbf{B}\Gamma^S,\Gamma^T\mathbf{C}]]\mathbf{A}\}$	$+\mathbb{T}[\mathbf{B}\Gamma^S,\Gamma^T\mathbf{C},\mathbf{A}]$
$(AA'),(BC'),(CB')$	$-\mathrm{tr}_c\{\mathrm{tr}_s[Q[\mathbf{B},\Gamma^T\mathbf{C}\Gamma^S]]\mathbf{A}\}$	$-\mathbb{T}[\mathbf{B},\Gamma^T\mathbf{C}\Gamma^S,\mathbf{A}]$
$(AB'),(BA'),(CC')$	$-\mathrm{tr}_c\{Q[\mathbf{A}\Gamma^S,\Gamma^T\mathbf{C}]\mathbf{B}\}$	$-\mathbb{L}[\mathbf{A}\Gamma^S,\Gamma^T\mathbf{C},\mathbf{B}]$
$(AB'),(BC'),(CA')$	$+\mathrm{tr}_c\{Q[\mathbf{A}\Gamma^S,\mathbf{B}]\Gamma^T\mathbf{C}\}$	$+\mathbb{L}[\mathbf{A}\Gamma^S,\mathbf{B},\Gamma^T\mathbf{C}]$
$(AC'),(BB'),(CA')$	$-\mathrm{tr}_c\{Q[\mathbf{A},\mathbf{B}\Gamma^S]\Gamma^T\mathbf{C}\}$	$-\mathbb{L}[\mathbf{A},\mathbf{B}\Gamma^S,\Gamma^T\mathbf{C}]$
$(AC'),(BA'),(CB')$	$+\mathrm{tr}\{Q[\mathbf{A},\Gamma^T\mathbf{C}\Gamma^S]\mathbf{B}\}$	$+\mathbb{L}[\mathbf{A},\Gamma^T\mathbf{C}\Gamma^S,\mathbf{B}]$

Table 5.3.: List for classification of different diagram contributions depending on the index pairs of the corresponding propagators. The rightmost column shows the diagram contribution in terms of trace-full and trace-less contractions defined in Eq. 5.36 and Eq. 5.37. The diquark structure $Q[A,B]$ is defined in Eq. 2.112.

where $\mathbf{A}$ signifies the propagator associated with the first index A, and so on. The second indices remain variable, with $i_A, i_B, i_C \in \{A', B', C'\}$. The sign of the diagram is denoted by σ. The notation $\langle . \rangle_U$ implies averaging over the gauge fields, as each product of propagators continues to rely on the gauge field U. The product $\prod_i L_i$ indicates all mesonic loops.
Contracting the remaining color and spin indices results in structures similar to those of the nucleon two-point function in Eq. 2.110. Depending on the pair of indexes of the propagators, we obtain trace-full or trace-less contractions as defined in Eq. 5.36 and Eq. 5.37, respectively. In general, we obtain

$$C_i(t,\boldsymbol{p},\boldsymbol{q})_{\xi\rho} = \sigma \sum_{\boldsymbol{x},\boldsymbol{y}} e^{-i\boldsymbol{p}\cdot\boldsymbol{x}} e^{i\boldsymbol{q}\cdot\boldsymbol{y}} P^+_{\xi\alpha} \langle \mathbb{X}_{\alpha\alpha'} \prod_i L_i \rangle_U (\gamma_t P^+)_{\alpha'\rho}, \tag{5.65}$$

where $\mathbb{X}$ has one of the forms shown in Tab. 5.3.
For the example used throughout this section, we obtain the final form of the correlation function

$$\begin{aligned} C_{n\pi^+,n\pi^+}(t,\boldsymbol{p},\boldsymbol{q})_{\xi\rho} &= \sum_{\boldsymbol{x},\boldsymbol{y}} e^{-i\boldsymbol{p}\cdot\boldsymbol{x}} e^{i\boldsymbol{q}\cdot\boldsymbol{y}} P^+_{\xi\alpha} (\gamma_t P^+)_{\alpha'\rho} \\ \times \Big\langle \Big(& \mathbb{L}[S^1, D\Gamma^S, \Gamma^T S^2] + \mathbb{T}[D\Gamma^S, \Gamma^T U, S^3] + \mathbb{L}[S^1, \Gamma^T S^2 \Gamma^S, D] \\ & + \mathbb{L}[S^3\Gamma^S, \Gamma^T U, D] + \mathbb{L}[D\Gamma^S, S^1, \Gamma^T S^2] + \mathbb{L}[D\Gamma^S, \Gamma^T U, S^3] \\ & + \mathbb{L}[D\Gamma^S, \Gamma^T S^4, U] - \mathbb{L}[D\Gamma^S, \Gamma^T U, D]L + \mathbb{T}[S^0, \Gamma^T S^1 \Gamma^S, D] \\ & + \mathbb{T}[S^3\Gamma^S, \Gamma^T U, D] + \mathbb{T}[D\Gamma^S, \Gamma^T S^4, D] - \mathbb{T}[D\Gamma^S, \Gamma^T U, D]L \Big)_{\alpha\alpha'} \Big\rangle_U . \end{aligned} \tag{5.66}$$

6. Translate into distillation objects
The last step is to translate the contractions into products of distillation object, that is, elementals, peramulators, and momentum insertions.

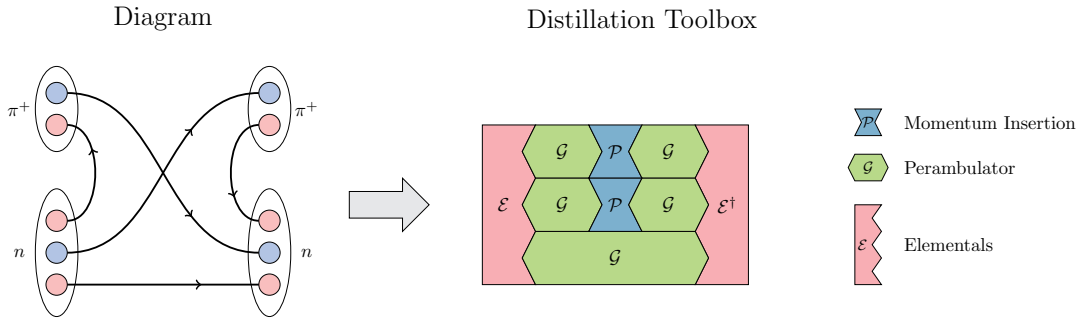

Figure 5.4.: Sketch of the distillation method being a toolbox for the calculation of correlation functions. The fundamental building blocks are elementals, momentum insertions and perambulator. The sketch shows diagram X as example of the channel $n\pi^+ \to n\pi^+$.

In Sec. 5.7, the translation of trace-full and trace-less contractions into the distillation framework has already been addressed (see Eq. 5.39 and Eq. 5.40). The last aspect to consider is the method for translating sequential propagators into a sequential perambulator. The general sequential propagator from Eq. 5.58 can be transformed using momentum insertions and perambulators into the sequential perambulator

$$\begin{aligned}\mathcal{S}^{nn'}_{\alpha\alpha'}(t_x, t_y) = &\left(\mathcal{G}^{(f_1)}\right)^{nm_1}_{\alpha\beta_1}(t_x, t_1)\mathcal{P}^{m_1m_2}(\boldsymbol{p}_1, t_1) \\ &\times \left(\mathcal{G}^{(f_2)}\right)^{m_1m_2}_{\beta_1\beta_2}(t_1, t_2)\ldots\left(\mathcal{G}^{(f_n)}\right)^{m_nn'}_{\beta_n\alpha'}(t_n, t_y),\end{aligned} \tag{5.67}$$

where the times t_i correspond to the space-time points x_i. The mesonic loop of Eq. 5.59 can be then transformed to

$$\mathcal{L} = \mathrm{tr}\left[\mathcal{S}(t', t')^{\ell\ell'}\mathcal{P}(t')^{\ell'\ell}\right]. \tag{5.68}$$

The translations provided in this section hold true only when the distillation quark smearing is applied to all quarks within the correlation function. When this condition is met, employing the distillation framework with precomputed distillation objects becomes extremely effective. A key advantage is the ability to compute general $N + \sum_i \pi \to N + \sum_j \pi_j$ correlation functions without performing any additional quark inversion. Typically, each correlation function of this type is reduced to tensor contractions involving distillation objects. The dimensions of these objects are as follows:

- $N_c \times N_c \times 4 \times 4$ for perambulators
- $N_c \times N_c$ for momentum insertions
- $N_c \times N_c \times N_c$ for modified elementals

based on the specified time positions of the operators. The relevant tensor projections for this thesis were all possible on single nodes with at most 32 GB of RAM used. In a

metaphorical sense, the distillation objects resemble bricks that can be used to build the correlation function from them, which is illustrated in Fig. 5.4.
Nevertheless, this line of reasoning overlooks the necessity of computing the distillation objects, which requires numerous quark inversions to obtain perambulators. Therefore, the decision whether employing the distillation framework is beneficial ultimately involves a trade-off analysis. For projects involving the calculation of numerous correlation functions of a similar nature, such as multi-hadronic correlation functions, as discussed in this thesis, distillation proves to be a promising approach.
In the end, the contractions derived using the automatic Wick contraction tools are tested against the Wick contraction code of GPT [103] for a significant subset of correlation functions. Unlike the automatic Wick contraction code discussed here, the GPT code does not offer the general functional form of the contractions but rather computes the individual contractions for specified propagators, matrix configurations, and positions.

5.9. Generalized Eigenvalue Problem (GEVP)

This thesis frequently employs the generalized eigenvalue problem (GEVP). Consequently, the following section provides a brief overview of GEVP within the context of lattice QCD. The usage of GEVP in Lattice QCD was initially introduced by the ALPHA Collaboration in 2009 [104]. The main idea is to use a set of operators $\mathcal{O}_i$ for $i = 1, \ldots, N$ to form the matrix of correlation functions with entries

$$C_{ij}(t, t_0) = \left\langle \mathcal{O}_i(t) \mathcal{O}_j^\dagger(t_0) \right\rangle, \quad \text{with } i, j = 1, \ldots, N. \tag{5.69}$$

In Ch. 7, the operators examined are pion-pion interpolating operators with different configurations of back-to-back momentum, together with a momentum zero rho operator. In the chapter dedicated to nucleon spectroscopy, namely Ch. 8, we use two separate groups of operators:

- for the positive parity sector, a nucleon operator, a nucleon-pion operator with back-to-back momentum, and nucleon-pion-pion operators are employed
- for the negative parity sector, we utilize a nucleon operator alongside two nucleon-pion operators: one with stationary particles and the other with back-to-back momentum.

The operator representation for the individual correlation function is expressed as a summation of functions decaying exponentially, which takes the form

$$C_{ij}(t) = \sum_n \langle 0|\mathcal{O}_i|n\rangle \langle n|\mathcal{O}_j^\dagger|0\rangle e^{-E_n t} \tag{5.70}$$

where E_n are the ascending energy levels of all states sharing identical quantum numbers. The matrix element $\langle 0|\mathcal{O}_i|n\rangle$ represents the overlap between the interpolating operator and the finite-volume state $|n\rangle$.
Solving the generalized eigenvalue problem

$$C(t) V_n(t, t_0) = \lambda_n(t, t_0) C(t_0) V_n(t, t_0), \tag{5.71}$$

for fixed t and t_0 yields the first N eigenenergies of the system using the eigenvalues $\lambda_n(t, t_0)$. Under the assumption that the system contains only N states, the eigenvalues have the form [104, 105]

$$\lambda_n(t, t_0) = e^{-E_n(t-t_0)}. \tag{5.72}$$

The eigenenergies are derived from the eigenvalues as expressed in

$$aE_{\text{eff},n}(t) = -\log\left(\frac{\lambda_n(t+a, t_0)}{\lambda_n(t, t_0)}\right) = aE_n. \tag{5.73}$$

Typically, more than N states are involved in the correlation functions. The contribution from excited states can be approximated by

$$aE_{\text{eff},n}(t) = aE_n + \alpha_n e^{-(E_{N+1}-E_n)t}, \tag{5.74}$$

assuming $t_0 \geq t/2$ and disregarding higher-order excited states [104]. In the analyzes, we typically choose a constant difference $\mathrm{d}t = t - t_0 = a$, therefore, for $t \geq 2a$ the assumed condition is fulfilled.
For sufficiently large t, the effective masses associated with the various GEVP modes converge to constant values. Similarly, the entries of the eigenvectors $V_{nm}(t, t_0)$ also reach constant values in this regime, thus allowing us to introduce a new optimized operator set via the basis transformation

$$\tilde{\mathcal{O}}_n = \sum_m V_{nm}(t, t_0)\mathcal{O}_m, \quad \text{for } t \gg a. \tag{5.75}$$

These operators $\tilde{\mathcal{O}}_n$ exhibit negligible overlap with eigenstates $m \neq n$, allowing the construction of correlation functions with reduced excited state contamination.

5.9.1. Normalization of eigenvectors

The matrix of eigenvectors V has two different directions to normalize. First, the eigenvectors $\alpha_n V_n$ also act as the eigenvectors of the GEVP. The second ambiguity comes from the fact that the rescaled operators $\mathcal{O}_i^r \equiv \beta_i \mathcal{O}_i$ encompass the same physical representation as $\mathcal{O}_i$, for any nonzero β_i. This invariance yields the rescaled optimized operator

$$\tilde{\mathcal{O}}_n^r = \sum_i V_{ni}\mathcal{O}_i^r = \sum_i \beta_i V_{ni}\mathcal{O}_i = \sum_i V_{ni}^r \mathcal{O}_i, \tag{5.76}$$

indicating that $\tilde{\mathcal{O}}_n$ can also be rescaled by adjusting V. When both types of rescaling for V are combined, we obtain

$$\bar{V}_{ij} = \alpha_i V_{ij} \beta_j, \tag{5.77}$$

where there is no implied summation over repeated indices.
The idea of our normalization scheme is to find α_i and β_j such that

$$\sum_i |\bar{V}_{ij}|^2 = 1 \quad \text{and} \quad \sum_j |\bar{V}_{ij}|^2 = 1. \tag{5.78}$$

To establish this, we can typically identify such matrices by initially defining the auxiliary matrix W whose elements are given by

$$W_{ij} = |V_{ij}|^2. \tag{5.79}$$

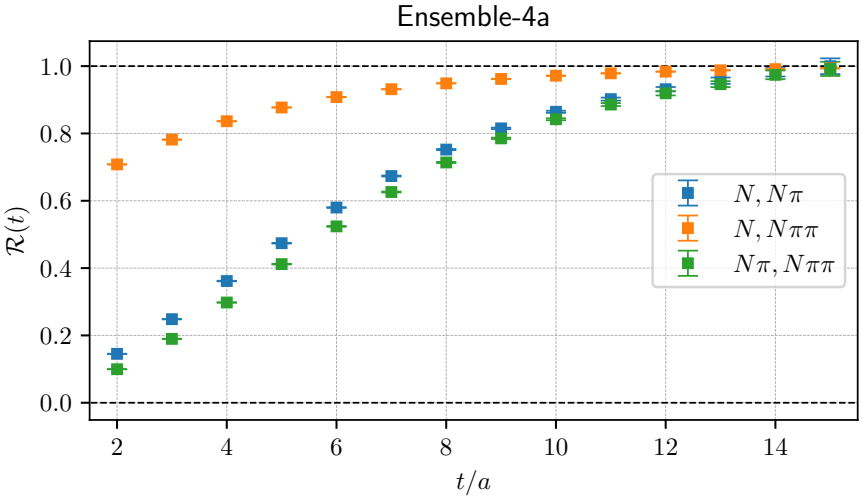

Figure 5.5.: Test for semi-definiteness of the GEVP in Sec. 8.1 for ensemble 4.

According to Sinkhorn's theorem [106], which states that for any square matrix W with strictly positive entries, there exist diagonal matrices D and E such that

$$\bar{W} \equiv DWE \tag{5.80}$$

is doubly stochastic, meaning that

$$\sum_i \bar{W}_{ij} = 1 \quad \text{and} \quad \sum_j \bar{W}_{ij} = 1. \tag{5.81}$$

Here, we consider D and E in the form

$$D = \mathrm{diag}(\alpha_0^2, \alpha_1^2, \ldots, \alpha_N^2) \quad \text{and} \quad E = \mathrm{diag}(\beta_0^2, \beta_1^2, \ldots, \beta_N^2). \tag{5.82}$$

The left-hand equation in Eq. 5.81 can then be reformulated as

$$1 = \sum_i \bar{W}_{ij} = \sum_{i,k,\ell} D_{ik} W_{k\ell} E_{\ell j} = \sum_i \alpha_i^2 W_{ij} \beta_j^2 \tag{5.83}$$

$$= \sum_i \alpha_i^2 |V_{ij}|^2 \beta_j^2 = \sum_i |\bar{V}_{ij}|^2, \tag{5.84}$$

thereby satisfying the first condition of Eq. 5.78. The second condition can be demonstrated in an analogous manner.
A simple algorithm we use to compute $\bar{V}$ is to alternatively normalize all rows and all columns of V, which is also called the Sinkhorn-Knopp algorithm [107].

5.9.2. Test Suite for GEVP

To assess the validity of the correlation function matrix employed in the GEVP, we utilized a particular test. The basic idea is to consider a general 2×2 matrix

$$C(t) = \begin{pmatrix} C_{00}(t) & C_{01}(t) \\ C_{10}(t) & C_{11}(t) \end{pmatrix}. \tag{5.85}$$

Given that the matrix must be Hermitian for all values of t, it is clear that $C_{00}(t)$ and $C_{11}(t)$ are positive, and $C_{01}(t)^* = C_{10}(t)$, which are themselves useful tests. The minimal eigenvalue of $C(t)$ is expressed as

$$\lambda(t) = \frac{1}{2}\left(C_{00}(t) + C_{11}(t) - \sqrt{(C_{00}(t) - C_{11}(t))^2 + 4C_{10}(t)C_{01}(t)}\right), \tag{5.86}$$

and by ensuring semi-definiteness, i.e., $\lambda(t) \geq 0$, we derive the condition

$$0 \leq \mathcal{R}_{01}(t) = \frac{C_{01}(t)C_{10}(t)}{C_{00}(t)C_{11}(t)} \leq 1. \tag{5.87}$$

In addition, as t becomes large, when the correlation functions are mainly influenced by the ground state, the ratio $\mathcal{R}$ approaches 1.
For general $N \times N$ correlation matrices, this test can be repeated for every pair of indices (i, j) with $i, j = 1, \ldots, N$ and $i < j$.
Fig. 5.5 illustrates the ratios for all positive parity operator combinations considered in Sec. 8.1, specifically a nucleon operator N, a nucleon-pion back-to-back operator $N\pi$, and a nucleon-pion-pion operator $N\pi\pi$. It is observed that all the ratios tend towards 1 as t increases. In addition, a steady increase is noticed, though it is in general not strictly necessary.

6. Omega Spectroscopy

The objective of this chapter is to identify the spectrum of projected and non-projected operators associated with the Ω-baryon. At first glance, the omega baryon, which consists only of strange quarks, appears to be unrelated to the nucleon spectrum and neutrino-nucleon scattering. However, due to the heavier strange quark mass, the inversions of the Dirac operator are less computationally expensive and the omega baryon has in general a better signal-to-noise ratio [108]. Therefore, the omega mass is commonly used to set the scale of the ensembles [109–111], which indirectly also affects the results of the nucleon spectrum analyses. Furthermore, because of its advantages properties, the omega baryon is a useful testing ground for developing new methods in the context of baryon physics.
Ref. [109] employs omega interpolating operators that have a non-zero overlap with states that transform within the irreducible representations H and G_1 of the octahedral group. The Ω-baryon has a spin of $J = \frac{3}{2}$, which is subduced into H (see Sec. 3.1). Consequently, a correctly projected operator for the Ω-baryon overlaps only with H, necessitating the projection of the operator applied in [109]. In this context, we will examine whether there is a shift in the ground and first excited states of the spectrum when using both the operator from [109] and a projected version. All calculations in this chapter are performed on ensemble 4 with the same number of configurations stated in Tab. 5.1.
Beginning with the non-projected operator as outlined in [109], we employ the interpolating operator

$$\mathcal{O}_\Omega(x)_{\alpha,i} = \varepsilon_{abc}(P_+ s_a(x))_\alpha \left[s_b(x)^T C\gamma_i s_c(x) \right], \tag{6.1}$$

which maintains a form analogous to Eq. 3.47, yet now incorporates an additional free index i, establishing the diquark's vector structure. As a result of this additional vector structure, we see that the operator transforms within the representation $G_1 \otimes T_1 \simeq G_1 \oplus H$. The operator from Eq. 6.1 is utilized for calculating the correlation function:

$$C_{\Omega\Omega,\mathrm{np}}(t_x, t_y) = \sum_{\alpha,i} \sum_{\boldsymbol{x},\boldsymbol{y}} \langle \mathcal{O}_\Omega(x)_{\alpha,i} \mathcal{O}^\dagger_\Omega(y)_{\alpha,i} \rangle. \tag{6.2}$$

The contraction of Eq. 6.2 results in:

$$C_{\Omega\Omega,\mathrm{np}}(t_x, t_y) = -2 \sum_i \sum_{\boldsymbol{x},\boldsymbol{y}} \left\langle \mathrm{tr}_s \left[P_+ \mathrm{tr}_c \left[\mathrm{tr}_s \left[Q_i^{\Omega\Omega}(x|y) \right] S(x|y) + 2 Q_i^{\Omega\Omega}(x|y) S(x|y) \right] \right] \right\rangle, \tag{6.3}$$

where $S(x|y)$ is the strange quark propagator and the diquark structure is defined as

$$Q_i^{\Omega\Omega}(x|y)_{\substack{\alpha\beta \\ a'a}} = \sum_{\gamma,b,c,b',c'} \varepsilon_{abc}\varepsilon_{a'b'c'} \left[S(x|y)\gamma_i C \right]_{\substack{\alpha\gamma \\ bb'}} \left[C\gamma_i S(x|y) \right]_{\substack{\beta\gamma \\ cc'}}. \tag{6.4}$$

In this study, we evaluate the correlation function using wall and box sources, with each box having a size of 6 sites (refer to Sec. 2.8), and point sinks. We further apply Coulomb gauge-fixing to enhance the signal of the correlation function (see Sec. 2.9). To improve the

Λ	k	J	J_z	$\Omega^{(DP)}_{\mu_1,\mu_2,\mu_2}$	Λ	k	J	J_z	$\Omega^{(DP)}_{\mu_1,\mu_2,\mu_2}$
G_{1g}		$\frac{1}{2}$	$+\frac{1}{2}$	$\Omega_{023} - \Omega_{122}$	G_{1u}		$\frac{1}{2}$	$+\frac{1}{2}$	$\Omega_{003} - \Omega_{012}$
G_{1g}		$\frac{1}{2}$	$-\frac{1}{2}$	$\Omega_{033} - \Omega_{123}$	G_{1u}		$\frac{1}{2}$	$-\frac{1}{2}$	$\Omega_{013} - \Omega_{112}$
H_g	1	$\frac{3}{2}$	$+\frac{3}{2}$	Ω_{000}	H_u	1	$\frac{3}{2}$	$+\frac{3}{2}$	$\sqrt{3}\,\Omega_{002}$
H_g	1	$\frac{3}{2}$	$+\frac{1}{2}$	$\sqrt{3}\,\Omega_{001}$	H_u	1	$\frac{3}{2}$	$+\frac{1}{2}$	$\Omega_{003} + 2\,\Omega_{012}$
H_g	1	$\frac{3}{2}$	$-\frac{1}{2}$	$\sqrt{3}\,\Omega_{011}$	H_u	1	$\frac{3}{2}$	$-\frac{1}{2}$	$2\,\Omega_{013} + \Omega_{112}$
H_g	1	$\frac{3}{2}$	$-\frac{3}{2}$	Ω_{111}	H_u	1	$\frac{3}{2}$	$-\frac{3}{2}$	$\sqrt{3}\,\Omega_{113}$
H_g	2	$\frac{3}{2}$	$+\frac{3}{2}$	Ω_{022}	H_u	2	$\frac{3}{2}$	$+\frac{3}{2}$	Ω_{222}
H_g	2	$\frac{3}{2}$	$+\frac{1}{2}$	$2\,\Omega_{023} + \Omega_{122}$	H_u	2	$\frac{3}{2}$	$+\frac{1}{2}$	$\sqrt{3}\,\Omega_{223}$
H_g	2	$\frac{3}{2}$	$-\frac{1}{2}$	$\Omega_{033} + 2\,\Omega_{123}$	H_u	2	$\frac{3}{2}$	$-\frac{1}{2}$	$\sqrt{3}\,\Omega_{233}$
H_g	2	$\frac{3}{2}$	$-\frac{3}{2}$	$\sqrt{3}\,\Omega_{133}$	H_u	2	$\frac{3}{2}$	$-\frac{3}{2}$	Ω_{333}

Table 6.1.: Projected Ω operators in the Dirac-Pauli representation. The operator are derived in [112].

statistics of the box sources, stochastic $\mathbb{Z}_3$ sources [113] with three hits are utilized. This approach involves dividing the three-dimensional sublattice into uniform boxes of size 6, followed by the multiplication of a random variable $\eta \in \{1, \frac{1+\sqrt{3}\,i}{2}, \frac{1-\sqrt{3}\,i}{2}\}$ to each box. As stated in [113], this strategy can enhance statistical accuracy while maintaining the same computational expense as employing a single box per source. Observing this improvement, we adopt gauge-fixed $\mathbb{Z}_3$ box sources for our analysis. The correlation function with the wall source is denoted by `npWP`, while the one with the box source is labeled as `npBP`.
The energies of the ground state and the first excited state are determined through a correlated constrained fit applied simultaneously to the effective mass from both correlation functions. The constrained fit process works as follows:

1. We calculate the effective mass for `npWP` and `npBP` as follows:

$$am_{\text{eff}}(t) = -\log\left(\frac{C(t+a)}{C(t)}\right). \tag{6.5}$$

2. Both effective mass curves are fitted simultaneously using the model function:

$$f(t, m, E, A) = m + A\,e^{-(E-m)t}, \tag{6.6}$$

where the parameters m and E are constrained to be the same for both curves. The resulting fit provides the parameter set as

$$\beta = (m, E, A_{\texttt{npWP}}, A_{\texttt{npBP}}). \tag{6.7}$$

The first line of Tab. 6.2 presents the fitting outcomes, with the selection of fit ranges based on a comparison of several possibilities, ultimately choosing one that meets the criteria for an optimal fit as described in Sec. 5.5. In the top illustration of Fig. 6.1, the effective masses of `npWP` and `npBP` are depicted by data points in their respective colors. The model prediction, achieved from the constrained fit, is represented by the colored band and is based on the filled data points.

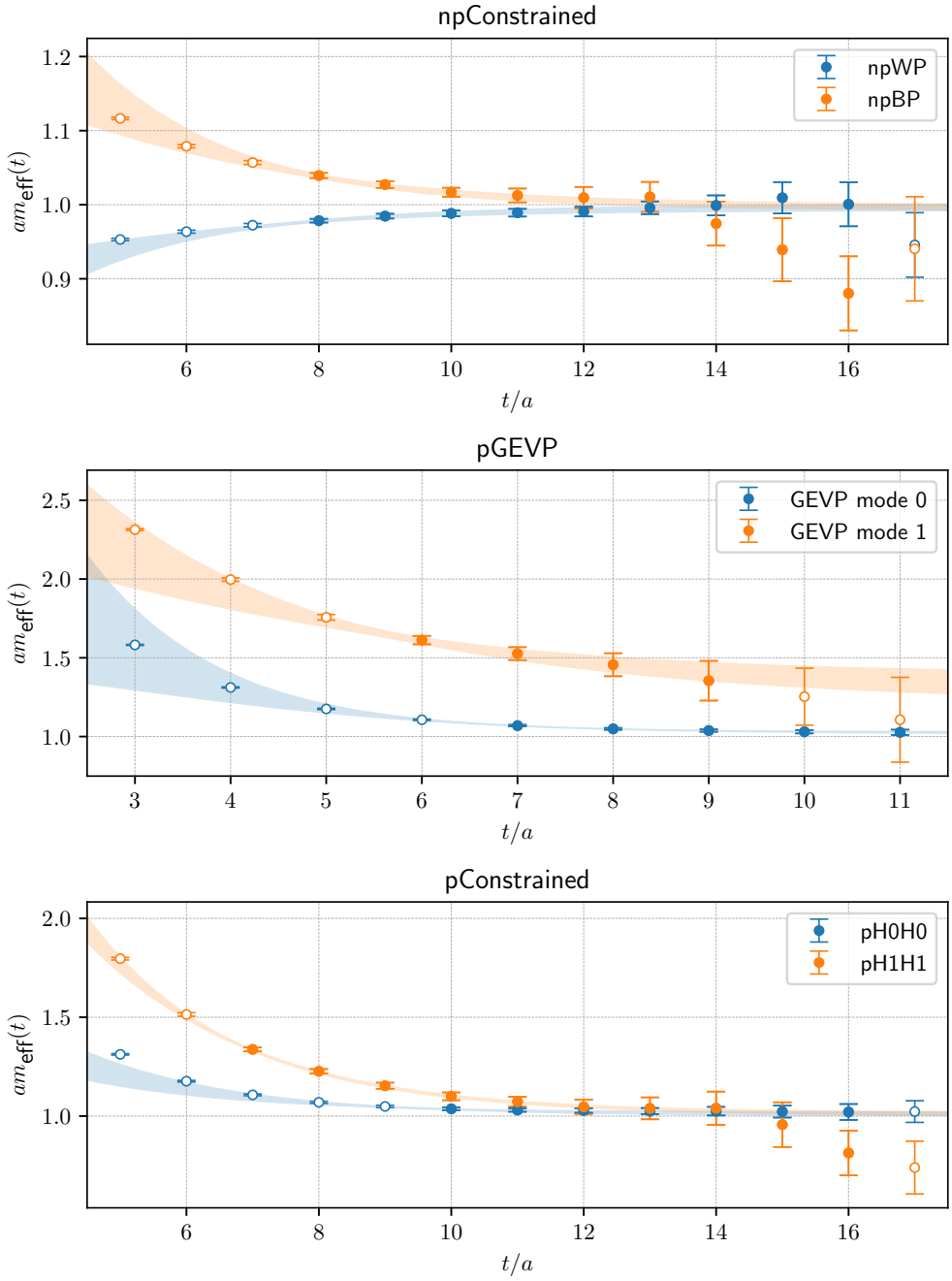

Figure 6.1.: Effective mass plots used in the individual constrained fits. The colored bands indicate the model predictions resulting from correlated constrained fits to the filled data points, which are shown in matching colors.

Constrained tag	Tags		Fit ranges		am_Ω	$am_{\Omega'}$	p-value
npConstrained	npWP	npBP	$(8, 16)$	$(8, 16)$	0.9963(49)	1.380(83)	0.84
pGEVP	GEVP0	GEVP1	$(7, 12)$	$(6, 9)$	1.024(12)	1.30(11)	0.98
pCombined	pH0H0	pH1H1	$(10, 16)$	$(7, 16)$	1.011(13)	1.437(44)	0.92

Table 6.2.: Fit results from the various constrained fits performed in this analysis. Fit ranges are determined by systematically testing multiple intervals and selecting those that meet the criteria described in Sec. 5.5. The overlap factors A are omitted, as they are not relevant for the spectral analysis.

In alignment with [112], we use the projected operator expressed as

$$\Omega^{(DP)}_{\alpha\beta\gamma}(x) = \varepsilon_{abc} s^{(DP)}_{\alpha,a}(x) s^{(DP)}_{\beta,b}(x) s^{(DP)}_{\gamma,c}(x), \tag{6.8}$$

which is defined in the Dirac-Pauli representation (further details can be found in Sec. A.2). It is important to note that the operator indicated in Eq. 6.8 has not yet been projected. The specific projections onto the irreducible representations of the octahedral group are shown in Tab. 6.1. The operator in Eq. 6.8 can brought to DeGrand-Rossi representation, which is the default basis throughout this thesis, by applying the unitary transformation

$$\psi_{\alpha,a} \to \psi'_{\alpha,a} = U_{\alpha\beta}\psi_{\beta,b} \quad \text{and} \quad \bar{\psi}_{a,\alpha} \to \bar{\psi}'_{\alpha,a} = \bar{\psi}_{\beta,a} U^\dagger_{\beta\alpha}, \tag{6.9}$$

with the transformation matrix

$$U = \frac{\gamma_1 \left(\mathbb{1} + \gamma_5\gamma_t\right)}{\sqrt{2}} \tag{6.10}$$

on the individual fermions in Eq. 6.8. For the projected operators shown as shown in Tab. 6.1 we observe that two distinct embeddings of the irreducible representation H_g exist. This implies that there are two orthogonal sets of operators corresponding to the irreducible representation H_g and $J_z = +\frac{3}{2}, +\frac{1}{2}, -\frac{1}{2}, -\frac{3}{2}$. These operators enable us to perform a GEVP analysis using the correlator matrix

$$C_{\Omega\Omega,\mathbf{p},i,j}(t_x, t_y) = \sum_{\boldsymbol{x},\boldsymbol{y}} \sum_{J_z=-\frac{3}{2},-\frac{1}{2},\frac{1}{2},\frac{3}{2}} \left\langle \Omega_{H_g,J_z,i}(x) \Omega^\dagger_{H_g,J_z,j}(y) \right\rangle, \tag{6.11}$$

where $\Omega_{H_g,J_z,i}$ refers to the projected operator as detailed in Tab. 6.1 with respect to the irreducible representation H_g, the spin z-component J_z, and the embedding i. In the generalized eigenvalue problem (GEVP), we set a fixed distance $t - t_0 = a$, allowing us to estimate the effective masses of various modes using

$$aE_{\text{eff},j}(t) \approx aE_j + A_j e^{-(E_N - E_j)t}, \tag{6.12}$$

where N indicates the number of modes in the GEVP, which is $N = 2$ in this study. The second row of Fig. 6.1 presents the curves for both effective masses, similar to those seen in the non-projected constrained fitting scenario. We apply a constrained fit approach for both effective masses, with only one shared parameter, E_N. The chosen fitting ranges are determined according to the criteria specified in Sec. 5.5. For consistency, we also perform

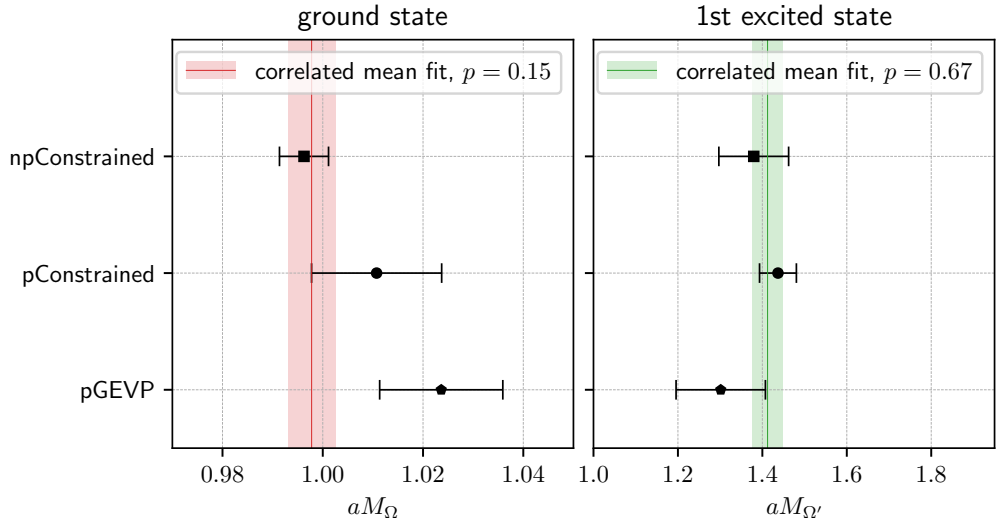

Figure 6.2.: Comparison of the mass estimates obtained from different analysis approaches. The colored band represents the result from the constant correlated fit.

a constrained fit of the correlation functions $C_{\Omega\Omega,\mathrm{p},i,i}$ for $i = 0, 1$. These are depicted in the lower row of Fig. 6.1, denoted `pH0H0` for $i = 0$ and `pH1H1` for $i = 1$.
The mass estimates from both fits are detailed in Tab. 6.2, together with the fit ranges and corresponding p-values. A summary of the ground state and excited state mass estimates using three different approaches is depicted in Fig. 6.2. To analyze the consistency of these approaches, a correlated fit is performed on all data points. In terms of the first excited state, all energy estimates are consistent with each other and align well with the average. For the ground state, some discrepancies are observed, particularly between the non-projected constrained fit (`npConstrained`) and the projected GEVP fit (`pGEVP`). However, the p-value for the constant fit across all data points does not suggest any significant tensions.

7. Two-Pion and Rho Meson Spectroscopy

This chapter explains the second project of this thesis, focusing on a spectroscopy study of the ρ-meson and two-pion states sharing identical quantum numbers. The ρ-meson possesses spin $J = 1$, negative parity, and isospin $I = 1$. In this chapter, we will consistently employ two-pion states characterized by these quantum numbers.

This research is undertaken in the context of evaluating the long-distance window contribution of the hadronic vacuum polarization (HVP) to the muon's anomalous magnetic moment, $g-2$ [4]. Typically, the leading order HVP contribution within the time-momentum representation is calculated as

$$a_\mu^{\text{HVP LO}} = \sum_{t=0}^{\infty} w_t C(t), \tag{7.1}$$

where the weights incorporate the effects of the photon and muon [114], though they are not relevant to the following spectroscopy analysis. The correlation function $C(t)$ is expressed as

$$C(t) = \frac{1}{3} \sum_{\boldsymbol{x}} \sum_{j=0,1,2} \langle J_j(\boldsymbol{x}, t) J_j(0) \rangle \,, \tag{7.2}$$

with the vector current defined as

$$J_j(x) = i \sum_f Q_f \bar{\Psi}_f(x) \gamma_j \Psi_f(x). \tag{7.3}$$

As outlined in Ch. 2, the correlation function can be expressed through its spectral representation

$$C(t) = \frac{1}{3} \sum_{j=0,1,2} \sum_n |\langle n | \hat{J}_j | 0 \rangle|^2 e^{-E_n t}, \tag{7.4}$$

where $\hat{J}_j$ represents the zero-momentum vector operator, and $|n\rangle$ and E_n are the Hamiltonian's eigenstates and eigenenergies, respectively. Specifically, we obtain energies E_n for states characterized by spin $J = 1$, isospin $I = 1$, and negative parity.

In the study of the muon's anomalous magnetic moment, the HVP contribution is generally divided into three distinct window contributions, the short-distance, intermediate, and long-distance windows. These are mathematically expressed as follows:

$$a_\mu^{\text{HVP LO}} = a_\mu^{\text{SD}} + a_\mu^{W} + a_\mu^{LD}, \tag{7.5}$$

where the contributions are given by:

$$a_\mu^{SD}(t_0, \Delta) = \sum_{t=0}^{\infty} C(t) w_t [1 - \Theta(t, t_0, \Delta)], \tag{7.6a}$$

$$a_\mu^{W}(t_0, t_1, \Delta) = \sum_{t=0}^{\infty} C(t) w_t [\Theta(t, t_0, \Delta) - \Theta(t, t_1, \Delta)], \tag{7.6b}$$

$$a_\mu^{LD}(t_1, \Delta) = \sum_{t=0}^{\infty} C(t) w_t \Theta(t, t_1, \Delta), \tag{7.6c}$$

with $\Theta(t, t', \Delta) = \frac{1}{2}(1 + \tanh[(t - t')/\Delta])$. In this case, the parameters are chosen as $t_0 = 0.4$ fm, $t_1 = 1.0$ fm, and $\Delta = 0.15$ fm. In particular, the long-distance window focuses on correlation functions at extended times. However, typically at these times the signal is often significantly affected by noise, as explained by Lepage's argument (refer to Sec. 2.11). A strategy to avoid this problem involves evaluating the overlap factors $|\langle n|\hat{J}_j|0\rangle|^2$ and determining the energies E_n. These parameters can then be utilized to reconstruct the correlation functions via

$$C^N(t) = \sum_{n=1}^{N} |\langle n|\hat{J}_j|0\rangle|^2 e^{-E_n t}, \tag{7.7}$$

where N denotes the number of states incorporated in the reconstruction. At large Euclidean time t and sufficiently large N, we achieve $C^N(t) = C(t)$ while remaining within statistical uncertainties.

This prompts the subsequent spectral analysis of the ρ-spectrum, paying particular attention to two-pion states. This analysis is performed in all the ensembles listed in the lower section of Tab. 5.1, specifically ensembles C, 48I, 64I, and 96I. In the subsequent discussion, only ensemble C is presented, as it exemplifies all characteristics discovered in the analyses.

The study involves a GEVP analysis using a set of operators that includes a ρ interpolating operator and several two-pion operators with back-to-back momentum, as detailed in Sec. 3.4. To briefly recap, the ρ interpolating operator is given by

$$\mathcal{O}_{\rho_\mu}(\mathbf{0}, t) = \sum_{\boldsymbol{x}} \bar{\psi}_i(\boldsymbol{x}, t) \gamma_\mu \psi_j(\boldsymbol{x}, t), \qquad \text{with } \mu = x, y, z, \tag{7.8}$$

where the indices i and j are chosen to obtain the relevant isospin states. Concerning the two-pion states, these are described by

$$\mathcal{O}_{\pi_1\pi_2}(t; \boldsymbol{p}) = \mathcal{O}_{\pi_1}(\boldsymbol{p}, t)\mathcal{O}_{\pi_2}(-\boldsymbol{p}, t), \tag{7.9}$$

where the structure of the pion operators $\mathcal{O}_{\pi_i}$ is similar to that in Eq. 7.8, but γ_μ is replaced with γ_5. The isospin projections of the two-pion states are depicted in Eq. 3.21. Each operator is smeared by distillation (refer to Sec. 5.7). For ensembles 48I and 64I, we employ momentum configurations $\mathbf{1}, \mathbf{2}, \mathbf{3}, \mathbf{4}$, while for ensembles C and 96I, we also include $\mathbf{5}, \mathbf{6}, \mathbf{8}$. In Tab. 7.1, the direct sums of irreducible representations (irreps) of the full cubic group, corresponding to the vector space spanned by the two-pion operators with an explicit momentum configuration, are illustrated. For the momentum configurations **5** and

momentum signature		irrep composition of $\pi\pi$ states
1	(0,0,1)	$A_{1g} \oplus E_g \oplus T_{1u}$
2	(0,1,1)	$A_{1g} \oplus E_g \oplus T_{1u} \oplus T_{2g} \oplus T_{2u}$
3	(1,1,1)	$A_{1g} \oplus A_{2u} \oplus T_{1u} \oplus T_{2g}$
4	(0,0,2)	$A_{1g} \oplus E_g \oplus T_{1u}$
5	(0,1,2)	$A_{1g} \oplus A_{2g} \oplus 2E_g \oplus T_{1g} \oplus 2T_{1u} \oplus T_{2g} \oplus 2T_{2u}$
6	(1,1,2)	$A_{1g} \oplus A_{2u} \oplus E_g \oplus E_u \oplus 2T_{1u} \oplus 2T_{2g} \oplus T_{2u}$
8	(0,2,2)	$A_{1g} \oplus E_g \oplus T_{1u} \oplus T_{2g} \oplus T_{2u}$

Table 7.1.: Direct sum of irreducible representations of the full cubic group associated with two-pion operators carrying back-to-back momentum. A detailed discussion is provided in Ch. 3.

6, we observe that the irreducible representation T_{1u} appears twice in the vector space. Consequently, two variations of projected operators can be defined. Fig. 7.1 provides a visualization of the linear combinations of the T_{1u}-projected operators in various momentum configurations. The basis set differs by momentum configuration and is derived through repeated application of group elements on the momentum signature. However, they are structured such that operators at even indices are paired with their parity flipped counterparts, that is, the operator at the $2n$-th position, $\mathcal{O}_{\pi_1}(\boldsymbol{q},t)\mathcal{O}_{\pi_2}(-\boldsymbol{q},t)$, is succeeded by $\mathcal{O}_{\pi_1}(-\boldsymbol{q},t)\mathcal{O}_{\pi_2}(\boldsymbol{q},t)$ at the $(2n+1)$-th position. An observation depict in Tab. 7.1 is that we have typically operator combinations of the type

$$\mathcal{O}_{\pi_1}(\boldsymbol{p},t)\mathcal{O}_{\pi_2}(-\boldsymbol{p},t) - \mathcal{O}_{\pi_1}(-\boldsymbol{p},t)\mathcal{O}_{\pi_2}(\boldsymbol{p},t), \tag{7.10}$$

which ensures the negative parity of the state.
In the subsequent discussion, the smeared rho operator is denoted as `rho`, and the various two-pion operators are marked as `2pi.q`, where q denotes the momentum configuration. In cases where there are two versions of the operator, we distinguish between them by using `2pi.q.v1` and `2pi.q.v2`. We perform a GEVP analysis (see Sec. 5.9 for additional information) using the stated operators, with a fixed time difference $\Delta t = a$. The effective energies for each GEVP mode are illustrated in Fig. 7.2. The black-dashed lines represent the energies of the non-interacting pion pairs, computed as

$$E_{\pi\pi}(\boldsymbol{p}) = 2\sqrt{m_\pi^2 + \boldsymbol{p}^2}, \tag{7.11}$$

associated with various momentum configurations. In addition, the red dashed line marks the 770 MeV energy level, which approximates the energy of the ρ-meson. For momentum configurations with only one version of the operator, including the ρ-meson energy, plateaus of the effective energy curves are observed near the non-interacting energy levels. Some modes exhibit energies below, and others above, the non-interacting energy, suggesting attractive and repulsive interactions, respectively. Close to the states, where there are two distinct forms of operators, an extra state emerges above what is anticipated from the non-interacting states.
Fig. 7.3 presents the normalized eigenvectors for all GEVP modes at $t = 6a$. These eigenvectors are normalized as described in Sec. 5.9.1. Each bar indicates the overlap of the respective GEVP mode with the operators within the GEVP basis. The dominant

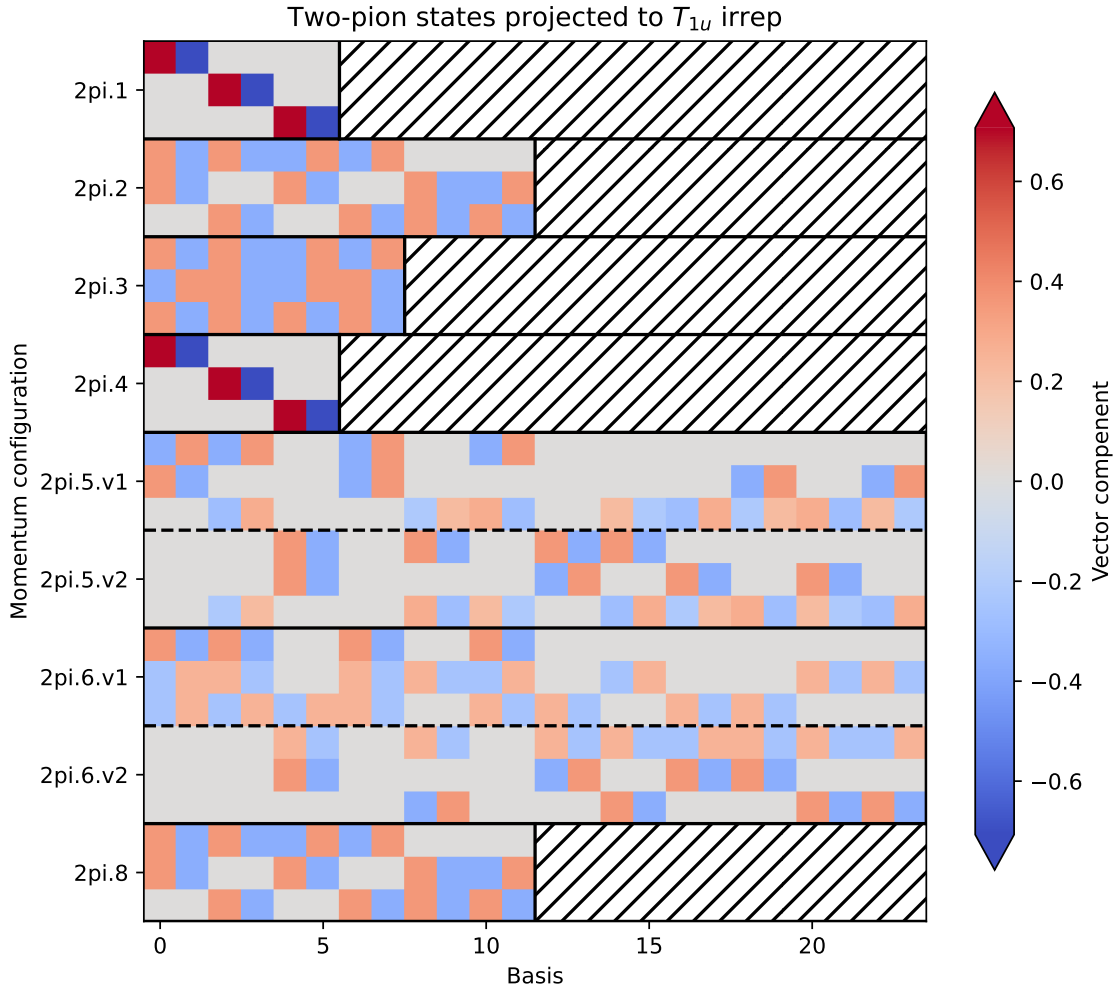

Figure 7.1.: Representations of the T_{1u}-projected operators across different momentum configurations.

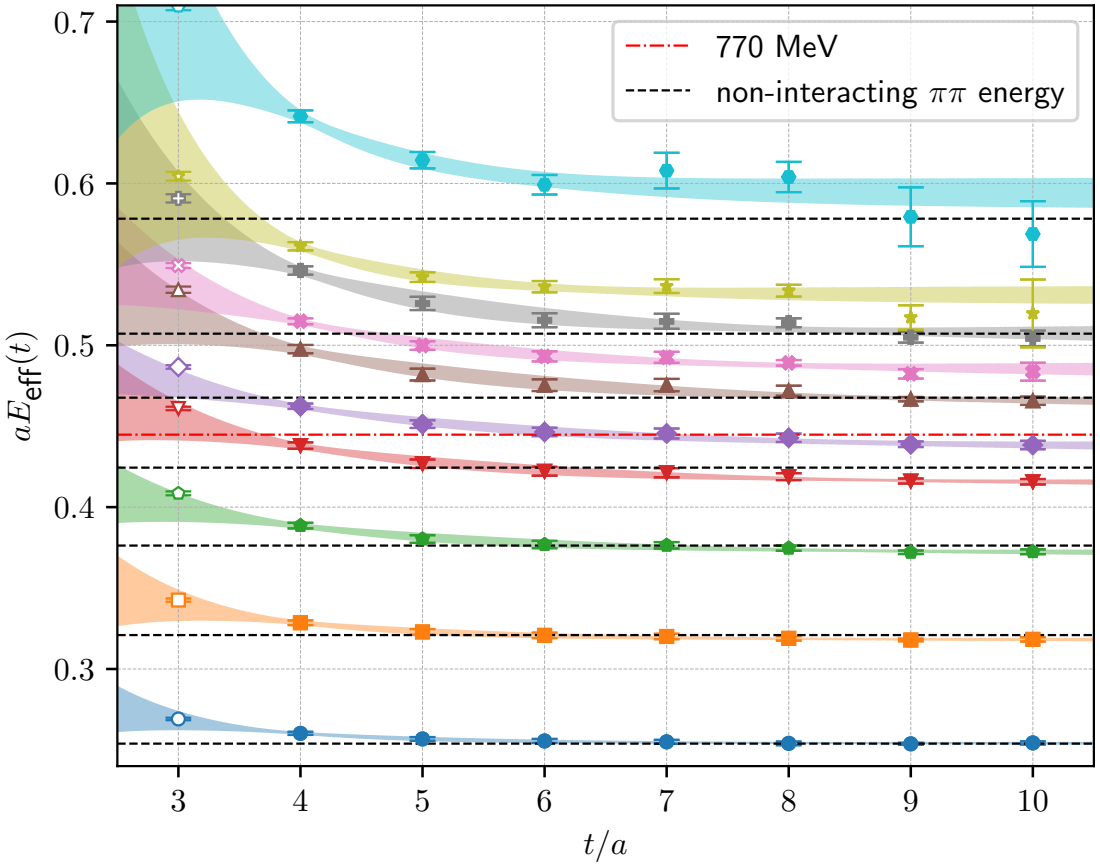

Figure 7.2.: Effective mass plots for the GEVP eigenstates for ensemble C. The colored bands, corresponding to the colors of the data points, depict the outcomes of excited state fits using the model $f(t, m, A, E) = m + Ae^{-(E-m)t}$, which incorporates all filled data points. The dashed lines indicate the non-interacting energy level of back-to-back pions, whereas the red dot-dashed line denotes 770 MeV, which is roughly the ρ meson mass in the continuum.

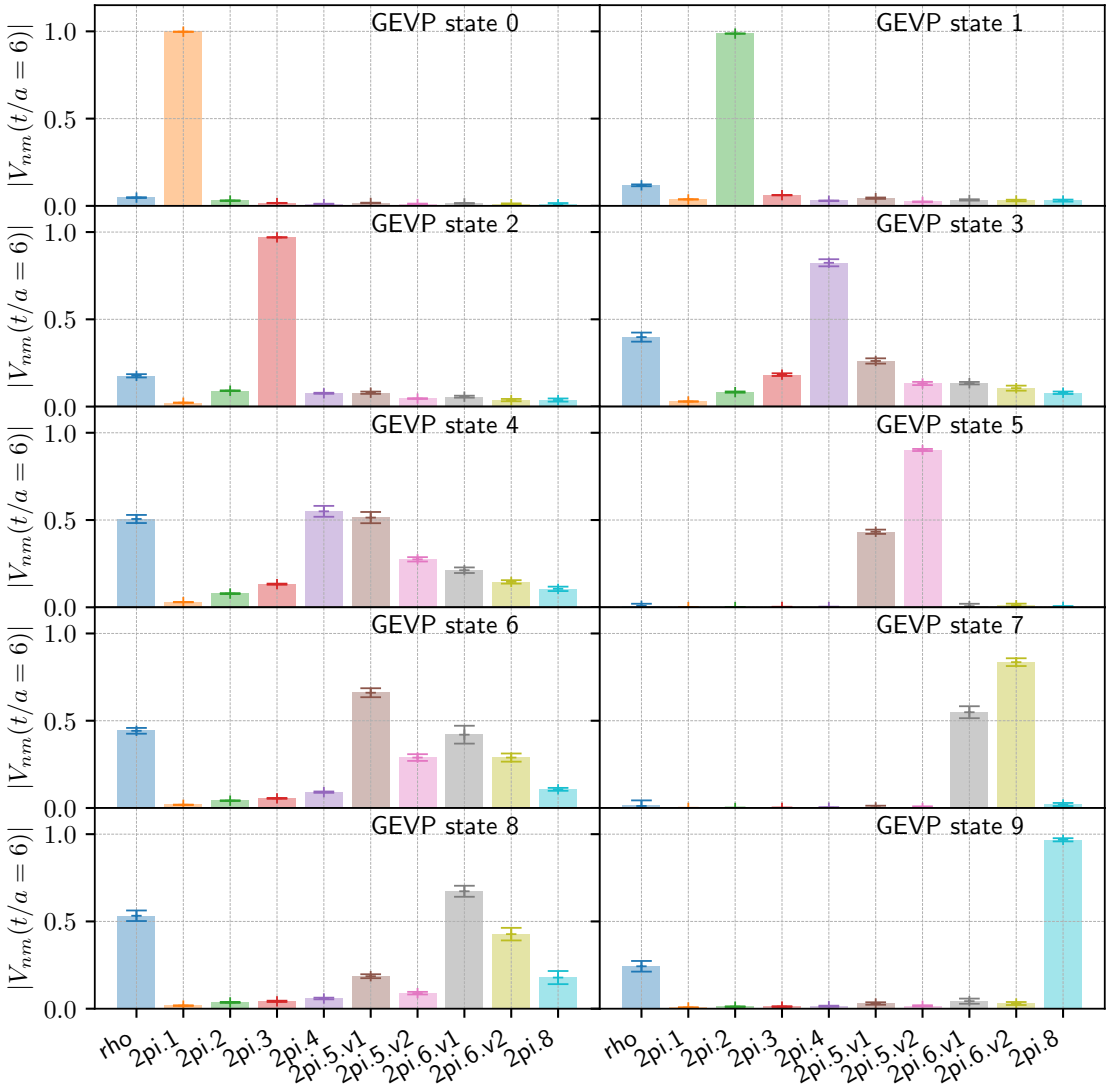

Figure 7.3.: Eigenvectors from the GEVP at $t/a = 6$ for ensemble C, which are normalized in accordance with Sec. 5.9.1.

	48I	64I	96I	C
aE_0	0.3025(13)	0.22369(39)	0.16231(90)	0.25413(95)
aE_1	0.38927(95)	0.28737(83)	0.20640(82)	0.3181(14)
aE_2	0.4548(38)	0.3364(18)	0.24303(84)	0.3716(31)
aE_3	0.4961(58)	0.3776(22)	0.2705(19)	0.4147(32)
aE_4	0.544(15)	0.4229(42)	0.2869(21)	0.4367(49)
aE_5	—	—	0.3082(27)	0.4642(58)
aE_6	—	—	0.3193(20)	0.4845(65)
aE_7	—	—	0.3354(29)	0.5066(79)
aE_8	—	—	0.3488(63)	0.5309(58)
aE_9	—	—	0.389(11)	0.5940(96)

Table 7.2.: Energy estimates of the individual GEVP modes obtained from excited-state fits using the model $f(t, m, A, E) = m + Ae^{-(E-m)t}$, shown for the ensembles listed in the lower part of Tab. 5.1.

operator aligns with expectations based on the plateau of the corresponding effective energy curve.
The energies of the distinct GEVP modes are determined using excited state fits on the effective energy, utilizing the model

$$f(t, A, m, E) = m + Ae^{-(E-m)t}, \tag{7.12}$$

where, unlike in Ch. 6, no constrained fit is applied. The fit intervals are selected to meet the criteria outlined in Sec. 5.5. Given the limited number of independent configurations, the fits are executed without correlation.
Tab. 7.2 presents the energy estimates for the various ensembles. These estimates, together with the overlap factors shown in, for instance, Fig. 7.3, are utilized to reconstruct the correlation function $C^N(t)$, as detailed in [4].

8. Nucleon-Pion and Nucleon-Pion-Pion Spectroscopy with Distillation

This chapter provides a description of the findings described in [5]. The study involves the calculation of the nucleon spectrum in both the positive and negative parity sectors, with particular attention to the $N\pi$ and $N\pi\pi$ states. Additionally, in the positive-parity sector, we conduct an extrapolation of the nucleon mass to the physical point. This chapter presents the main results of this thesis.
Analyses of the GEVP are performed using a fixed temporal separation $\Delta t = a$, enabling the fitting of excited states with the function

$$f(t, m, E, A) = m + Ae^{-(E-m)t}, \tag{8.1}$$

where m represents the mass of the state, E the excited state's energy, and A is an overlap factor.

8.1. Positive Parity Sector

8.1.1. Individual Ensemble GEVP

In the positive parity sector, a 3×3 generalized eigenvalue problem (GEVP) is constructed using the nucleon interpolating operator (Eq. 2.108), the p-wave nucleon-pion operator (Eq. 3.57), and the s-wave nucleon-pion-pion operator (Eq. 3.58). This analysis is performed on the ensembles listed in the upper part of Tab. 5.1. The discussion in this section focuses on ensemble L, as its results are representative of the general behavior observed across all analyzed ensembles.
The effective masses $am_{\text{eff}}(t)$ corresponding to the three lowest GEVP modes are presented in Fig. 8.1, along with the effective mass curve obtained from the two-point nucleon function, shown in red for reference. All mass curves exhibit well-defined plateaus within a temporal region where the signal-to-noise ratio remains favorable and the modes are clearly distinguishable. Each curve is modeled using the functional form described in Eq. 8.1, with fits applied to the filled data points. The predictions of the resulting models are visualized as shaded bands, matched in color to their respective data sets, and representing the 1σ confidence intervals. The criteria governing the choice of fit ranges are detailed in Sec. 5.5, in particular, the end points of the fit ranges are manually selected to lie within good signal-to-noise behavior to ensure fit stability.
In Fig. 8.1, the dashed horizontal line labeled N denotes the average nucleon mass extracted from the fit to GEVP mode 0. Additional lines indicate the expected non-interacting energies of multi-hadron states. Specifically, the energy of the $N\pi$ state is given by

$$aE_{N\pi} = a\left(\sqrt{m_N^2 + p^2} + \sqrt{m_\pi^2 + p^2}\right), \tag{8.2}$$

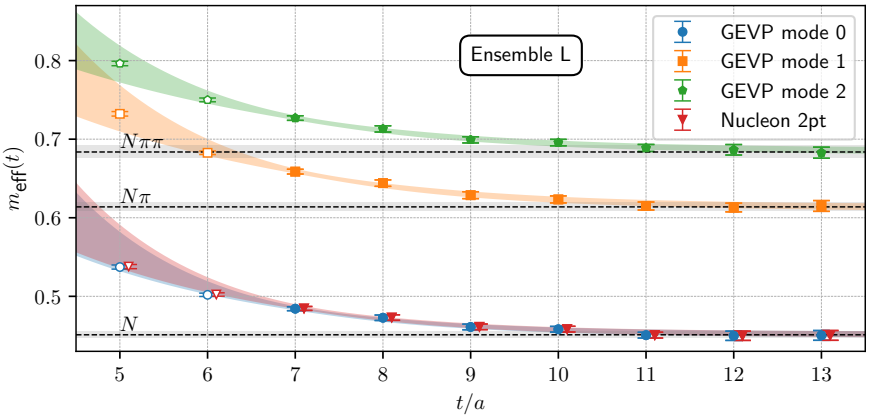

Figure 8.1.: Comparison of the effective energies obtained from the three lowest GEVP modes with the effective mass extracted from the nucleon two-point function on ensemble L. Colored bands, matching the data point colors, represent the results of excited-state fits using the model described in Eq. 8.1, based on all filled data points. The dashed line labeled N indicates the central value of the nucleon mass extracted from the excited-state fit to GEVP mode 0. The additional lines, labeled $N\pi$ and $N\pi\pi$, correspond to the non-interacting energy levels of the $N\pi$ state in a p-wave and the $N\pi\pi$ state in an s-wave, respectively. Shaded regions around these lines depict the corresponding 1σ uncertainty estimates.

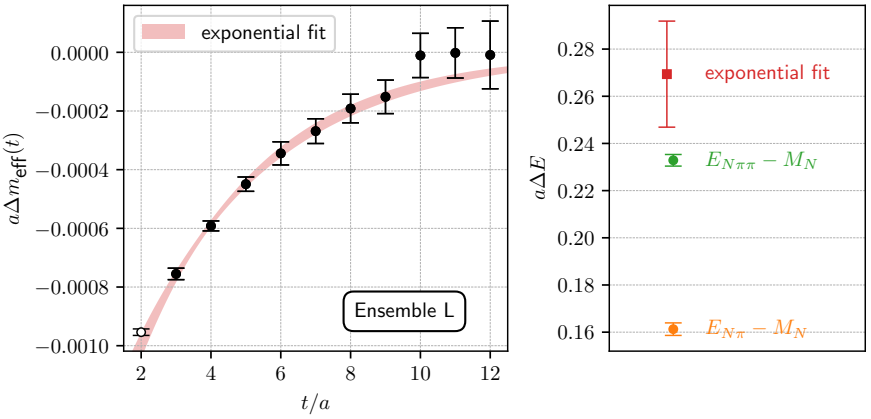

Figure 8.2.: Left: The data points show the effective mass difference Δm_{eff} between GEVP mode 0 and the nucleon two-point function for ensemble L, as defined in Eq. 8.4. The red band represents an exponential fit to the filled data points, based on the functional form $f(t; A, \Delta E) = Ae^{-\Delta E t}$. Right: The extracted energy gap $a\Delta E$ from this fit is displayed and compared to energy differences obtained from the GEVP analysis, namely $E_{N\pi\pi} - M_N$ and $E_{N\pi} - M_N$.

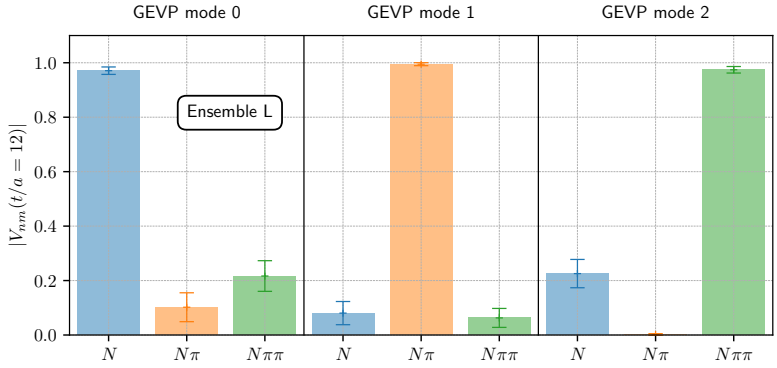

Figure 8.3.: GEVP eigenvectors evaluated at $t/a = 12$ for ensemble L, normalized according to the Sinkhorn-Knopp algorithm described in Sec. 5.9.1.

where m_N is the fitted nucleon mass, m_π is the pion mass taken from Tab. 5.1, and p denotes the momentum, with $ap = \frac{2\pi}{L}$. The non-interacting energy of the $N\pi\pi$ system is approximated by

$$aE_{N\pi\pi} = m_N + 2m_\pi. \tag{8.3}$$

A key observation in Fig. 8.1 is the small difference between the effective mass of GEVP mode 0 and that of the standard two-point nucleon correlator. This difference is quantified as

$$a\Delta m_{\text{eff}}(t) = am_{\text{eff}}^{\text{GEVP0}}(t) - am_{\text{eff}}^{\text{2pt}}(t), \tag{8.4}$$

and shown in Fig. 8.2. The observed discrepancy is at the per mille level, underscoring the precision of the comparison.
To further interpret this difference, we approximate the effective mass from the two-point function as

$$am_{\text{eff}}^{\text{2pt}}(t) = am_N + A_{N\pi}e^{-(E_{N\pi}-m_N)t} + A_{N\pi\pi}e^{-(E_{N\pi\pi}-m_N)t} + A_{N^\star}e^{-(E_{N^\star}-m_N)t}, \tag{8.5}$$

where the terms represent contributions from multi-hadron and excited baryon states. In contrast, since the $N\pi$ and $N\pi\pi$ operators are included in the GEVP basis, these states are projected out in GEVP mode 0, leaving an effective mass described by

$$am_{\text{eff}}^{\text{GEVP0}}(t) = am_N + A'N^\star e^{-(EN^\star-m_N)t}. \tag{8.6}$$

The resulting difference $\Delta m_{\text{eff}}(t)$ is therefore expected to follow an exponential behavior:

$$a\Delta m_{\text{eff}}(t) \propto e^{-(E_X-m_N)t}, \tag{8.7}$$

where X denotes either the $N\pi$ or $N\pi\pi$ state, depending on which dominates. The red band in Fig. 8.2 shows the fit of this form to the data, using the same range selection criteria used in the effective mass fits described earlier.
The right panel of Fig. 8.2 compares the extracted energy gap $\Delta E = E_X - m_N$ from this single-exponential fit to the corresponding energy differences determined directly from the GEVP spectrum. The fitted value is found to be consistent within 2σ of the gap $E_{N\pi\pi} -$

M_N, suggesting that the $N\pi\pi$ state represents the dominant multi-hadron contamination in the nucleon two-point function for this ensemble and operator basis.
Additional information is provided by Fig. 8.3, which shows the normalized GEVP eigenvectors at $t/a = 8$ for ensemble L, using the normalization scheme described in Sec. 5.9.1. The composition of the eigenvector indicates that GEVP mode 0 is primarily dominated by the nucleon operator, mode 1 by the $N\pi$ operator, and mode 2 by the $N\pi\pi$ operator. In particular, the $N\pi\pi$ state (mode 2) exhibits a larger component of the nucleon interpolator than the $N\pi$ state (mode 1), which is in agreement with the results of the fit of Δm_{eff}. The significant excited-state contamination observed in GEVP mode 0 highlights the presence of additional contributions beyond those considered here, motivating future investigations using an expanded operator basis.
In the case of the other ensembles, we achieve results that are largely similar. We can differentiate the distinct eigenmodes, and all effective masses either converge to the nucleon mass or approach the energy level of the associated non-interacting particles (see Fig. A.1). Additionally, for every ensemble, we note only a minimal difference between the 0th mode of the GEVP and the nucleon 2-point function. The exponential fit applied to this difference reveals energy gaps within a range of 2σ from one of the gaps determined by the GEVP. For the eigenvectors of the additional ensembles, we identified that the primary contribution aligns with the anticipated state based on its energy. Moreover, it is generally found that the state with the second highest contribution from the nucleon operator corresponds to the state whose energy gap is closest to the estimated energy gap derived from the single exponential fit of Δm_{eff}.
In summary, we find that the contributions of $N\pi$ and $N\pi\pi$ to the nucleon two-point function are negligible for estimating the nucleon mass, consistent with previous findings in [74, 75] through chiral perturbation theory. For the $N\pi$ and $N\pi\pi$ states, we develop new operators that do not overlap with the ground state or other multi-hadronic states present in the GEVP operator set. Fig. 8.4 provides a comprehensive overview of the energies for all N, $N\pi$, and $N\pi\pi$ states across different ensembles. In the majority of ensembles, the energies of multi-hadronic states match the non-interacting particle energies, except for ensemble 9, which shows a 2σ discrepancy.
All ensemble fit results are presented in Tab. A.1, with a brief description provided in Sec. A.3.

8.1.2. Finite Volume Correction

To account for finite volume effects in the positive parity sector, we apply the correction derived from relativistic $SU(2)_f$ baryon chiral perturbation theory (BχPT), following the formulation presented in [115, 116]. The finite volume shift in the nucleon mass is given by

$$m_N(L) - m_N(\infty) = \Delta_a(L) + \Delta_b(L), \tag{8.8}$$

where $\Delta_a(L)$ and $\Delta_b(L)$ denote the contributions at orders $\mathcal{O}(p^3)$ and $\mathcal{O}(p^4)$, respectively. The leading-order correction, $\Delta_a(L)$, takes the form

$$\Delta_a(L) = \frac{3g_A^2 m_0 m_\pi^2}{16\pi^2 f_\pi^2} \int_0^\infty \mathrm{d}x \sum_{\boldsymbol{n}\neq\boldsymbol{0}} K_0\left(L|\boldsymbol{n}|\sqrt{m_0^2 x^2 + m_\pi^2(1-x)}\right), \tag{8.9}$$

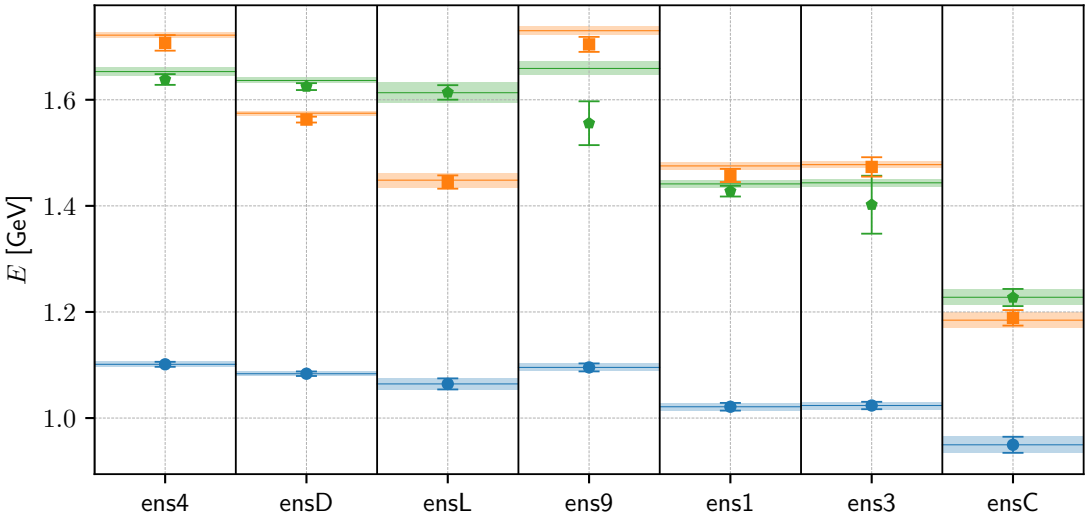

Figure 8.4.: Summary of the extracted energy levels across all ensembles. Data points represent the energies obtained from the individual GEVP analyses in the positive parity channel. The color coding identifies each state: the nucleon is shown in blue, the $N\pi$ state in orange, and the $N\pi\pi$ state in green. Solid blue lines indicate the central value of the nucleon mass, while additional lines mark the expected non-interacting energies of the $N\pi$ and $N\pi\pi$ systems. Shaded bands around these reference lines depict the associated 1σ uncertainties of the non-interacting energy estimates.

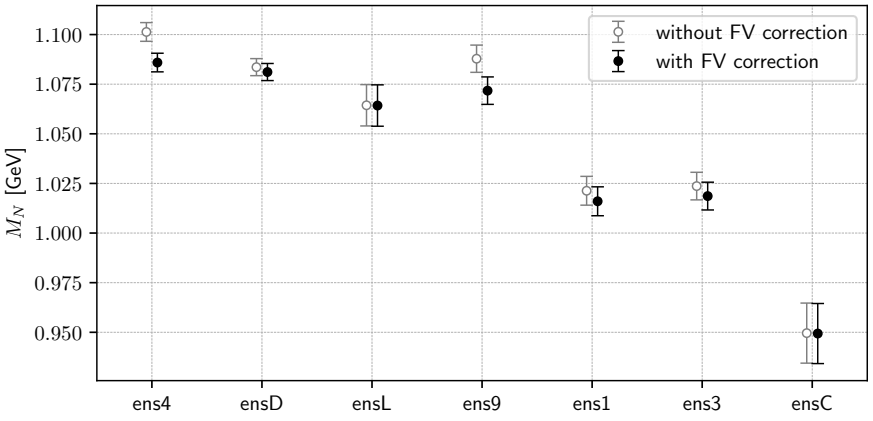

Figure 8.5.: Finite volume (FV) corrections to the nucleon masses for the various ensembles. Open symbols indicate the nucleon masses prior to applying the finite volume correction, while solid symbols represent the corrected values.

where K_0 denotes the modified Bessel function of the second kind, and the sum runs over all non-zero integer vectors $\boldsymbol{n}$ in three dimensions. The parameters g_A, f_π, and m_0 correspond to the axial coupling, the pion decay constant, and the nucleon mass in the chiral limit, respectively.
The next-to-leading order correction, $\Delta_b(L)$, introduces additional low-energy constants c_1, c_2, and c_3, and is given by

$$\Delta_b(L) = \frac{3m_\pi^4}{4\pi^2 f_\pi^2} \sum_{\boldsymbol{n}\neq\boldsymbol{0}} \left[(2c_1 - c_3) \frac{K_1(L|\boldsymbol{n}|m_\pi)}{L|\boldsymbol{n}|m_\pi} + c_2 \frac{K_2(L|\boldsymbol{n}|m_\pi)}{(L|\boldsymbol{n}|m_\pi)^2} \right], \tag{8.10}$$

where K_1 and K_2 are also modified Bessel functions of the second kind.
For the evaluation of the finite volume corrections, we adopt the values $g_A = 1.2754(13)$ and $f_\pi = 92.07(84)$ MeV, as reported by the Particle Data Group [52]. The nucleon mass in the chiral limit is taken to be $m_0 = 0.8566(17)$ GeV, following the determination in [117]. The low-energy constants (LECs) c_1, c_2, and c_3 are extracted from the N^{3}LO heavy-baryon chiral perturbation theory (HBχ PT) within the Δ-less framework, based on the HB-πN data in [118]. The specific values used are $c_1 = -1.11(3)$ GeV^{-1}, $c_2 = 3.17(3)$ GeV^{-1}, and $c_3 = -5.67(6)$ GeV^{-1}. These values are consistent with those obtained from alternative formulations, such as the HB-NN approach and covariant chiral perturbation theory, indicating that there are no significant discrepancies between the methods.
Fig. 8.5 illustrates the impact of finite-volume corrections on the nucleon mass estimates for selected ensembles. In particular, ensembles `ens4` and `ensD`, which differ only in volume, exhibit significantly improved agreement following the application of the correction. Before correction, the discrepancy between their nucleon mass values is approximately 2.8σ, which is reduced to 0.7σ after correction, thereby supporting the reliability of the applied methodology. A similar trend is observed for ensembles `ensL` and `ens9`, which also differ only in volume.
Statistical uncertainties in the input parameters are propagated by generating synthetic jackknife samples, where each parameter is sampled from a Gaussian distribution defined

by its central value and the uncertainty quoted.

8.1.3. Physical Point Extrapolation of the Nucleon Mass

The extrapolation to the continuum limit and to the physical masses of pion and kaons, also called physical point extrapolation, is performed using a model-averaging approach based on the Akaike Information Criterion (AIC) [119, 120]. The AIC for a given model is defined as

$$\mathrm{AIC} = 2k + \chi^2 \tag{8.11}$$

where k denotes the number of fit parameters and χ^2 is the chi-square value of the fit. This criterion enables the construction of a weighted average for the parameter of interest, here denoted as β, via

$$\bar{\beta} = \sum_{\mathcal{M}} P(\mathcal{M})\beta_{\mathcal{M}}, \tag{8.12}$$

where $\mathcal{M}$ indexes the models considered, and $\beta_{\mathcal{M}}$ is the estimate of β from model $\mathcal{M}$. The weight assigned to each model is given by its AIC-derived probability,

$$P(\mathcal{M}) = \frac{e^{-\mathrm{AIC}_{\mathcal{M}}}}{\sum_{\mathcal{M}'} e^{-\mathrm{AIC}_{\mathcal{M}'}}}. \tag{8.13}$$

Statistical uncertainties are quantified using jackknife resampling, while the systematic uncertainty associated with model averaging is computed as the variance of the weighted model estimates,

$$\mathrm{Var}(\beta)_{\mathrm{sys}} = \sum_{\mathcal{M}} P(\mathcal{M})(\beta_{\mathcal{M}} - \bar{\beta})^2. \tag{8.14}$$

The functional forms considered in model averaging are designed to capture the dependence of the nucleon mass on the lattice spacing a, the pion mass m_π, and the kaon mass m_K. Given that domain-wall fermions exhibit discretization effects at $\mathcal{O}(a^2)$, we include a term of the form $c_1 a^2$ to account for lattice artifacts. The models are further constructed to ensure that the constant term M_N corresponds to the nucleon mass evaluated at the physical pion and kaon masses, m_π^0 and m_K^0, respectively.
In terms of the hadronic mass dependence, we examine several parameterizations. For the kaon mass, we consider linear, quadratic, or no dependence. For the pion mass, two different ansätze are employed: (i) functional forms inspired by chiral perturbation theory, beginning with quadratic terms and optionally extended to cubic order to test consistency, following the approach in [115], and (ii) linear dependence models, as proposed in [121].
A total of nine models are evaluated as part of the model averaging procedure, with a detailed overview provided in Tab. 8.1. Representative results from one of these models, a linear dependence on the pion mass combined with a quadratic dependence on the kaon mass, are shown in Fig. 8.6. This figure includes three subplots, each illustrating the nucleon mass as a function of one model parameter, while the remaining two parameters are fixed at their physical values. The projection of the initial data points to the physical point is visualized by gray transparent points and their corresponding extrapolated values, indicated by solid black markers. The horizontal red lines denote the confidence interval 1σ for the prediction of the nucleon mass, and the vertical dashed lines mark the physical values of the pion and kaon masses.

The results of the remaining models are summarized in Fig. A.6, Fig. A.7, and Fig. A.8, categorized by the form of their dependence on pion mass (linear, quadratic, and quadratic with cubic extension, respectively).
In this study, the pion and kaon masses, as well as the lattice spacing, were not determined on a per-configuration basis. To account for the associated statistical uncertainties, we generate synthetic data that reproduce the same statistical properties as the ensemble-averaged quantities. These synthetic values are treated identically to the measured data in the analysis, and their uncertainties are propagated using the single-elimination jackknife procedure.

Tag	Model function $\mathcal{M}(a, m_\pi, m_K)$
$\pi(1)K(0)$	$M_N + c_0 a^2 + c_1(m_\pi - m_\pi^0)$
$\pi(1)K(1)$	$M_N + c_0 a^2 + c_1(m_\pi - m_\pi^0) + c_2(m_K - m_K^0)$
$\pi(1)K(2)$	$M_N + c_0 a^2 + c_1(m_\pi - m_\pi^0) + c_2(m_K^2 - (m_K^0)^2)$
$\pi(2)K(0)$	$M_N + c_0 a^2 + c_1(m_\pi^2 - (m_\pi^0)^2)$
$\pi(2)K(1)$	$M_N + c_0 a^2 + c_1(m_\pi^2 - (m_\pi^0)^2) + c_2(m_K - m_K^0)$
$\pi(2)K(2)$	$M_N + c_0 a^2 + c_1(m_\pi^2 - (m_\pi^0)^2) + c_2(m_K^2 - (m_K^0)^2)$
$\pi(2,3)K(0)$	$M_N + c_0 a^2 + c_1(m_\pi^2 - (m_\pi^0)^2) + c_2(m_\pi^3 - (m_\pi^0)^3)$
$\pi(2,3)K(1)$	$M_N + c_0 a^2 + c_1(m_\pi^2 - (m_\pi^0)^2) + c_2(m_K - m_K^0) + c_3(m_\pi^3 - (m_\pi^0)^3)$
$\pi(2,3)K(2)$	$M_N + c_0 a^2 + c_1(m_\pi^2 - (m_\pi^0)^2) + c_2(m_K^2 - (m_K^0)^2) + c_3(m_\pi^3 - (m_\pi^0)^3)$

Table 8.1.: Overview of all models used for the physical point extrapolation.

The fit results for the nine models considered in the extrapolation analysis are summarized in Tab. 8.2. From these results, we observe that the kaon mass dependence is statistically insignificant and that the cubic pion mass term is not well constrained by our data, a result that is expected given the limited number of pion mass values (three) available in this study. In particular, the slope extracted from the linear pion-mass model is consistent with the estimate obtained via the "ruler approximation" discussed in [121].
The model probabilities $P(\mathcal{M})$, shown in Fig. 8.7, indicate a mild preference for the linear model over the others. Based on the model averaging procedure, we arrive at a final estimate for the nucleon mass at the physical point:

$$M_N = 0.926(21)_{\text{stat}}(06)_{\text{sys}}\ \text{GeV}, \tag{8.15}$$

which agrees with the experimentally observed value of the nucleon mass within one standard deviation.

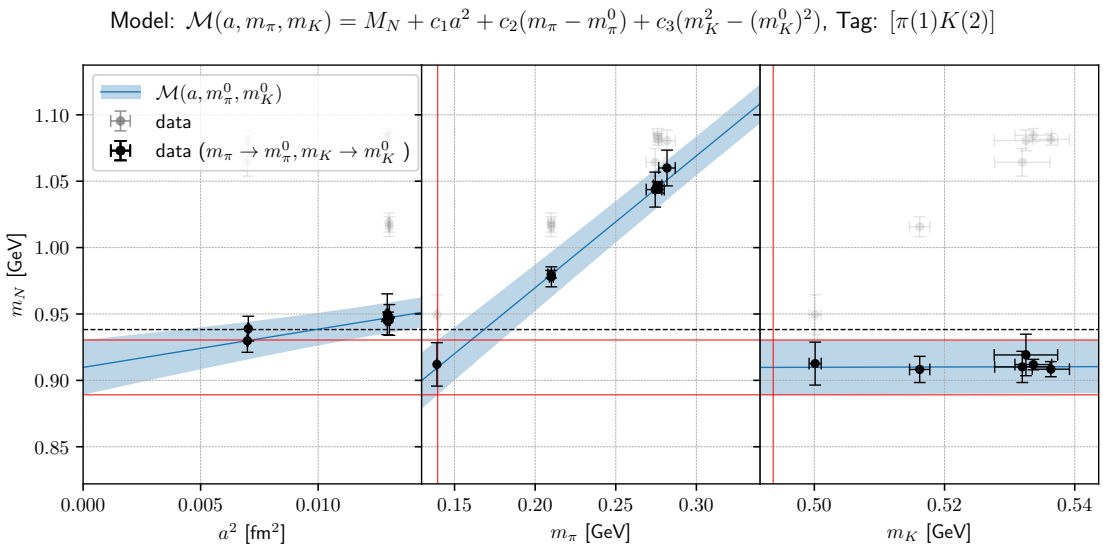

Figure 8.6.: Fit results for the extrapolation to the physical point. Each subplot illustrates the dependence of the fitted model on one of the variables: the lattice spacing a, the pion mass m_π, or the kaon mass m_K. The original data are shown as transparent grey points, while the corresponding projections to the physical values of the remaining parameters are indicated by solid black points. Red horizontal lines mark the 1σ confidence interval for the extrapolated nucleon mass, and vertical lines indicate the physical values of the pion and kaon masses.

Tag	M_N/GeV	c_0/GeV^3	c_1	$c_2^{(1)}$	$c_2^{(2)} \cdot$ GeV		χ^2/dof	p-value
$\pi(1)K(0)$	0.924(21)	0.073(52)	0.987(83)	—	—	—	0.89/4	0.93
$\pi(1)K(1)$	0.923(22)	0.072(52)	0.990(83)	0.02(11)	—	—	0.85/3	0.84
$\pi(1)K(2)$	0.910(21)	0.112(49)	0.993(82)	—	0.011(96)	—	0.73/3	0.87
Tag	M_N/GeV	c_0/GeV^3	$c_1 \cdot$ GeV	$c_2^{(1)}$	$c_2^{(2)} \cdot$ GeV	$c_3 \cdot$ GeV^2	χ^2/dof	p-value
$\pi(2)K(0)$	0.935(21)	0.081(55)	2.14(18)	—	—	—	1.67/4	0.80
$\pi(2)K(1)$	0.931(22)	0.079(55)	2.17(19)	0.07(11)	—	—	1.15/3	0.76
$\pi(2)K(2)$	0.931(22)	0.079(55)	2.17(19)	—	0.065(98)	—	1.15/3	0.76
$\pi(2,3)K(0)$	0.926(23)	0.074(52)	4.3(2.3)	—	—	−6.2(6.5)	0.89/3	0.83
$\pi(2,3)K(1)$	0.926(23)	0.074(53)	3.9(2.6)	0.04(12)	—	−4.9(7.5)	0.77/2	0.68
$\pi(2,3)K(2)$	0.926(23)	0.074(53)	3.9(2.7)	—	0.04(11)	−4.9(7.6)	0.77/2	0.68

Table 8.2.: Results from the various extrapolations to the physical point. Model labels correspond to those defined in Tab. 8.1. The coefficients $c_2^{(1)}$ and $c_2^{(2)}$ represent the prefactors of the linear and quadratic kaon-mass terms, respectively.

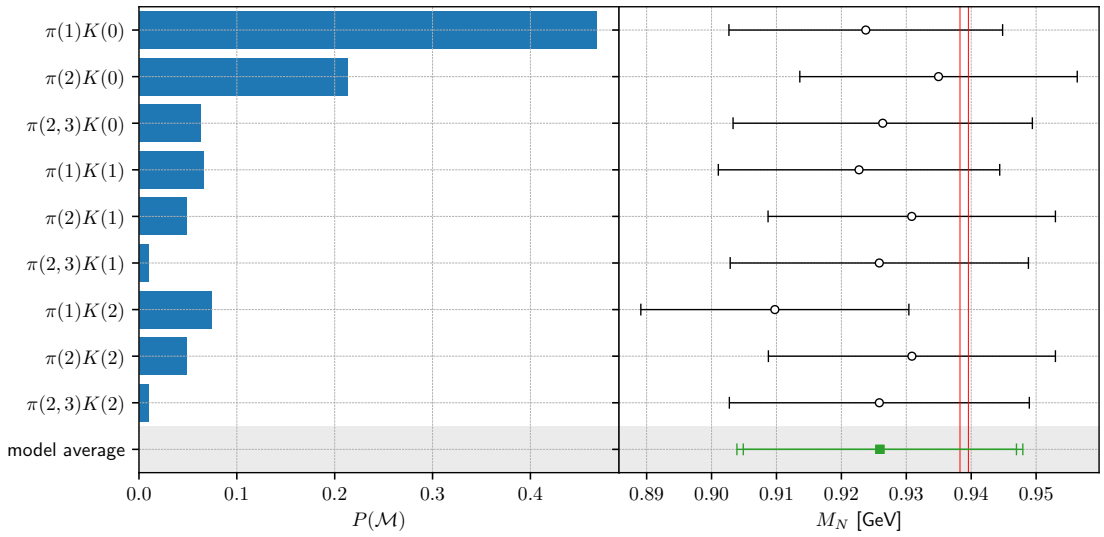

Figure 8.7.: Left: Model probabilities computed using the Akaike Information Criterion (AIC). Right: Nucleon mass estimates from each individual model, along with the model-averaged result as defined in Eq. 8.12. Vertical lines indicate the experimental values of the proton and neutron masses. Model labels correspond to those provided in Tab. 8.1.

8.2. Negative Parity Sector

The spectral analysis in the negative parity sector is performed using a generalized eigenvalue problem (GEVP) constructed from three interpolating operators: the nucleon operator with negative parity projection (see Eq. 3.47), the nucleon-pion operator with both particles at rest (cf. Eq. 3.59), and the nucleon-pion operator in a back-to-back momentum configuration (cf. Eq. 3.60).
Fig. 8.8 presents the effective mass curves extracted from the GEVP analysis for ensemble 9, shown alongside the effective mass of the two-point negative parity nucleon function, represented by red data points. As in the positive parity channel, excited-state fits are performed on all effective mass curves. The black dashed lines indicate the energies of the non-interacting $N\pi$ states, where the nucleon mass input is taken from the fits in the positive parity channel. For reference, the gray dash-dotted lines correspond to the masses of the two lowest-lying negative parity nucleon resonances, $N(1535)$ and $N(1650)$, as reported by the Particle Data Group [52]. The corresponding normalized eigenvectors at time slice $t/a = 8$ are shown in Fig. 8.9, using the normalization procedure described in Sec. 5.9.1.
The GEVP modes that exhibit the strongest overlap with multi-hadronic states display a clear and statistically robust signal. In contrast, the nucleon two-point correlation function in the negative parity channel suffers from significant signal-to-noise degradation. A similar pattern is observed across the remaining ensembles, as shown in Fig. A.4, with the corresponding eigenvectors presented in Fig. A.5. In particular, the signal quality of the nucleon two-point function is, in most cases, even poorer than that observed for ensemble 9. One plausible explanation is that the number of high modes included in the distillation setup is insufficient to adequately resolve higher energetic single-particle states. This interpretation is supported by the observation that the two ensembles with the most pronounced and stable signals, namely ensembles 4 and 9, also possess the narrowest smearing profiles, as illustrated in Fig. 5.2.
Despite the limitations in signal quality for the nucleon two-point function, all ensembles exhibit a clear and consistent signal for the multi-hadronic states. In contrast to the positive parity sector, the nucleon two-point correlator in the negative parity channel shows a substantial overlap with the nucleon-pion states. However, a more refined analysis in this sector would likely require an increase in the number of Laplacian eigenmodes in the distillation framework or the adoption of an alternative strategy to incorporate the distillation space, such as the approach proposed in [122]. As in positive parity analysis, the results of excited state fits performed within the GEVP framework are summarized in Tab. A.2, with additional details provided in Sec. A.3.

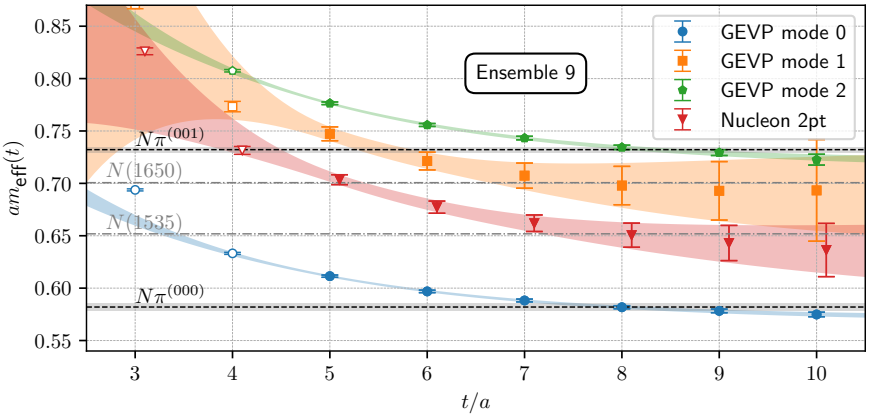

Figure 8.8.: Effective mass curves of the GEVP eigenstates (modes 0, 1, and 2) in the negative parity sector for ensemble 9, compared with the effective mass from the corresponding nucleon two-point function. The black dashed lines indicate the non-interacting energies of the nucleon-pion system with both particles at rest ($N\pi^{(000)}$) and with back-to-back momentum of magnitude $|\boldsymbol{p}| = \frac{2\pi}{aL}$ ($N\pi^{(001)}$). The grey bands surrounding these lines denote the 1σ uncertainty in the energy estimates. Dash-dotted lines correspond to the physical masses of the negative parity nucleon resonances $N(1535)$ and $N(1650)$.

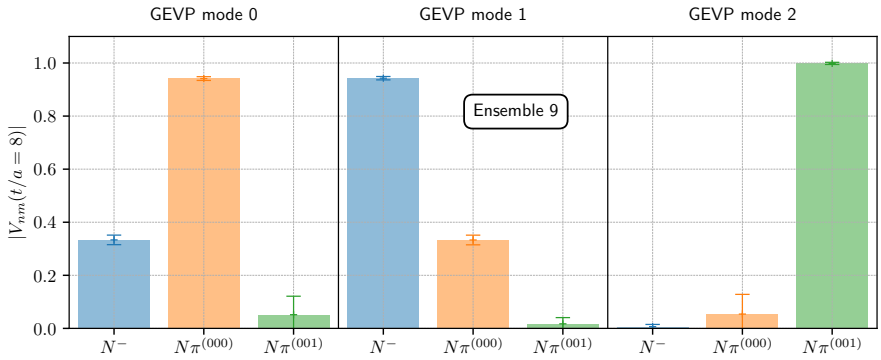

Figure 8.9.: Negative parity GEVP eigenvectors at $t/a = 8$ for ensemble 9, renormalized according to the scheme described in Sec. 5.9.1.

9. Summary and Outlook

In Ch. 6, we carried out a comparison between non-projected and projected omega operators. We utilized a GEVP analysis for the projected operators and employed constrained fits for both types. The comparison of the ground and first excited state energies reveals no notable differences, suggesting that non-projected operators are equally effective in determining the omega mass. Nevertheless, because projecting the operator generally does not require extra computational effort, it is advisable to include it.
The ρ and two-pion spectroscopy discussed in Ch. 7 confirmed the effectiveness of the distillation method for the spectral analysis needed to reconstruct the long-distance window of the hadronic vacuum polarization's contribution to the muon's anomalous magnetic moment. Additionally, we showed that for momentum configurations involving back-to-back two-pion states with two T_{1u} irreducible representations included in the vector space, both operators play a crucial role in performing an accurate spectral analysis. Currently, it is a plausible hypothesis that the extra states might be associated with $J = 3$ states. This could be examined by, for example, analyzing A_2 projected states and would be a natural extension to this project.
In Ch. 8, distinct conclusions can be drawn for the two parity channels examined in this chapter. In the positive parity sector, the results are unambiguous and stable across all ensembles detailed in the upper part of Tab. 5.1 using a GEVP built from three interpolating operators: the nucleon, a nucleon pion, and, newly introduced in this study, a nucleon-pion-pion operator. For all ensembles, the ground state signal is distinct, leading to precise mass extraction with relative uncertainties between approximately 0.3% and 2%. The energies of multi-hadronic excited states agree with the corresponding non-interacting levels, as shown in Fig. 8.4. A slight anomaly occurs in ensemble 9, where both the $N\pi\pi$ and $N\pi$ energies are roughly 2σ below the predicted non-interacting values. However, the broader significance of this discrepancy is unclear.
Additionally, our results support the expectation of chiral perturbation theory that the $N\pi$ and $N\pi\pi$ states contribute negligibly to the two-point nucleon function [74]. This is evidenced by the minimal difference between the effective mass extracted from the two-point function and that of the ground-state GEVP mode. We quantify this suppression by analyzing the effective mass difference between the two observables. An exponential fit to this difference yields an energy gap that is consistent, within 2σ, with the gap obtained from the GEVP spectrum between the ground state and the excited state with the next-largest overlap with the nucleon interpolator, as determined from the GEVP eigenvectors.
Following the spectral analysis, we applied finite-volume corrections to the nucleon masses based on the $SU(2)_f$ baryon chiral perturbation theory. To validate these corrections, we examined ensemble pairs that differ solely in spatial volume: ensembles 4 and D, and ensembles L and 9. In both cases, the corrected nucleon masses agree within statistical uncertainties.
We also performed a continuum and physical point extrapolation of the nucleon mass

using nine distinct fit models incorporating linear, quadratic, and quadratic-plus-cubic pion-mass dependencies. All models yielded reasonable values of χ^2/dof, enabling the use of model averaging through the Akaike Information Criterion. The final nucleon mass result is consistent with the experimental values of the proton and neutron within the quoted uncertainties:

$$M_N = 0.926(21)_{\text{stat}}(06)_{\text{sys}} \text{ GeV} \tag{9.1}$$

The effects of isospin breaking and QED were not included in this analysis, as overall uncertainties remain too large for these effects to be relevant. The main objective of this study was to evaluate the suitability of our distillation setup, which was originally optimized for the RBC/UKQCD $g-2$ program, for baryon spectroscopy. Our findings confirm that this setup is also well suited for baryon physics, providing a solid foundation for future investigations.

In the negative parity sector, we conducted a similar GEVP analysis using a basis consisting of a nucleon interpolator and two nucleon-pion operators (with both at rest and back-to-back momentum configurations). The main limitation in this channel arises from the relatively small number of Laplacian eigenmodes used in the distillation smearing. While the multi-hadronic states are resolved with similar clarity as for the positive parity case, the nucleon two-point function exhibits a significantly degraded signal-to-noise ratio. This limitation is most apparent in ensembles with broader smearing profiles. Conversely, ensembles with narrower smearing, particularly ensembles 4 and 9, produce the clearest signals, supporting the conclusion that a larger number of distillation modes is required to perform a more sophisticated analysis of negative parity baryons.

Continuing on the research outlined in this thesis, several promising directions for future studies become apparent. An intuitive progression from spectroscopy analysis involves using the optimized operators derived from the GEVP to calculate the form factors for a variety of processes, including $N \to N$, $N \to N\pi$, and $N \to N\pi\pi$. Furthermore, another intriguing path involves calculating the transition form factors for $N \to \Delta$, which are of considerable significance for simulating neutrino-nucleon interactions within the resonance regime. Moreover, detecting Roper resonance signals through nucleon-pion and nucleon-pion-pion scattering through distillation techniques and the Lüscher method represents another relevant direction, particularly due to its importance in neutrino-nucleon scattering within the resonance regime [60].

Acknowledgment

First and foremost, I would like to express my deepest gratitude to my supervisor, Prof. Dr. Christoph Lehner, for giving me the opportunity to pursue a PhD under his guidance. His insightful advice and encouragement have been invaluable throughout my doctoral studies. This dissertation would not have been possible without his unwavering support and mentorship.
I extend my gratitude to Prof. Dr. Gunnar Bali, Prof. Dr. Franz J. Gissibl, and Prof. Dr. Ferdinand Evers for agreeing to participate in my examination committee.
I would also like to thank Dr. Davide Giusti for numerous helpful discussions and for generously sharing his expertise. Special thanks go to Aaron Meyer for his valuable input at various stages, and to Dr. Michael Wagman for the fruitful and welcoming discussions during my research visit at Fermilab, which were both inspiring and enjoyable.
My gratitude extends to all colleagues from the RBC/UKQCD collaboration, not only for providing the essential distillation data, but also for engaging in insightful discussions during collaboration meetings. Their feedback and shared expertise significantly contributed to the development of this research.
I would also like to thank Marcel Rodekamp, Daniel Knüttel, and Julian Parrino for their time and effort in proofreading this thesis. Moreover, I am grateful to Lisa Walter, Marcel Rodekamp, Julian Parrino, Tobias Sitzmann, Simon Pfahler, Valentin Moss, Sebastian Spiegel, and Daniel Knüttel for countless coffee breaks with delightful conversations about both physics and life. My thanks also go to my colleagues at the Hans-Böckler Foundation, whose interdisciplinary perspectives and discussions helped me to view my research through a broader lens.
A special acknowledgment goes to my office mates and close friends, Sebastian Spiegel and Daniel Knüttel, for their constant support, encouragement, and camaraderie throughout the entirety of my PhD journey. Their presence amplified the joy of successes and made difficulties more tolerable. Last but certainly not least, I would like to thank my family and friends, whose continued support, understanding, and belief in me have carried me through the many ups and downs. Their unwavering support has been the cornerstone of this achievement, and I am truly grateful.
This thesis received financial support through a scholarship provided by the Hans-Böckler Foundation. The contractions were executed on the QPace3 and QPace4 local clusters utilizing Numpy [123] and Jax [124]. Statistical analysis was performed using QStatPy [92], and for data fitting, Scipy [125] was partially used. The graphics used throughout this thesis were generated with Matplotlib [126], PGF/Tikz [127], and Tikz-Feynman [128]. The quark inversions and gauge fixing were done using GPT [103], which uses Grid [129–131] to achieve performance portability. All contractions were performed using AutoWick [102].

Bibliography

[1] R. Mitalas and K.R. Sills. "On the Photon Diffusion Time Scale for the Sun". In: *Astrophys. J.*, 401 (1992). DOI: doi:10.1086/172103.

[2] A. D. Sakharov. "Violation of CP Invariance, C asymmetry, and baryon asymmetry of the universe". In: *Pisma Zh. Eksp. Teor. Fiz.* 5 (1967), pp. 32–35. DOI: 10.1070/PU1991v034n05ABEH002497.

[3] Edward W. Kolb and Michael S. Turner. *The Early Universe*. Vol. 69. Taylor and Francis, May 2019. ISBN: 978-0-429-49286-0, 978-0-201-62674-2. DOI: 10.1201/9780429492860.

[4] T. Blum et al. "Long-Distance Window of the Hadronic Vacuum Polarization for the Muon g-2". In: *Phys. Rev. Lett.* 134.20 (2025), p. 201901. DOI: 10.1103/PhysRevLett.134.201901. arXiv: 2410.20590 [hep-lat].

[5] Andreas Hackl and Christoph Lehner. "Spectral analysis for nucleon-pion and nucleon-pion-pion states in both parity sectors using distillation with domain-wall fermions". In: (Dec. 2024). arXiv: 2412.17442 [hep-lat].

[6] Christof Gattringer and Christian B. Lang. *Quantum chromodynamics on the lattice*. Vol. 788. Berlin: Springer, 2010. ISBN: 978-3-642-01849-7, 978-3-642-01850-3. DOI: 10.1007/978-3-642-01850-3.

[7] Istvan Montvay and Gernot Münster. *Quantum Fields on a Lattice*. Cambridge Monographs on Mathematical Physics. Cambridge University Press, 1994.

[8] Wu-Ki Tung. *Group Theory in Physics*. WORLD SCIENTIFIC, 1985. DOI: 10.1142/0097. eprint: https://www.worldscientific.com/doi/pdf/10.1142/0097. URL: https://www.worldscientific.com/doi/abs/10.1142/0097.

[9] Michael E Peskin and Daniel V Schroeder. *An introduction to quantum field theory*. Includes exercises. Boulder, CO: Westview, 1995. URL: https://cds.cern.ch/record/257493.

[10] Steven Weinberg. *The Quantum Theory of Fields*. Cambridge University Press, 1995.

[11] Y. Iwasaki. "Renormalization Group Analysis of Lattice Theories and Improved Lattice Action. II. Four-dimensional non-Abelian SU(N) gauge model". In: (Dec. 1983). arXiv: 1111.7054 [hep-lat].

[12] Kenneth G. Wilson. "Confinement of quarks". In: *Phys. Rev. D* 10 (8 Oct. 1974), pp. 2445–2459. DOI: 10.1103/PhysRevD.10.2445. URL: https://link.aps.org/doi/10.1103/PhysRevD.10.2445.

[13] H. B. Nielsen and M. Ninomiya. "A no-go theorem for regularizing chiral fermions". In: *Physics Letters B* 105.2-3 (Oct. 1981), pp. 219–223. DOI: 10.1016/0370-2693(81)91026-1.

[14] H. B. Nielsen and M. Ninomiya. "Absence of neutrinos on a lattice (I). Proof by homotopy theory". In: *Nuclear Physics B* 185.1 (July 1981), pp. 20–40. DOI: 10.1016/0550-3213(81)90361-8.

[15] H. B. Nielsen and M. Ninomiya. "Absence of neutrinos on a lattice (II). Intuitive topological proof". In: *Nuclear Physics B* 193.1 (Dec. 1981), pp. 173–194. DOI: 10.1016/0550-3213(81)90524-1.

[16] Paul H. Ginsparg and Kenneth G. Wilson. "A remnant of chiral symmetry on the lattice". In: *Phys. Rev. D* 25 (10 May 1982), pp. 2649–2657. DOI: 10.1103/PhysRevD.25.2649. URL: https://link.aps.org/doi/10.1103/PhysRevD.25.2649.

[17] Rajamani Narayanan and Herbert Neuberger. "Chiral determinant as an overlap of two vacua". In: *Nucl. Phys. B* 412 (1994), pp. 574–606. DOI: 10.1016/0550-3213(94)90393-X. arXiv: hep-lat/9307006.

[18] Rajamani Narayanan and Herbert Neuberger. "Chiral fermions on the lattice". In: *Phys. Rev. Lett.* 71.20 (1993), p. 3251. DOI: 10.1103/PhysRevLett.71.3251. arXiv: hep-lat/9308011.

[19] Rajamani Narayanan and Herbert Neuberger. "Infinitely many regulator fields for chiral fermions". In: *Phys. Lett. B* 302 (1993), pp. 62–69. DOI: 10.1016/0370-2693(93)90636-V. arXiv: hep-lat/9212019.

[20] Rajamani Narayanan and Herbert Neuberger. "A Construction of lattice chiral gauge theories". In: *Nucl. Phys. B* 443 (1995), pp. 305–385. DOI: 10.1016/0550-3213(95)00111-5. arXiv: hep-th/9411108.

[21] Herbert Neuberger. "Exactly massless quarks on the lattice". In: *Phys. Lett. B* 417 (1998), pp. 141–144. DOI: 10.1016/S0370-2693(97)01368-3. arXiv: hep-lat/9707022.

[22] Herbert Neuberger. "More about exactly massless quarks on the lattice". In: *Phys. Lett. B* 427 (1998), pp. 353–355. DOI: 10.1016/S0370-2693(98)00355-4. arXiv: hep-lat/9801031.

[23] Herbert Neuberger. "Vectorlike gauge theories with almost massless fermions on the lattice". In: *Phys. Rev. D* 57 (9 May 1998), pp. 5417–5433. DOI: 10.1103/PhysRevD.57.5417. URL: https://link.aps.org/doi/10.1103/PhysRevD.57.5417.

[24] Richard C. Brower, Harmut Neff, and Kostas Orginos. "The Möbius domain wall fermion algorithm". In: *Comput. Phys. Commun.* 220 (2017), pp. 1–19. DOI: 10.1016/j.cpc.2017.01.024. arXiv: 1206.5214 [hep-lat].

[25] Robert G. Edwards, Urs M. Heller, and Rajamani Narayanan. "Approach to the continuum limit of the quenched Hermitian Wilson-Dirac operator". In: *Phys. Rev. D* 60 (3 June 1999), p. 034502. DOI: 10.1103/PhysRevD.60.034502. URL: https://link.aps.org/doi/10.1103/PhysRevD.60.034502.

[26] F. Knechtli, M. Günther, and M. Peardon. *Lattice Quantum Chromodynamics: Practical Essentials*. SpringerBriefs in Physics. Springer Netherlands, 2016. ISBN: 9789402409994. URL: https://books.google.de/books?id=JgZODQAAQBAJ.

[27] M. R. Hestenes and E. Stiefel. "Methods of conjugate gradients for solving linear systems". In: *Journal of research of the National Bureau of Standards* 49 (1952), pp. 409–436.

[28] H. A. van der Vorst. "Bi-CGSTAB: A Fast and Smoothly Converging Variant of Bi-CG for the Solution of Nonsymmetric Linear Systems". In: *SIAM Journal on Scientific and Statistical Computing* 13.2 (1992), pp. 631–644. DOI: 10.1137/0913035. eprint: https://doi.org/10.1137/0913035. URL: https://doi.org/10.1137/0913035.

[29] Youcef Saad and Martin H. Schultz. "GMRES: A Generalized Minimal Residual Algorithm for Solving Nonsymmetric Linear Systems". In: *SIAM Journal on Scientific and Statistical Computing* 7.3 (1986), pp. 856–869. DOI: 10.1137/0907058. eprint: https://doi.org/10.1137/0907058. URL: https://doi.org/10.1137/0907058.

[30] R. Babich et al. "Adaptive multigrid algorithm for the lattice Wilson-Dirac operator". In: *Phys. Rev. Lett.* 105 (2010), p. 201602. DOI: 10.1103/PhysRevLett.105.201602. arXiv: 1005.3043 [hep-lat].

[31] Thomas A. DeGrand and Richard D. Loft. "Wave function tests for lattice QCD spectroscopy". In: *Comput. Phys. Commun.* 65 (1991), pp. 84–91. DOI: 10.1016/0010-4655(91)90158-H.

[32] Dean Howarth and Joel Giedt. "The sigma meson from lattice QCD with two-pion interpolating operators". In: *Int. J. Mod. Phys. C* 28.10 (2017), p. 1750124. DOI: 10.1142/S0129183117501248. arXiv: 1508.05658 [hep-lat].

[33] O Oliveira and P.J Silva. "A global optimization method for Landau gauge fixing in lattice QCD". In: *Computer Physics Communications* 158.2 (2004), pp. 73–88. ISSN: 0010-4655. DOI: https://doi.org/10.1016/j.cpc.2003.12.001. URL: https://www.sciencedirect.com/science/article/pii/S0010465503005423.

[34] Mario Schröck and Hannes Vogt. "Coulomb, Landau and Maximally Abelian Gauge Fixing in Lattice QCD with Multi-GPUs". In: *Comput. Phys. Commun.* 184 (2013), pp. 1907–1919. DOI: 10.1016/j.cpc.2013.03.021. arXiv: 1212.5221 [hep-lat].

[35] G. Parisi. "The Strategy for Computing the Hadronic Mass Spectrum". In: *Phys. Rept.* 103 (1984). Ed. by C. Itzykson, Y. Pomeau, and N. Sourlas, pp. 203–211. DOI: 10.1016/0370-1573(84)90081-4.

[36] G. Peter Lepage. "The Analysis of Algorithms for Lattice Field Theory". In: *Theoretical Advanced Study Institute in Elementary Particle Physics*. June 1989.

[37] Howard Georgi and Kannan Jagannathan. "Lie Algebras in Particle Physics". In: *American Journal of Physics* 50 (1982), pp. 1053–1053. URL: https://api.semanticscholar.org/CorpusID:120974557.

[38] C J Bradley and A P Cracknell. *The Mathematical Theory Of Symmetry In Solids: Representation theory for point groups and space groups*. Oxford University PressOxford, Dec. 2009. ISBN: 9780191702334. DOI: 10.1093/oso/9780199582587.001.0001. URL: http://dx.doi.org/10.1093/oso/9780199582587.001.0001.

[39] Jozef J. Dudek et al. "Toward the excited meson spectrum of dynamical QCD". In: *Physical Review D* 82.3 (Aug. 2010). ISSN: 1550-2368. DOI: 10.1103/physrevd.82.034508. URL: http://dx.doi.org/10.1103/PhysRevD.82.034508.

[40] David J. Griffiths and Darrell F. Schroeter. *Introduction to quantum mechanics*. Third edition. Cambridge ; New York, NY: Cambridge University Press, 2018. ISBN: 978-1-107-18963-8.

[41] J. J. Sakurai and Jim Napolitano. *Modern Quantum Mechanics*. 3rd ed. Cambridge University Press, 2020.

[42] B.C. Hall. *Lie Groups, Lie Algebras, and Representations: An Elementary Introduction*. Graduate Texts in Mathematics. Springer, 2015. ISBN: 9780387401225. URL: https://doi.org/10.1007/978-3-319-13467-3.

[43] Lorenzo Barca. "Nucleon form factors from Lattice QCD for neutrino oscillation experiments". PhD thesis. Universität Regensburg, Regensburg U., 2022. DOI: 10.5283/epub.53286.

[44] S. Prelovsek, U. Skerbis, and C. B. Lang. "Lattice operators for scattering of particles with spin". In: *JHEP* 01 (2017), p. 129. DOI: 10.1007/JHEP01(2017)129. arXiv: 1607.06738 [hep-lat].

[45] C. B. Lang et al. "Pion-nucleon scattering in the Roper channel from lattice QCD". In: *Phys. Rev. D* 95.1 (2017), p. 014510. DOI: 10.1103/PhysRevD.95.014510. arXiv: 1610.01422 [hep-lat].

[46] Lorenzo Barca, Gunnar Bali, and Sara Collins. "Toward N to Nπ matrix elements from lattice QCD". In: *Phys. Rev. D* 107.5 (2023), p. L051505. DOI: 10.1103/PhysRevD.107.L051505. arXiv: 2211.12278 [hep-lat].

[47] C. B. Lang and V. Verduci. "Scattering in the πN negative parity channel in lattice QCD". In: *Phys. Rev. D* 87.5 (2013), p. 054502. DOI: 10.1103/PhysRevD.87.054502. arXiv: 1212.5055 [hep-lat].

[48] Takaaki Kajita. "Nobel Lecture: Discovery of atmospheric neutrino oscillations". In: *Rev. Mod. Phys.* 88.3 (2016), p. 030501. DOI: 10.1103/RevModPhys.88.030501.

[49] Arthur B. McDonald. "Nobel Lecture: The Sudbury Neutrino Observatory: Observation of flavor change for solar neutrinos". In: *Rev. Mod. Phys.* 88.3 (2016), p. 030502. DOI: 10.1103/RevModPhys.88.030502.

[50] David J Griffiths. *Introduction to elementary particles; 2nd rev. version*. Physics textbook. New York, NY: Wiley, 2008. URL: https://cds.cern.ch/record/111880.

[51] M. C. Gonzalez-Garcia and Yosef Nir. "Neutrino Masses and Mixing: Evidence and Implications". In: *Rev. Mod. Phys.* 75 (2003), pp. 345–402. DOI: 10.1103/RevModPhys.75.345. arXiv: hep-ph/0202058.

[52] S. Navas et al. "Review of particle physics". In: *Phys. Rev. D* 110.3 (2024), p. 030001. DOI: 10.1103/PhysRevD.110.030001.

[53] S. M. Bilenky and C. Giunti. "Neutrinoless Double-Beta Decay: a Probe of Physics Beyond the Standard Model". In: *Int. J. Mod. Phys. A* 30.04n05 (2015), p. 1530001. DOI: 10.1142/S0217751X1530001X. arXiv: 1411.4791 [hep-ph].

[54] Ivan Esteban et al. "NuFit-6.0: updated global analysis of three-flavor neutrino oscillations". In: *JHEP* 12 (2024), p. 216. DOI: 10.1007/JHEP12(2024)216. arXiv: 2410.05380 [hep-ph].

[55] L. Wolfenstein. "Neutrino oscillations in matter". In: *Phys. Rev. D* 17 (9 May 1978), pp. 2369–2374. DOI: 10.1103/PhysRevD.17.2369. URL: https://link.aps.org/doi/10.1103/PhysRevD.17.2369.

[56] S. P. Mikheyev and A. Yu. Smirnov. "Resonance Amplification of Oscillations in Matter and Spectroscopy of Solar Neutrinos". In: *Sov. J. Nucl. Phys.* 42 (1985), pp. 913–917.

[57] Vernon D. Barger et al. "Matter Effects on Three-Neutrino Oscillations". In: *Phys. Rev. D* 22 (1980), p. 2718. DOI: 10.1103/PhysRevD.22.2718.

[58] R. Acciarri et al. "Long-Baseline Neutrino Facility (LBNF) and Deep Underground Neutrino Experiment (DUNE): Conceptual Design Report, Volume 1: The LBNF and DUNE Projects". In: (Jan. 2016). arXiv: 1601.05471 [physics.ins-det].

[59] Babak Abi et al. "Deep Underground Neutrino Experiment (DUNE), Far Detector Technical Design Report, Volume I Introduction to DUNE". In: *JINST* 15.08 (2020), T08008. DOI: 10.1088/1748-0221/15/08/T08008. arXiv: 2002.02967 [physics.ins-det].

[60] Andreas S. Kronfeld et al. "Lattice QCD and Neutrino-Nucleus Scattering". In: *Eur. Phys. J. A* 55.11 (2019), p. 196. DOI: 10.1140/epja/i2019-12916-x. arXiv: 1904.09931 [hep-lat].

[61] Aaron S. Meyer, André Walker-Loud, and Callum Wilkinson. "Status of Lattice QCD Determination of Nucleon Form Factors and their Relevance for the Few-GeV Neutrino Program". In: *Ann. Rev. Nucl. Part. Sci.* 72 (2022), pp. 205–232. DOI: 10.1146/annurev-nucl-010622-120608. arXiv: 2201.01839 [hep-lat].

[62] L. Alvarez Ruso et al. "Theoretical tools for neutrino scattering: interplay between lattice QCD, EFTs, nuclear physics, phenomenology, and neutrino event generators". In: (Mar. 2022). DOI: 10.1088/1361-6471/adae26. arXiv: 2203.09030 [hep-ph].

[63] J. A. Formaggio and G. P. Zeller. "From eV to EeV: Neutrino Cross Sections Across Energy Scales". In: *Rev. Mod. Phys.* 84 (2012), pp. 1307–1341. DOI: 10.1103/RevModPhys.84.1307. arXiv: 1305.7513 [hep-ex].

[64] Rajan Gupta. "Isovector Axial Charge and Form Factors of Nucleons from Lattice QCD". In: *Universe* 10.3 (2024), p. 135. DOI: 10.3390/universe10030135. arXiv: 2401.16614 [hep-lat].

[65] C. C. Chang et al. "A per-cent-level determination of the nucleon axial coupling from quantum chromodynamics". In: *Nature* 558.7708 (2018), pp. 91–94. DOI: 10.1038/s41586-018-0161-8. arXiv: 1805.12130 [hep-lat].

[66] Dalibor Djukanovic et al. "Isovector axial form factor of the nucleon from lattice QCD". In: *Phys. Rev. D* 106.7 (2022), p. 074503. DOI: 10.1103/PhysRevD.106.074503. arXiv: 2207.03440 [hep-lat].

[67] Sungwoo Park et al. "Precision nucleon charges and form factors using (2+1)-flavor lattice QCD". In: *Phys. Rev. D* 105.5 (2022), p. 054505. DOI: 10.1103/PhysRevD.105.054505. arXiv: 2103.05599 [hep-lat].

[68] Ryutaro Tsuji et al. "Nucleon isovector couplings in Nf=2+1 lattice QCD at the physical point". In: *Phys. Rev. D* 106.9 (2022), p. 094505. DOI: 10.1103/PhysRevD.106.094505. arXiv: 2207.11914 [hep-lat].

[69] Ryutaro Tsuji et al. "Nucleon form factors in Nf=2+1 lattice QCD at the physical point: Finite lattice spacing effect on the root-mean-square radii". In: *Phys. Rev. D* 109.9 (2024), p. 094505. DOI: 10.1103/PhysRevD.109.094505. arXiv: 2311.10345 [hep-lat].

[70] C. Alexandrou et al. "Nucleon axial and pseudoscalar form factors from lattice QCD at the physical point". In: *Phys. Rev. D* 103.3 (2021), p. 034509. DOI: 10.1103/PhysRevD.103.034509. arXiv: 2011.13342 [hep-lat].

[71] Gunnar S. Bali et al. "Nucleon axial structure from lattice QCD". In: *JHEP* 05 (2020), p. 126. DOI: 10.1007/JHEP05(2020)126. arXiv: 1911.13150 [hep-lat].

[72] Gunnar S. Bali et al. "Octet baryon isovector charges from Nf=2+1 lattice QCD". In: *Phys. Rev. D* 108.3 (2023), p. 034512. DOI: 10.1103/PhysRevD.108.034512. arXiv: 2305.04717 [hep-lat].

[73] Yong-Chull Jang et al. "Nucleon isovector axial form factors". In: *Phys. Rev. D* 109.1 (2024), p. 014503. DOI: 10.1103/PhysRevD.109.014503. arXiv: 2305.11330 [hep-lat].

[74] Oliver Bär. "Nucleon-pion-state contribution to nucleon two-point correlation functions". In: *Physical Review D* 92.7 (Oct. 2015). ISSN: 1550-2368. DOI: 10.1103/physrevd.92.074504. URL: http://dx.doi.org/10.1103/PhysRevD.92.074504.

[75] Oliver Bär. "Three-particle $N\pi\pi$ state contribution to the nucleon two-point function in lattice QCD". In: *Phys. Rev. D* 97.9 (2018), p. 094507. DOI: 10.1103/PhysRevD.97.094507. arXiv: 1802.10442 [hep-lat].

[76] Rajan Gupta et al. "The pion-nucleon sigma term from Lattice QCD". In: *PoS* CD2021 (2024), p. 060. DOI: 10.22323/1.413.0060. arXiv: 2203.13862 [hep-lat].

[77] G. S. Bali et al. "Solving the PCAC puzzle for nucleon axial and pseudoscalar form factors". In: *Phys. Lett. B* 789 (2019), pp. 666–674. DOI: 10.1016/j.physletb.2018.12.053. arXiv: 1810.05569 [hep-lat].

[78] Yong-Chull Jang et al. "Axial Vector Form Factors from Lattice QCD that Satisfy the PCAC Relation". In: *Phys. Rev. Lett.* 124.7 (2020), p. 072002. DOI: 10.1103/PhysRevLett.124.072002. arXiv: 1905.06470 [hep-lat].

[79] Jinchen He et al. "Detailed analysis of excited-state systematics in a lattice QCD calculation of gA". In: *Phys. Rev. C* 105.6 (2022), p. 065203. DOI: 10.1103/PhysRevC.105.065203. arXiv: 2104.05226 [hep-lat].

[80] Constantia Alexandrou et al. "Investigation of pion-nucleon contributions to nucleon matrix elements". In: *Phys. Rev. D* 110.9 (2024), p. 094514. DOI: 10.1103/PhysRevD.110.094514. arXiv: 2408.03893 [hep-lat].

[81] Anthony V. Grebe and Michael Wagman. "Nucleon-Pion Spectroscopy from Sparsened Correlators". In: (Nov. 2023). arXiv: 2312.00321 [hep-lat].

[82] C. Alexandrou et al. "Nucleon to Delta transition form factors with $N_F = 2 + 1$ domain wall fermions". In: *Phys. Rev. D* 83 (2011), p. 014501. DOI: 10.1103/PhysRevD.83.014501. arXiv: 1011.3233 [hep-lat].

[83] C. Alexandrou et al. "Determination of Δ Resonance Parameters from Lattice QCD". In: *Phys. Rev. D* 88.3 (2013), p. 031501. DOI: 10.1103/PhysRevD.88.031501. arXiv: 1305.6081 [hep-lat].

[84] Constantia Alexandrou et al. "Study of decuplet baryon resonances from lattice QCD". In: *Phys. Rev. D* 93.11 (2016), p. 114515. DOI: 10.1103/PhysRevD.93.114515. arXiv: 1507.02724 [hep-lat].

[85] N. Mathur et al. "Roper resonance and S(11)(1535) from lattice QCD". In: *Phys. Lett. B* 605 (2005), pp. 137–143. DOI: 10.1016/j.physletb.2004.11.010. arXiv: hep-ph/0306199.

[86] Adrian L. Kiratidis et al. "Search for low-lying lattice QCD eigenstates in the Roper regime". In: *Phys. Rev. D* 95.7 (2017), p. 074507. DOI: 10.1103/PhysRevD.95.074507. arXiv: 1608.03051 [hep-lat].

[87] Jia-jun Wu et al. "Structure of the Roper Resonance from Lattice QCD Constraints". In: *Phys. Rev. D* 97.9 (2018), p. 094509. DOI: 10.1103/PhysRevD.97.094509. arXiv: 1703.10715 [nucl-th].

[88] Gerhard Bohm and Guenter Zech. *Introduction to statistics and data analysis for physicists*. Hamburg: DESY, 2014. ISBN: 978-3-935702-88-1. DOI: 10.3204/DESY-BOOK/statistics.

[89] John A. Gubner. *Probability and Random Processes for Electrical and Computer Engineers*. Cambridge University Press, 2006.

[90] B. Efron. "Bootstrap Methods: Another Look at the Jackknife". In: *The Annals of Statistics* 7.1 (1979), pp. 1–26. DOI: 10.1214/aos/1176344552. URL: https://doi.org/10.1214/aos/1176344552.

[91] B. Efron and C. Stein. "The Jackknife Estimate of Variance". In: *The Annals of Statistics* 9.3 (1981), pp. 586–596. DOI: 10.1214/aos/1176345462. URL: https://doi.org/10.1214/aos/1176345462.

[92] Andreas Hackl. *QStatPy*. Version v1.0. Apr. 2025. DOI: 10.5281/zenodo.15265042. URL: https://doi.org/10.5281/zenodo.15265041.

[93] Christoph Lehner. *JKS measurement database, 2024-10*. Version 2024-10. Oct. 2024. DOI: 10.5281/zenodo.14017593. URL: https://doi.org/10.5281/zenodo.14017593.

[94] KENNETH LEVENBERG. "A METHOD FOR THE SOLUTION OF CERTAIN NON-LINEAR PROBLEMS IN LEAST SQUARES". In: *Quarterly of Applied Mathematics* 2.2 (1944), pp. 164–168. ISSN: 0033569X, 15524485. URL: http://www.jstor.org/stable/43633451 (visited on 03/26/2025).

[95] Donald W. Marquardt. "An Algorithm for Least-Squares Estimation of Nonlinear Parameters". In: *Journal of the Society for Industrial and Applied Mathematics* 11.2 (1963), pp. 431–441. DOI: 10.1137/0111030. eprint: https://doi.org/10.1137/0111030. URL: https://doi.org/10.1137/0111030.

[96] T. DeGrand and S. Schaefer. "Improving meson two-point functions by low-mode averaging". In: *Nuclear Physics B - Proceedings Supplements* 140 (Mar. 2005), pp. 296–298. ISSN: 0920-5632. DOI: 10.1016/j.nuclphysbps.2004.11.352. URL: http://dx.doi.org/10.1016/j.nuclphysbps.2004.11.352.

[97] Gunnar S. Bali, Sara Collins, and Andreas Schäfer. "Effective noise reduction techniques for disconnected loops in Lattice QCD". In: *Computer Physics Communications* 181.9 (Sept. 2010), pp. 1570–1583. ISSN: 0010-4655. DOI: 10.1016/j.cpc.2010.05.008. URL: http://dx.doi.org/10.1016/j.cpc.2010.05.008.

[98] Thomas Blum, Taku Izubuchi, and Eigo Shintani. "New class of variance-reduction techniques using lattice symmetries". In: *Physical Review D* 88.9 (Nov. 2013). ISSN: 1550-2368. DOI: 10.1103/physrevd.88.094503. URL: http://dx.doi.org/10.1103/PhysRevD.88.094503.

[99] Michael Peardon et al. "A Novel quark-field creation operator construction for hadronic physics in lattice QCD". In: *Phys. Rev. D* 80 (2009), p. 054506. DOI: 10.1103/PhysRevD.80.054506. arXiv: 0905.2160 [hep-lat].

[100] Mattia Bruno et al. "Isospin 0 and 2 two-pion scattering at physical pion mass using distillation with periodic boundary conditions in lattice QCD". In: (Apr. 2023). arXiv: 2304.03313 [hep-lat].

[101] Colin Egerer, David Richards, and Frank Winter. "Controlling excited-state contributions with distillation in lattice QCD calculations of nucleon isovector charges g_S^{u-d}, g_A^{u-d}, g_T^{u-d}". In: *Phys. Rev. D* 99.3 (2019), p. 034506. DOI: 10.1103/PhysRevD.99.034506. arXiv: 1810.09991 [hep-lat].

[102] Andreas Hackl. *AutoWick*. Version 1.0. 2024. URL: https://github.com/andreas-hackl/AutoWick.

[103] Christoph Lehner et al. *Grid Python Toolkit (GPT), 2024-10*. Version 2024-10. Oct. 2024. DOI: 10.5281/zenodo.14017415. URL: https://doi.org/10.5281/zenodo.14017415.

[104] ALPHA collaboration et al. "On the generalized eigenvalue method for energies and matrix elements in lattice field theory". In: *Journal of High Energy Physics* 2009.04 (Apr. 2009), pp. 094–094. ISSN: 1029-8479. DOI: 10.1088/1126-6708/2009/04/094. URL: http://dx.doi.org/10.1088/1126-6708/2009/04/094.

[105] Martin Lüscher and Ulli Wolff. "How to calculate the elastic scattering matrix in two-dimensional quantum field theories by numerical simulation". In: *Nuclear Physics B* 339.1 (1990), pp. 222–252. ISSN: 0550-3213. DOI: https://doi.org/10.1016/0550-3213(90)90540-T. URL: https://www.sciencedirect.com/science/article/pii/055032139090540T.

[106] Richard Sinkhorn. "A Relationship Between Arbitrary Positive Matrices and Doubly Stochastic Matrices". In: *The Annals of Mathematical Statistics* 35.2 (1964), pp. 876–879. DOI: 10.1214/aoms/1177703591. URL: https://doi.org/10.1214/aoms/1177703591.

[107] Paul Knopp and Richard Sinkhorn. "Concerning nonnegative matrices and doubly stochastic matrices." In: *Pacific Journal of Mathematics* 21.2 (1967), pp. 343–348.

[108] Joseph Wasem. "Omega baryon interactions with lattice QCD". In: *PoS* LATTICE2012 (2012). Ed. by Derek Leinweber et al., p. 133. DOI: 10.22323/1.164.0133.

[109] T. Blum et al. "Domain wall QCD with physical quark masses". In: *Phys. Rev. D* 93.7 (2016), p. 074505. DOI: 10.1103/PhysRevD.93.074505. arXiv: 1411.7017 [hep-lat].

[110] Nolan Miller et al. "Scale setting the Möbius domain wall fermion on gradient-flowed HISQ action using the omega baryon mass and the gradient-flow scales t_0 and w_0". In: *Phys. Rev. D* 103.5 (2021), p. 054511. DOI: 10.1103/PhysRevD.103.054511. arXiv: 2011.12166 [hep-lat].

[111] Renwick J. Hudspith, Matthias F. M. Lutz, and Daniel Mohler. "Precise Omega baryons from lattice QCD". In: (Apr. 2024). arXiv: 2404.02769 [hep-lat].

[112] Subhasish Basak et al. "Clebsch-Gordan construction of lattice interpolating fields for excited baryons". In: *Phys. Rev. D* 72 (2005), p. 074501. DOI: 10.1103/PhysRevD.72.074501. arXiv: hep-lat/0508018.

[113] P. A. Boyle et al. "Use of stochastic sources for the lattice determination of light quark physics". In: *JHEP* 08 (2008), p. 086. DOI: 10.1088/1126-6708/2008/08/086. arXiv: 0804.1501 [hep-lat].

[114] T. Blum et al. "Update of Euclidean windows of the hadronic vacuum polarization". In: *Phys. Rev. D* 108.5 (2023), p. 054507. DOI: 10.1103/PhysRevD.108.054507. arXiv: 2301.08696 [hep-lat].

[115] A. Ali Khan et al. "The nucleon mass in Nf=2 lattice QCD: finite size effects from chiral perturbation theory". In: *Nuclear Physics B* 689.3 (June 2004), pp. 175–194. ISSN: 0550-3213. DOI: 10.1016/j.nuclphysb.2004.04.018. URL: http://dx.doi.org/10.1016/j.nuclphysb.2004.04.018.

[116] Massimiliano Procura, Thomas R. Hemmert, and Wolfram Weise. "Nucleon mass, sigma term, and lattice QCD". In: *Physical Review D* 69.3 (Feb. 2004). ISSN: 1550-2368. DOI: 10.1103/physrevd.69.034505. URL: http://dx.doi.org/10.1103/PhysRevD.69.034505.

[117] Long-Bin Chen et al. "Light quark mass dependence of nucleon mass to two-loop order". In: (June 2024). arXiv: 2406.04124 [hep-ph].

[118] D. Siemens et al. "Reconciling threshold and subthreshold expansions for pion–nucleon scattering". In: *Phys. Lett. B* 770 (2017), pp. 27–34. DOI: 10.1016/j.physletb.2017.04.039. arXiv: 1610.08978 [nucl-th].

[119] H. Akaike. "A new look at the statistical model identification". In: *IEEE Transactions on Automatic Control* 19.6 (1974), pp. 716–723. DOI: 10.1109/TAC.1974.1100705.

[120] Hirotogu Akaike. "Information Theory and an Extension of the Maximum Likelihood Principle". In: *Selected Papers of Hirotugu Akaike*. Ed. by Emanuel Parzen, Kunio Tanabe, and Genshiro Kitagawa. New York, NY: Springer New York, 1998, pp. 199–213. ISBN: 978-1-4612-1694-0. DOI: 10.1007/978-1-4612-1694-0_15. URL: https://doi.org/10.1007/978-1-4612-1694-0_15.

[121] Andre Walker-Loud. *New lessons from the nucleon mass, lattice QCD and heavy baryon chiral perturbation theory*. 2008. arXiv: 0810.0663 [hep-lat]. URL: https://arxiv.org/abs/0810.0663.

[122] Francesco Knechtli et al. "Optimizing creation operators for charmonium spectroscopy on the lattice". In: *Phys. Rev. D* 106.3 (2022), p. 034501. DOI: 10.1103/PhysRevD.106.034501. arXiv: 2205.11564 [hep-lat].

[123] Charles R. Harris et al. "Array programming with NumPy". In: *Nature* 585.7825 (Sept. 2020), pp. 357–362. DOI: 10.1038/s41586-020-2649-2. URL: https://doi.org/10.1038/s41586-020-2649-2.

[124] James Bradbury et al. *JAX: composable transformations of Python+NumPy programs*. Version 0.3.13. 2018. URL: http://github.com/jax-ml/jax.

[125] Pauli Virtanen et al. "SciPy 1.0: Fundamental Algorithms for Scientific Computing in Python". In: *Nature Methods* 17 (2020), pp. 261–272. DOI: 10.1038/s41592-019-0686-2.

[126] J. D. Hunter. "Matplotlib: A 2D graphics environment". In: *Computing in Science & Engineering* 9.3 (2007), pp. 90–95. DOI: 10.1109/MCSE.2007.55.

[127] Till Tantau. *The TikZ and PGF Packages. Manual for version 3.1.10*. Apr. 11, 2025. URL: https://tikz.dev/.

[128] Joshua P. Ellis. "Ti k Z-Feynman: Feynman diagrams with Ti k Z". In: *Computer Physics Communications* 210 (Jan. 2017), pp. 103–123. ISSN: 0010-4655. DOI: 10.1016/j.cpc.2016.08.019. URL: http://dx.doi.org/10.1016/j.cpc.2016.08.019.

[129] P.A. Boyle et al. *Grid*. URL: https://github.com/paboyle/Grid.

[130] Peter A. Boyle et al. "Grid: A next generation data parallel C++ QCD library". In: *PoS* LATTICE2015 (2016), p. 023. DOI: 10.22323/1.251.0023.

[131] Azusa Yamaguchi et al. "Grid: OneCode and FourAPIs". In: *PoS* LATTICE2021 (2022), p. 035. DOI: 10.22323/1.396.0035. arXiv: 2203.06777 [hep-lat].

A. Appendix

A.1. Conventions

In particle physics, it is conventional to adopt natural units, where Planck's constant and the speed of light are given by

$$\hbar = c = 1. \tag{A.1}$$

Within this system, all quantities are expressed in orders of energy, generally GeV, and the relation between energy and distance is established as

$$0.19732 \text{ GeV} = 1 \text{ fm}^{-1}. \tag{A.2}$$

Natural units are employed consistently throughout this thesis.
In addition, we follow the convention that 4-vectors are typically denoted by non-bold lowercase letters such as x, y, z, etc. These 4-vectors comprise a temporal component t_x and a spatial vector $\boldsymbol{x}$, represented by

$$x = (\boldsymbol{x}, t_x), \tag{A.3}$$

where the spatial vector is always represented by the corresponding bold lowercase letter. In this thesis, the indexing usually follows the convention used in programming languages, starting at zero. We denote spin indices by lowercase Greek letters $(\alpha, \beta, \gamma, \delta, \dots)$, with α indexed as $0, 1, 2, 3$, and color indices by lowercase Latin letters $(a, b, c, \dots)$, indexed as $a = 0, 1, 2$.

A.2. Gamma Matrices

The Minkowski gamma matrices are elements of a Minkowski Clifford algebra defined by the anticommutator relation

$$\{\gamma_\mu^M, \gamma_\nu^M\} = \gamma_\mu^M \gamma_\nu^M + \gamma_\nu^M \gamma_\mu^M = 2g_{\mu\nu} \mathbb{1}_4, \tag{A.4}$$

where $g_{\mu\nu} = \text{diag}(1, -1, -1, -1)$ indicates the Minkowski metric tensor and $\mu, \nu = t, x, y, z$. To derive the Euclidean gamma matrices from the Minkowski ones, we set

$$\gamma_x = -i\gamma_x^M, \gamma_y = -i\gamma_y^M, \gamma_z = -i\gamma_z^M, \gamma_t = \gamma_t^M, \tag{A.5}$$

which satisfy the Euclidean anticommutator relations

$$\{\gamma_\mu, \gamma_\nu\} = 2\delta_{\mu\nu} \mathbb{1}_4, \tag{A.6}$$

where $\delta_{\mu\nu}$ is the Euclidean metric. Additionally, the fifth gamma matrix is defined as

$$\gamma_5 = \gamma_x \gamma_y \gamma_z \gamma_t. \tag{A.7}$$

By default, we use the DeGrand-Rossi basis, which is used as a standard basis in the software packages `GRID` [129] and `GPT` [103]. The gamma matrices in the DeGrand-Rossi basis are defined by

$$\gamma_x = \begin{pmatrix} 0 & i\sigma_x \\ -i\sigma_x & 0 \end{pmatrix}, \gamma_y = \begin{pmatrix} 0 & -i\sigma_y \\ i\sigma_y & 0 \end{pmatrix}, \gamma_z = \begin{pmatrix} 0 & i\sigma_z \\ -i\sigma_z & 0 \end{pmatrix}, \gamma_t = \begin{pmatrix} 0 & \mathbb{1}_2 \\ \mathbb{1}_2 & 0 \end{pmatrix}, \tag{A.8}$$

where σ_i represent the Pauli matrices. In this basis the fifth gamma matrix is

$$\gamma_5 = \begin{pmatrix} \mathbb{1}_2 & 0 \\ 0 & -\mathbb{1}_2 \end{pmatrix}. \tag{A.9}$$

The charge conjugation matrix C, relevant for the definition of baryon operators, which is defined through

$$C\gamma_\mu C^{-1} = -\gamma_\mu^T, \tag{A.10}$$

is in the chiral representation given by

$$C = i\gamma_y\gamma_t. \tag{A.11}$$

In Ch. 6, instead of utilizing the chiral representation, we opt for the Dirac-Pauli representation defined by the gamma matrices

$$\gamma_j^{(\mathrm{DP})} = \begin{pmatrix} 0 & -i\sigma_j \\ i\sigma_j & 0 \end{pmatrix}, \gamma_t^{(\mathrm{DP})} = \begin{pmatrix} \mathbb{1}_2 & 0 \\ 0 & -\mathbb{1}_2 \end{pmatrix}, \tag{A.12}$$

where j spans x, y, z.

A.3. Summary of Fit Results of the Nucleon Spectroscopy

This section summarizes the fit results from Ch. 8. For ensembles with a minimum of 60 independent configurations, such as ensemble 4, D, or 9, we employ correlated fits within the positive parity channel. For stable correlated fits in the negative parity channel, a larger set of statistical data is needed. Thus, only Ensemble 4 is involved in correlated fits in this scenario. Tab. A.1 provides the fit results across all ensembles, including the effective mass curves in the positive parity sector, while Tab. A.2 details those in the negative parity sector. Both tables contain eight columns, beginning with the fit tag, which identifies the effective mass curve being fitted. `N2N` denotes the nucleon 2-point function, whereas tags starting with `GEVP` refer to specific GEVP modes. The next column specifies the fit range of the chosen fit, followed by the parameters in the subsequent two columns. The results for the overlap factor A are excluded due to the error overestimation caused by an asymmetrical distribution of the individual jackknife samples. The value $\sigma_{\tau-1}$, derived from the extrapolation criterion in Eq. 5.23, evaluates the discrepancy between the first excluded data point of the fit and the expected value of the model. Ideally, this value should be less than 2, but sometimes no fit range meets this requirement, particularly in the negative parity channel. The following column displays the reduced χ^2 value, which is the χ^2 value divided by the degrees of freedom. We preferred the reduced χ^2 over the p-value because a combination of correlated and uncorrelated fits is used. The final column indicates whether the fit is correlated (c) or uncorrelated (uc).

positive parity						
Tag	range	aE	aE^{ex}	σ_{τ_0-1}	χ^2/dof	type
Ensemble-4						
GEVP0	4 - 12	0.6358(24)	1.83(23)	2.23	0.93	c
GEVP1	4 - 10	0.9458(55)	1.86(21)	1.75	1.73	c
GEVP2	4 - 10	0.9857(80)	1.94(54)	0.61	0.35	c
N2N	5 - 12	0.6375(32)	1.62(29)	1.40	1.18	c
Ensemble-D						
GEVP0	4 - 12	0.6244(23)	1.48(16)	0.87	0.25	c
GEVP1	4 - 12	0.9004(29)	1.59(10)	0.30	0.88	c
GEVP2	4 - 12	0.9362(35)	1.60(10)	0.43	0.52	c
N2N	5 - 12	0.6248(24)	1.44(15)	0.93	0.24	c
Ensemble-L						
GEVP0	6 - 18	0.4511(42)	1.02(12)	1.17	0.47	uc
GEVP1	6 - 18	0.6123(52)	1.11(12)	0.73	0.71	uc
GEVP2	6 - 18	0.6839(53)	1.16(12)	0.46	0.31	uc
N2N	7 - 18	0.4510(42)	1.02(12)	1.15	0.50	uc
Ensemble-9						
GEVP0	5 - 17	0.4622(26)	0.898(71)	-1.11	1.26	c
GEVP1	6 - 15	0.661(18)	0.877(90)	0.50	0.69	c
GEVP2	5 - 15	0.7151(65)	1.044(70)	-3.28	1.75	c
N2N	6 - 17	0.4621(32)	0.851(63)	-1.81	1.58	c
Ensemble-1						
GEVP0	3 - 14	0.5909(41)	1.51(23)	-0.31	0.19	uc
GEVP1	3 - 10	0.8260(58)	1.61(18)	-0.87	0.15	uc
GEVP2	3 - 10	0.8432(70)	1.51(13)	-2.00	0.16	uc
N2N	4 - 15	0.5918(44)	1.44(21)	-0.54	0.13	uc
Ensemble-3						
GEVP0	2 - 10	0.5919(40)	1.433(87)	2.15	0.76	uc
GEVP1	4 - 10	0.811(31)	1.05(30)	-1.87	0.29	uc
GEVP2	3 - 10	0.8521(68)	1.53(14)	-2.00	0.12	uc
N2N	3 - 11	0.5930(42)	1.406(83)	2.17	0.83	uc
Ensemble-C						
GEVP0	4 - 18	0.5475(88)	1.33(24)	0.80	0.48	uc
GEVP1	4 - 18	0.6856(86)	1.48(21)	0.87	0.38	uc
GEVP2	4 - 18	0.7076(93)	1.47(22)	0.76	0.37	uc
N2N	5 - 18	0.5473(90)	1.31(24)	0.73	0.45	uc

Table A.1.: Summary of all excited-state fits of the GEVP and two-point effective mass curves with the fit form from Eq. 8.1 for the different ensembles in the positive parity sector. The last column denotes whether a fit is correlated (c) or uncorrelated (uc).

negative parity						
Tag	range	aE	aE^{ex}	σ_{τ_0-1}	χ^2/dof	type
Ensemble-4						
GEVP0	4 - 9	0.7841(35)	1.64(19)	1.44	2.31	c
GEVP1	4 - 9	0.971(26)	1.59(85)	0.42	0.53	c
GEVP2	3 - 7	1.0058(82)	3.19(13)	2.96	0.44	c
N2N	4 - 10	0.928(17)	2.2(1.3)	-0.42	0.03	c
Ensemble-D						
GEVP0	4 - 7	0.7782(27)	1.59(17)	0.57	0.00	uc
GEVP1	3 - 5	0.8958(38)	1.523(51)	-8.47	0.00	uc
GEVP2	2 - 5	0.918(23)	1.81(19)	3.79	0.55	uc
N2N	3 - 7	0.865(24)	1.58(16)	3.67	0.83	uc
Ensemble-L						
GEVP0	4 - 8	0.5732(80)	1.13(11)	0.38	0.41	uc
GEVP1	4 - 7	0.6313(87)	1.32(12)	1.38	0.14	uc
GEVP2	2 - 6	0.690(52)	1.19(16)	-1.35	0.03	uc
N2N	4 - 7	0.679(87)	1.18(40)	-0.93	0.04	uc
Ensemble-9						
GEVP0	4 - 10	0.5698(33)	0.983(44)	-0.41	0.06	uc
GEVP1	4 - 10	0.686(50)	1.23(62)	0.63	0.01	uc
GEVP2	4 - 10	0.7176(52)	1.138(57)	-0.19	0.12	uc
N2N	5 - 11	0.627(42)	1.03(32)	0.75	0.02	uc
Ensemble-1						
GEVP0	4 - 10	0.7064(53)	1.62(52)	0.36	0.08	uc
GEVP1	3 - 8	0.8399(64)	1.45(10)	-3.43	0.04	uc
GEVP2	3 - 6	0.8(1.4)	1.1(1.9)	-1.17	0.06	uc
N2N	4 - 10	0.802(98)	1.39(77)	-0.36	0.18	uc
Ensemble-3						
GEVP0	4 - 8	0.703(11)	1.13(28)	-1.05	0.25	uc
GEVP1	2 - 6	0.837(49)	1.53(36)	0.20	0.26	uc
GEVP2	3 - 6	0.8661(55)	3.0(1.1)	0.77	0.19	uc
N2N	4 - 7	0.800(29)	1.85(61)	0.39	0.15	uc
Ensemble-C						
GEVP0	3 - 7	0.621(11)	1.24(11)	-1.66	0.48	uc
GEVP1	2 - 6	0.6825(55)	1.412(40)	-1.86	1.06	uc
GEVP2	2 - 5	0.723(93)	1.35(31)	1.46	0.33	uc
N2N	3 - 6	0.711(82)	1.35(28)	1.52	0.32	uc

Table A.2.: Summary over all excited state fits of the GEVP and two-point effective mass curves with the fit form from Eq. 8.1 for the different ensembles in the negative parity sector. The last column denotes whether a fit is correlated (c) or uncorrelated (uc).

A.4. Additional Figures

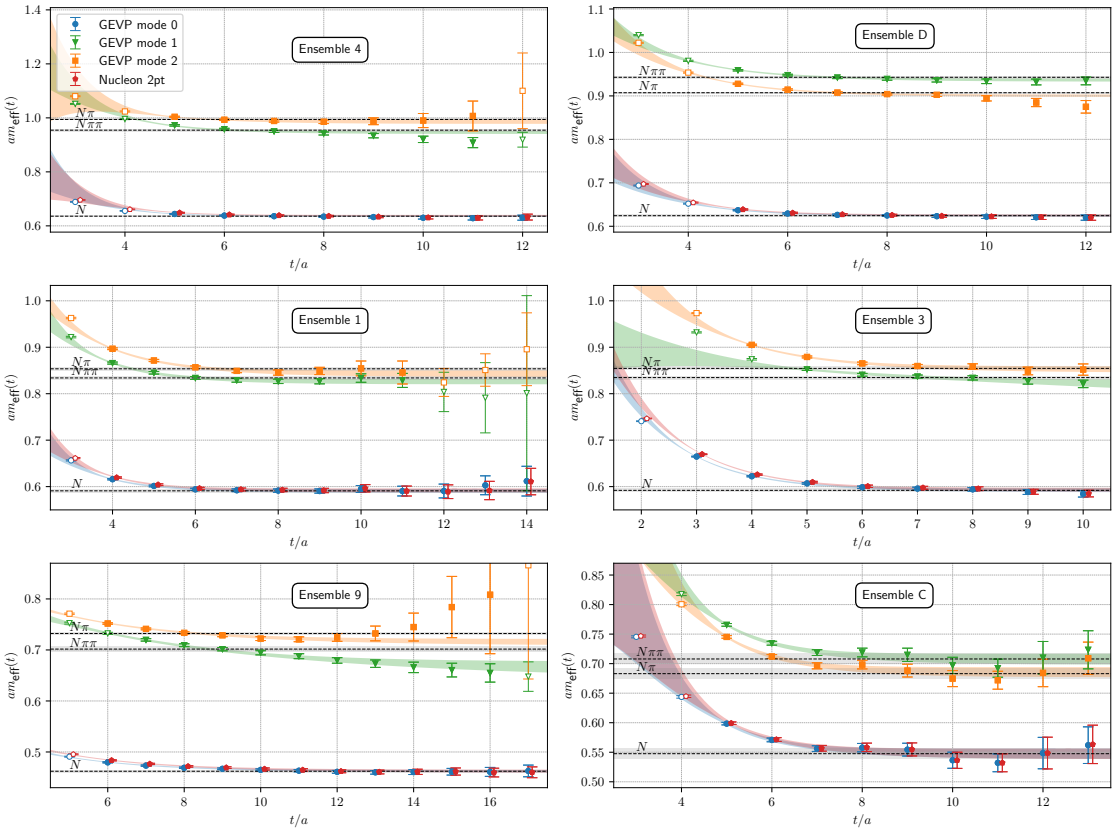

Figure A.1.: Overview plots of the remaining ensembles showing the same results as depicted in Fig. 8.1 for all other ensembles of this study.

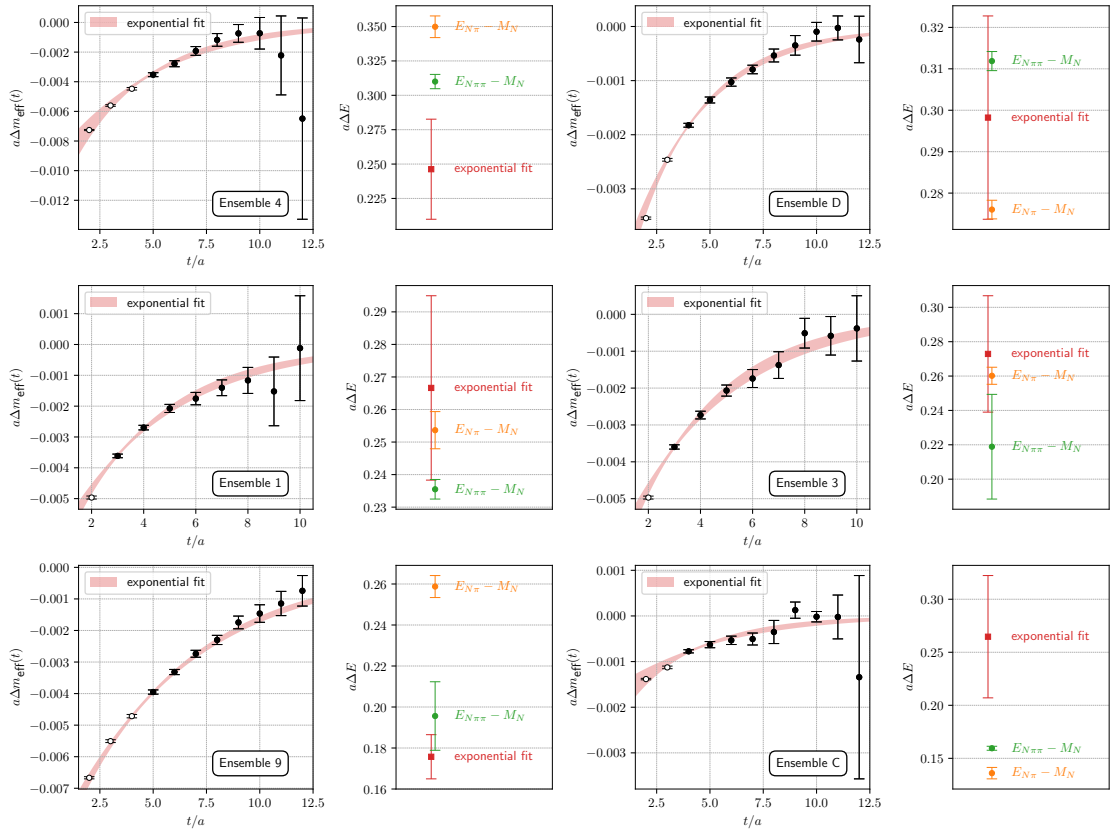

Figure A.2.: Overview plots of the remaining ensembles showing the same results as depicted in Fig. 8.2 for all other ensembles of this study.

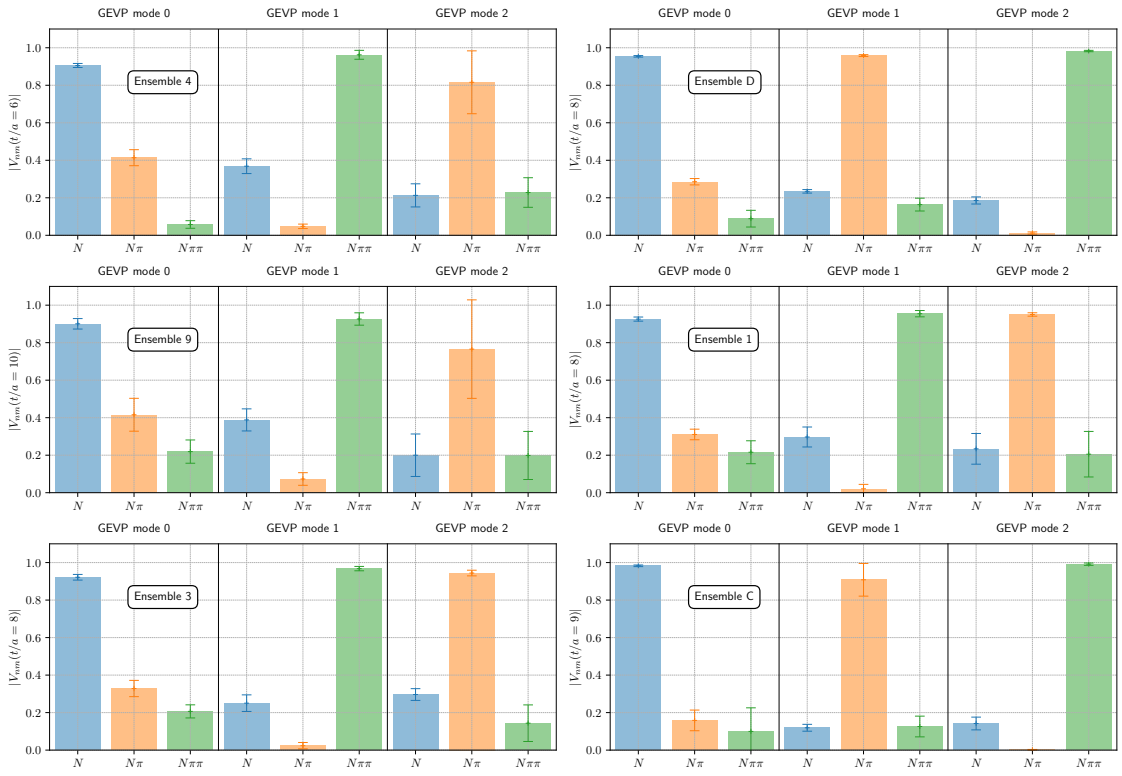

Figure A.3.: Overview plot of all GEVP eigenvectors. The plots depict the same eigenvectors as Fig. 8.3 for the remaining ensembles of this study. The reference time slices can vary between the different ensembles and are chosen so that the effective mass is converged to the state's mass while still having a moderate signal-to-noise ratio.

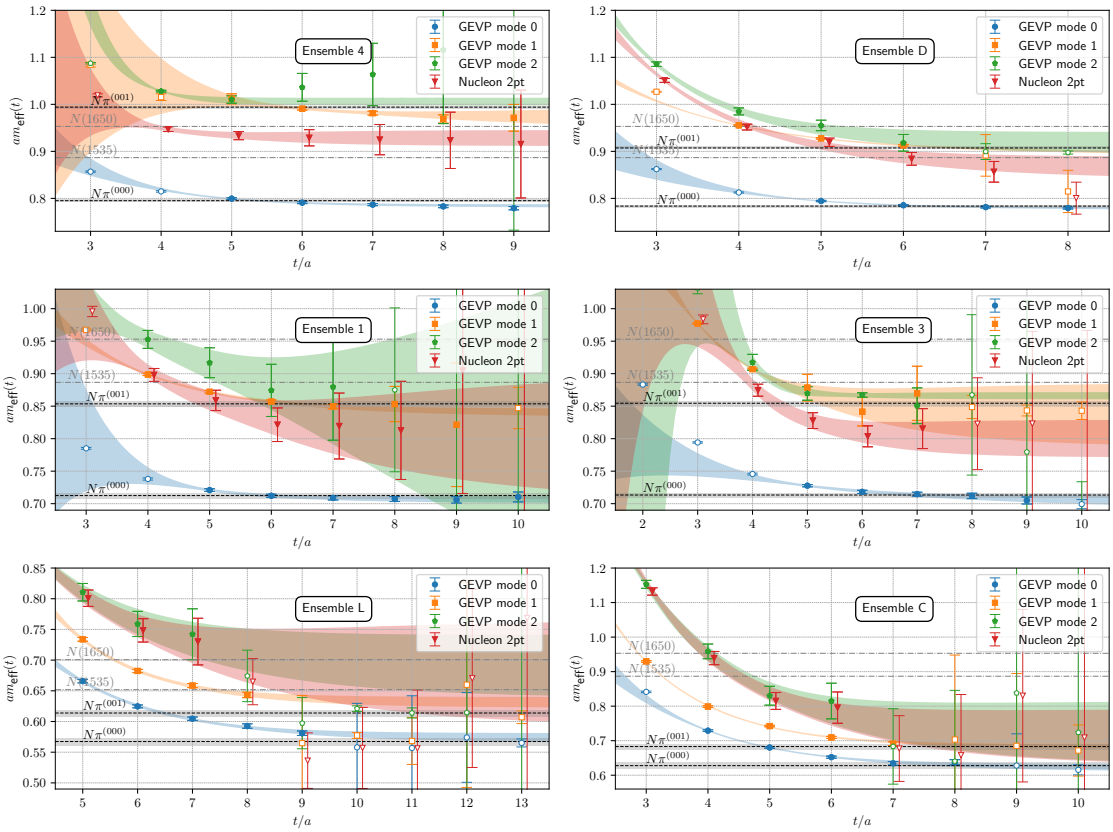

Figure A.4.: Overview over the GEVP effective masses of the remaining ensembles in the negative parity sector. The plots are similar to Fig. 8.8

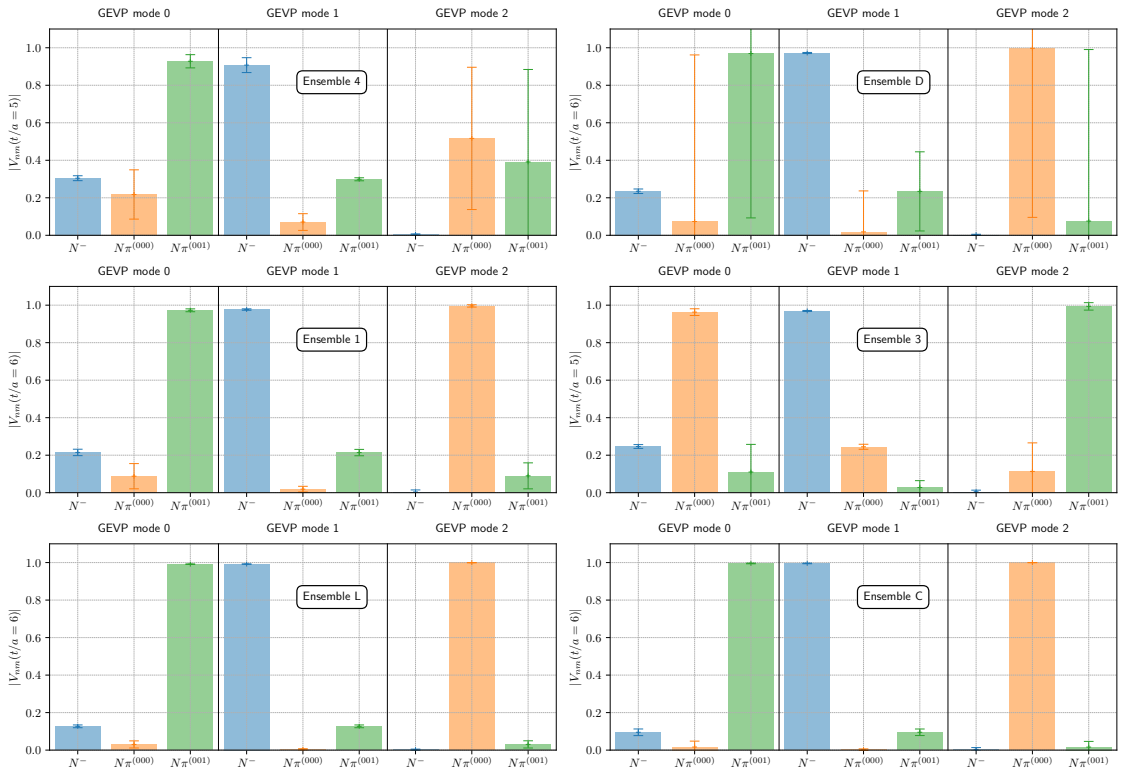

Figure A.5.: Overview plot of all negative parity GEVP eigenvectors. The plots depict the same eigenvectors as Fig. 8.9 for the remaining ensembles of this study. The reference time slices can vary between the different ensembles and are chosen such that the effective mass is converged to the state's mass while still having a moderate signal-to-noise ratio.

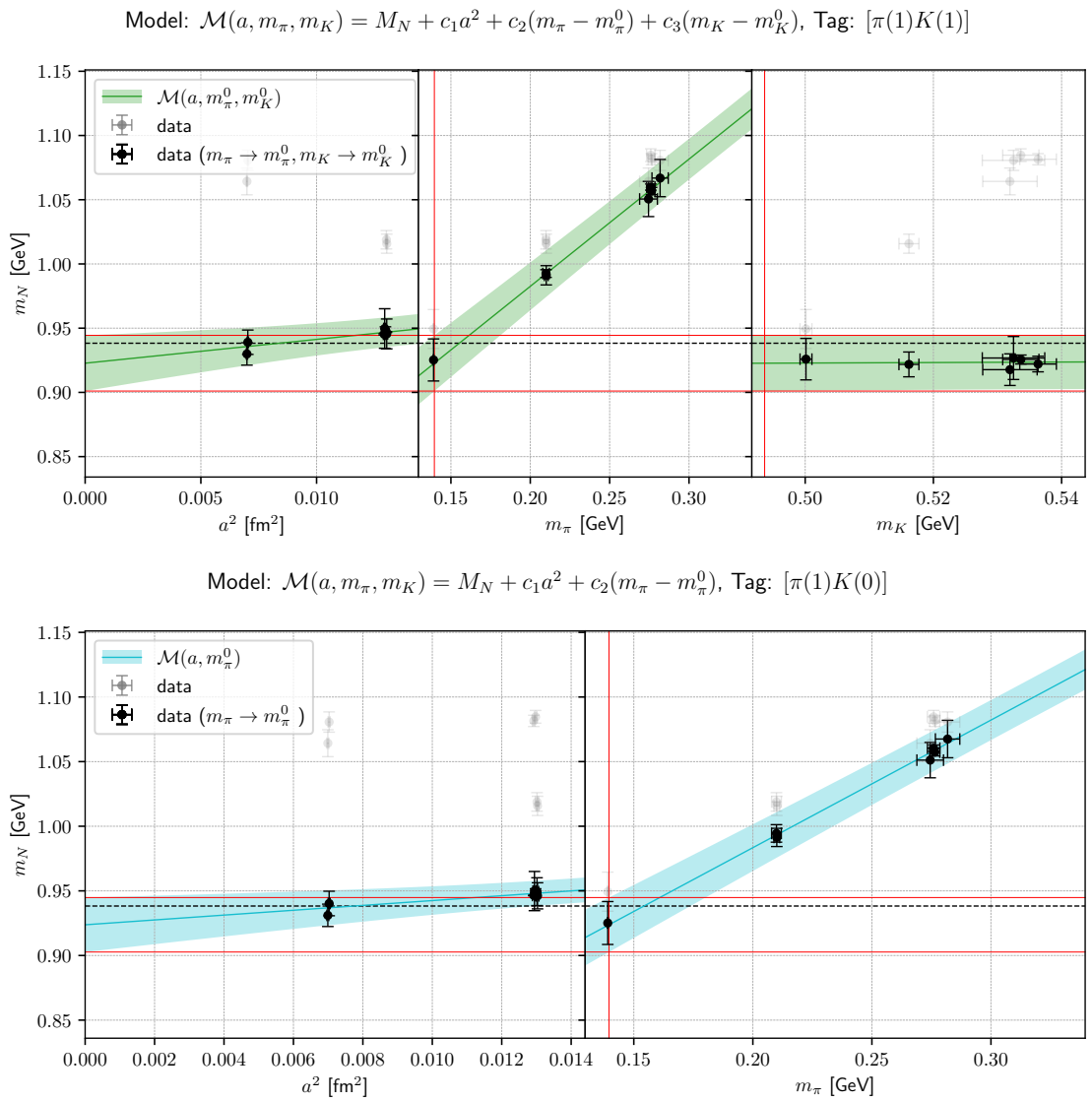

Figure A.6.: Overview of the linear models for the continuum and physical point extrapolation. The plots are similar to Fig. 8.6.

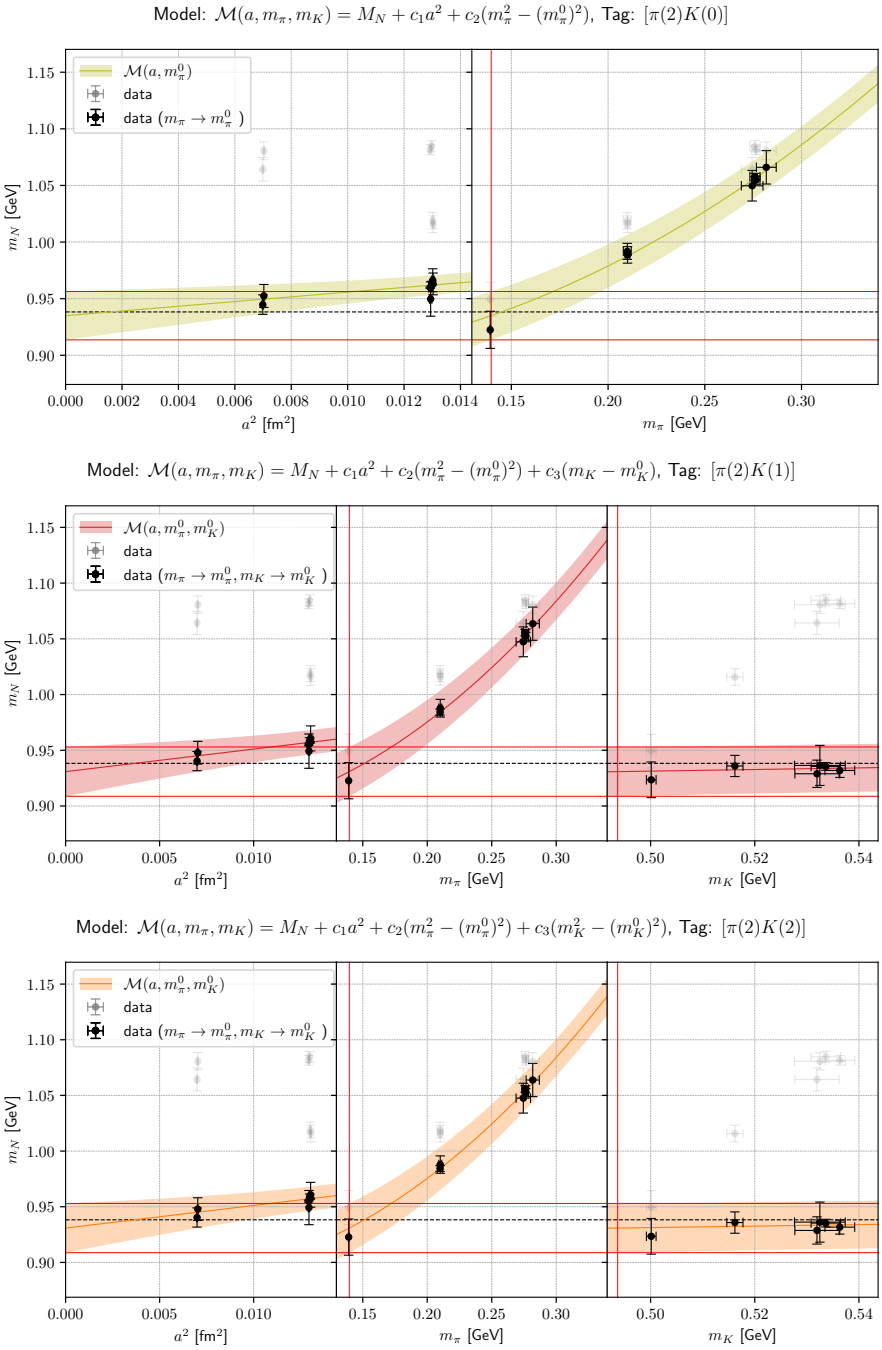

Figure A.7.: Overview of the quadratic models for the continuum and physical point extrapolation. The plots are similar to Fig. 8.6.

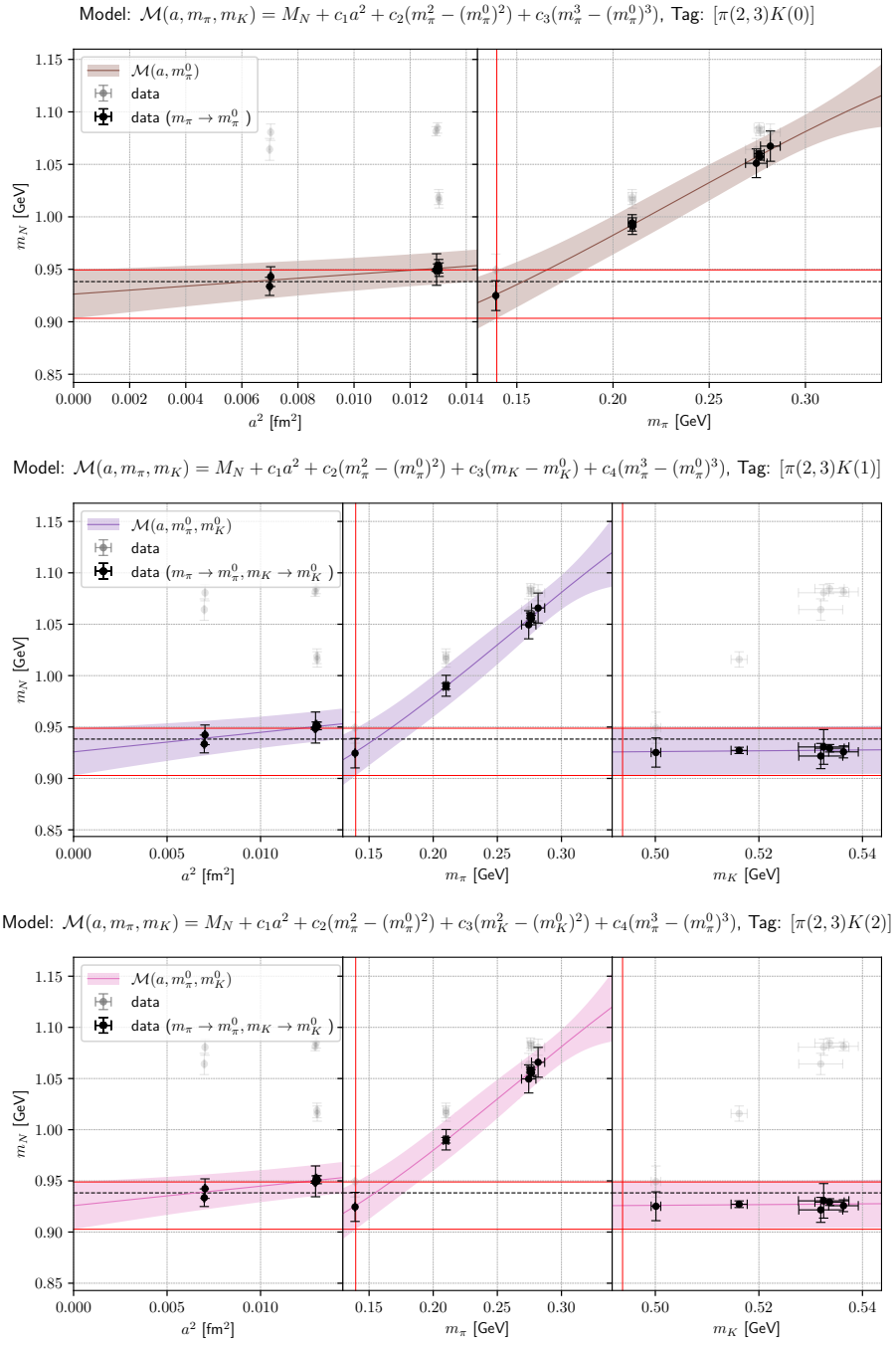

Figure A.8.: Overview of the quadratic models with a cubic term for the continuum and physical point extrapolation. The plots are similar to Fig. 8.6.